INFORMATION TO USERS

This manuscript has been reproduced from the microfilm master. UMI films the text directly from the original or copy submitted. Thus, some thesis and dissertation copies are in typewriter face, while others may be from any type of computer printer.

The quality of this reproduction is dependent upon the quality of the copy submitted. Broken or indistinct print, colored or poor quality illustrations and photographs, print bleedthrough, substandard margins, and improper alignment can adversely affect reproduction.

In the unlikely event that the author did not send UMI a complete manuscript and there are missing pages, these will be noted. Also, if unauthorized copyright material had to be removed, a note will indicate the deletion.

Oversize materials (e.g., maps, drawings, charts) are reproduced by sectioning the original, beginning at the upper left-hand corner and continuing from left to right in equal sections with small overlaps.

ProQuest Information and Learning
300 North Zeeb Road, Ann Arbor, MI 48106-1346 USA
800-521-0600

UMI®

Reproduced with permission of the copyright owner. Further reproduction prohibited without permission.

Reproduced with permission of the copyright owner. Further reproduction prohibited without permission.

UNIVERSITY OF ALBERTA

Study of Energy Flux in a Magnetron Sputter Deposition System

by

Samuel David Ekpe

A thesis submitted to the Faculty of Graduate Studies and Research in partial fulfillment of the requirements for the degree of Doctor of Philosophy

Department of Electrical and Computer Engineering

Edmonton, Alberta

Spring 2005

Reproduced with permission of the copyright owner. Further reproduction prohibited without permission.

Library and Archives Canada

Published Heritage Branch

395 Wellington Street
Ottawa ON K1A 0N4
Canada

Bibliothèque et Archives Canada

Direction du Patrimoine de l'édition

395, rue Wellington
Ottawa ON K1A 0N4
Canada

0-494-08228-3

Your file Votre référence
ISBN:
Our file Notre reterence
ISBN:

NOTICE:
The author has granted a non-exclusive license allowing Library and Archives Canada to reproduce, publish, archive, preserve, conserve, communicate to the public by telecommunication or on the Internet, loan, distribute and sell theses worldwide, for commercial or non-commercial purposes, in microform, paper, electronic and/or any other formats.

The author retains copyright ownership and moral rights in this thesis. Neither the thesis nor substantial extracts from it may be printed or otherwise reproduced without the author's permission.

AVIS:
L'auteur a accordé une licence non exclusive permettant à la Bibliothèque et Archives Canada de reproduire, publier, archiver, sauvegarder, conserver, transmettre au public par télécommunication ou par l'Internet, prêter, distribuer et vendre des thèses partout dans le monde, à des fins commerciales ou autres, sur support microforme, papier, électronique et/ou autres formats.

L'auteur conserve la propriété du droit d'auteur et des droits moraux qui protège cette thèse. Ni la thèse ni des extraits substantiels de celle-ci ne doivent être imprimés ou autrement reproduits sans son autorisation.

In compliance with the Canadian Privacy Act some supporting forms may have been removed from this thesis.

While these forms may be included in the document page count, their removal does not represent any loss of content from the thesis.

Conformément à la loi canadienne sur la protection de la vie privée, quelques formulaires secondaires ont été enlevés de cette thèse.

Bien que ces formulaires aient inclus dans la pagination, il n'y aura aucun contenu manquant.

Reproduced with permission of the copyright owner. Further reproduction prohibited without permission.

Abstract

The energy flux at the substrate during physical vapour deposition has been shown to influence the microstructure of the growing thin films. For many applications in microelectronics and nanotechnology, even slight changes in the amount of the deposited energy can affect the nanostructure and the suitability of the film. To meet the challenges of fabricating films with the desired properties, a more complete knowledge of the energy flux towards the substrate is required.

In this thesis, both the experimental and theoretical determination of the energy flux in a direct current (dc) magnetron sputtering system is explored. Experimental energy flux was determined by measuring the transient response of a micro-machined polysilicon sensor. The steady state energy flux at the substrate was measured to vary from 9.6 to 46 mW/cm^2, and 14 to 114 mW/cm^2 at a substrate-target distance of 10.8 cm depending on the magnetron power (75 – 300 W) and gas pressure for aluminum (Al) and copper (Cu) respectively. The energy deposition efficiency depends on pressure, distance and the type of material.

Reproduced with permission of the copyright owner. Further reproduction prohibited without permission.

Models have been developed for the deposition rate of sputtered flux, and the energy deposited onto an un-biased substrate. The models compare well with the experimentally determined values for aluminum (Al) and copper (Cu). The energy per deposited atom is determined, and it trends towards being independent of power and pressure, especially at high magnetron powers. At low powers, the energy per deposited atom increases with pressure due to lower deposition rates. The energy per atom also increases with spatial distance. However, for those regions not too far from the target, the energy per atom is independent of the spatial distance. For the magnetron system used, plasma effects are shown to be important in determining the total energy flux to the substrate. Contributions of the electrons and thermal radiation from the target region are included in the model.

Numerical simulation of gas heating is also carried out. Thermal conduction of heat from the heating sources has been identified as the major issue with gas heating. The type of sputtering gas, target material, substrate plane location and pressure determines the extent of gas heating. Sputtered particles have been shown to be the main source of energy for heating the gas. Contributions from electrons, ions and reflected neutrals are only significant at high pressures.

Reproduced with permission of the copyright owner. Further reproduction prohibited without permission.

Acknowledgement

I am grateful to my research supervisor, Dr. S.K. Dew for the financial support and professional guidance during the course of the study. The assistance of the members of Dr. Dew's group, supervisory committee, and staff of the University of Alberta Nano-fabrication facility is greatly acknowledged. Keith Franklin has been of great help especially in the area of wire bonding of the micromachined chip to the package. I am thankful to Dr. A.M. Robinson, Yuan Ma, Keith Brown and Canadian Microelectronics Corporation for providing the chips used in the study.

I am also grateful for the constant moral support and encouragement from my family and friends. To Itohowo, Idongesit, Oto-Abasi, Akemini, Enefiok thank you for the understanding. Finally, I would like to thank the University of Alberta, University of Uyo, Natural Sciences and Engineering Research Council of Canada and all others who have provided the necessary support.

Reproduced with permission of the copyright owner. Further reproduction prohibited without permission.

Table of Contents

1 Introduction **1**

1.1 Thin Film Deposition Techniques 5

1.2 Sputtering Process 8

1.2.1 Description of the Physical Process 11

1.3 Effect of Energy on Thin Film Microstructure 18

2 Theory of Energy Flux in a Sputter Deposition System **24**

2.1 Introduction 24

2.2 Sources of Energy 25

2.2.1 Sputtered Particles 26

2.2.2 Reflected Neutrals 27

2.2.3 Plasma Irradiation 28

2.2.4 Charged Particles 28

2.2.5 Thermal Radiation 29

2.3 Particle Matter Interaction 30

2.4 Transport Process 33

2.4.1 Sputtered Atoms and Reflected Neutrals 33

2.4.2 Electrons and Ions 37

Reproduced with permission of the copyright owner. Further reproduction prohibited without permission.

2.5 Heat Transfer 38

2.6 Effect of Gas Phase Collisions: Gas Heating and Rarefaction . . 42

2.7 Scaling of Particle Flux and Kinetic Energy with Pressure and Distance 47

3 Calorimeter and Experimental Design **53**

3.1 Calorimeter 53

3.2 Energy Flux Measurement 54

3.3 Micromachined Temperature Probe 58

3.4 Characterization and Calibration of the Sensor 62

3.4.1 Temperature Coefficient 62

3.4.2 Heating Mode: Dynamic Response 64

3.4.3 Sensing Mode 71

3.5 Experimental Design 75

4 Process Conditions and Results **78**

4.1 Process Conditions 78

4.2 Results 80

4.2.1 Effect of Applied Power 80

4.2.2 Effect of Pressure 81

4.2.3 Effect of Substrate-target Distance 83

Reproduced with permission of the copyright owner. Further reproduction prohibited without permission.

4.2.4 Effect of Target Material 85

4.2.5 Effect of Substrate Bias 86

4.2.6 Determination of Plasma Properties 87

4.3 Analysis of results 88

4.3.1 Power and Pressure on Transient Energy 89

4.3.2 Energy Flux as a Function of Bias Potential 94

4.3.3 Total Energy per Deposited Atom 96

5 Theoretical Models and Discussions **102**

5.1 3-D Deposition Rate Model 102

5.1.1 Fast Moving Particles 107

5.1.2 Slow Moving Particles 112

5.1.3 Results and Discussions 114

5.2 Energy Model 128

5.2.1 Total Energy Flux at the Substrate 138

5.2.2 Total Energy per Deposited Atom 142

6 Numerical Simulation of Gas Heating **152**

6.1 Numerical Model 153

6.2 Results and Discussions 158

Reproduced with permission of the copyright owner. Further reproduction prohibited without permission.

6.2.1 Effect of Pressure 160
6.2.2 Effect of Target Material 164
6.2.3 Effect of Substrate Plane Location 166
6.2.4 Effect of Gas Type 169
6.2.5 Effect of Target Location 171
6.2.6 Effect of Target Size 172
6.2.7 Individual Contributions to the Gas Heating 175

7 Conclusions and Recommendations **178**

7.1 Conclusions 178

7.1.1 Micromachined Temperature Probe 179
7.1.2 Deposition Rate 179
7.1.3 Total Energy Flux at the Substrate 181
7.1.4 Total Energy per Deposited Atom 182
7.1.5 Simulation of Gas Heating 183

7.2 Recommendations for Further Work 184

8 Bibliography **185**

Reproduced with permission of the copyright owner. Further reproduction prohibited without permission.

List of Tables

4.1 Mean Discharge Voltage and Current (Al at 5 mTorr) 79

4.2 Mean Discharge Voltage and Current (Al at 10 mTorr) 82

4.3 Mean Discharge Voltage and Current (Cu) 86

4.4 Bias Potential Effect on Sensor Resistance 87

4.5 Contributions to the Total Energy per Deposited Al Atom (Expt) . . 101

5.1 Contributions to the Total Energy per Al Atom (Model) 150

5.2 Contributions to the Total Energy per Cu Atom (Model) 151

6.1 Relative Gas Density (Sputtering of Al & Cu) 166

6.2 Contributions to the Gas Heating 177

Reproduced with permission of the copyright owner. Further reproduction prohibited without permission.

List of Figures

1.1 Integrated Circuit Metallization Scheme 3

1.2 Sputtering Process 9

1.3 Magnetron Sputtering System 11

1.4 Representation of Linear Collision Cascade 13

1.5 Depth of Penetration of Ions in Matter 13

1.6 Structural Zone Models 23

1.7 Thornton's Zone Models 23

2.1 Representation of Energy Sources 25

2.2 Angular Distribution of Sputtered Atoms 32

2.3 Sketch of Collision between Atoms 35

2.4 Thermal Radiation between Finite Bodies 41

2.5 Changes in Gas Temperature with Pressure 45

2.6 Kinetic Energy of Sputtered Atoms 48

2.7 Zero Pressure Deposition Efficiency 51

2.8 Distance Dependent Deposition Efficiency 52

3.1 Micromachined Temperature Probe Layout 60

3.2 Photograph of Sensor 2 Cell 61

Reproduced with permission of the copyright owner. Further reproduction prohibited without permission.

3.3 Temperature Dependent Resistance of sensors 1 & 2 66

3.4 Sensor 1 Response 65

3.5 Changes in Sensor Resistance (Heating and Cooling) 68

3.6 Effect of Applied Power on Sensor Resistance (Heating Mode) . . 69

3.7 Effect of Gas Pressure on Sensor Resistance (Heating Mode) . . 71

3.8 Effect of Pressure on Thermal Resistance of Sensor 72

3.9 Cooling Curve Response of Sensor (Sensing Mode) 74

3.10 Schematic Diagram of Experimental System 76

3.11 Schematic Views of 24-pin DIP Package 77

4.1 Effect of Magnetron Power on Sensor Response during Al Deposition 81

4.2 Effect of Pressure on Sensor Response during Al Deposition . . 83

4.3 Effect of Substrate-target Distance on Sensor Response 84

4.4 Sensor Response during Deposition of Cu 85

4.5 Plasma Characteristics 88

4.6 Transient Energy Flux at the Substrate (Al Deposition) 91

4.7 Steady State Energy Flux at the Substrate (Al Deposition) 92

4.8 Steady State Energy Flux at the Substrate (Cu Deposition) 94

4.9 Bias Potential Effect on Energy Flux at the Substrate 96

4.10 Total Energy per Deposited Al Atom 99

5.1 Current – Voltage Characteristics of the DC Magnetron Discharge . . 104

Reproduced with permission of the copyright owner. Further reproduction prohibited without permission.

5.2 Dependence of Admittance Factor on Pressure 105

5.3 System Geometry (Deposition Rate Model) 111

5.4 Deposition Profile of Sputtered Al Atoms 116

5.5 On-axis Deposition Rate of Al Atoms as a Function of Etch Track . . 117

5.6 Dependence of Film Uniformity on Etch Track (NT) 118

5.7 Dependence of Film Uniformity on Etch Track (ST) 119

5.8 Dependence of Film Uniformity on Etch Track (LT) 120

5.9 Effect of Substrate Location on Film Uniformity 121

5.10 Pressure Dependent On-axis Deposition Rate of Al & Cu 123

5.11 Deposition Rate Profile of Cu 124

5.12 Power Dependent On-axis Deposition Rate of Al & Cu (system 2) . . 125

5.13 Power Dependent On-axis Deposition Rate of Al (system1) . . 126

5.14 Fraction of Diffused Flux of Al & Cu Atoms 128

5.15 Average Kinetic Energy of Al & Cu atoms 130

5.16 Pressure-distance product dependent Kinetic Energy of Al 131

5.17 Temperature of Target Shield during Sputtering of Al 137

5.18 Steady State Energy of Deposited Al 139

5.19 Steady State Energy of Deposited Cu 140

5.20 Substrate-target distance dependent On-axis Energy Flux 141

5.21 Total On-axis Energy per Deposited Atom 143

Reproduced with permission of the copyright owner. Further reproduction prohibited without permission.

5.22 Effect of Size of Target and Etch Track on the Energy per Atom . . 144

5.23 Individual Contributions to the Total Energy per Al Atom 148

5.24 Individual Contributions to the Total Energy per Cu Atom 149

6.1 3-D Nodal R-C Network 155

6.2 Effect of Grid Size on Gas Temperature 159

6.3 Longitudinal Gas Temperature Profile (Al) 161

6.4 Transverse Gas Temperature Profile (Al) 162

6.5 Longitudinal Gas Temperature Profile (Cu) 163

6.6 Transverse Gas Temperature Profile (Cu) 164

6.7 Effect of Location of Substrate Plane on Gas Temperature 167

6.8 Effect of Gas Type on Longitudinal Gas Temperature Profile (Cu) . . 170

6.9 Temperature Profile of an Off-axis Sputter Source 172

6.10 Temperature Profile of Large Target Size 174

Reproduced with permission of the copyright owner. Further reproduction prohibited without permission.

Chapter 1

Introduction

Thin films are a key enabling part of most micro- and nanotechnologies. These films consist of micro- to nanometer thick layers of functional material coated onto a “base” material usually referred to as the substrate. The films may be electrically conducting or insulating, magnetic, hard, optically or chemically active, depending on the applications. They are usually formed from the condensation or reaction of free atoms or molecules [1]. The source of these free particles may be gases or solids from which they are released through an energetic process. A variety of different techniques are available, depending on the materials and required properties [2].

The applications of thin films are numerous. Some of these include conductors, insulators and diffusion barriers for microelectronics, antimicrobial or biocompatible coatings for biomedicine, catalytic or barrier coatings for high and low index chemical industry, hard coatings for tools or mechanical application, optical coating, magnetic coatings for data storage and recovery, and decorative coatings for toys, automobiles and other

Reproduced with permission of the copyright owner. Further reproduction prohibited without permission.

manufactured products [2–4]. Some of these applications lend towards miniaturization and integration, and/or reduction in the overall weight. In fact, thin film technology is a critical part of the multi-hundred billion dollars integrated circuit industry, magnetic storage industry, optics industry, etc. In all these cases, the addition of a small amount of film material dramatically changes the functionality of the substrate.

A particularly important consumer of thin films is the microelectronics industry. Microelectronics has become a leading technological force in the present world economy as a result of the invention of transistor in 1947 [3] and the fabrication of more and more components on a single chip (integrated circuit). Scales of Integration has progressed from the small scale (SSI) in 1958 through medium, large to now very large and ultra large scales [5,6] as a result of the demand for faster and more powerful integrated circuits. With the advancement in VLSI technology, chips now contain tens of millions of transistors [7]. The increasing number of transistors per chip leads to increasing complexity and requires decreasing feature size. These transistors would be useless if they are not interconnected to form functional circuits. These interconnects are formed from very thin layers of conductive metal which are deposited onto the silicon transistors in layers separated by insulation in a process referred to as metallization as hypothetically depicted in Fig. 1.1. The feature size of each interconnect must also be reduced along with the transistor size which poses additional challenges as the properties of the

Reproduced with permission of the copyright owner. Further reproduction prohibited without permission.

deposited films are affected. These reductions could only be achieved through a sustained improvement in manufacturing technology, especially with the present/future sub-100 nm technologies.

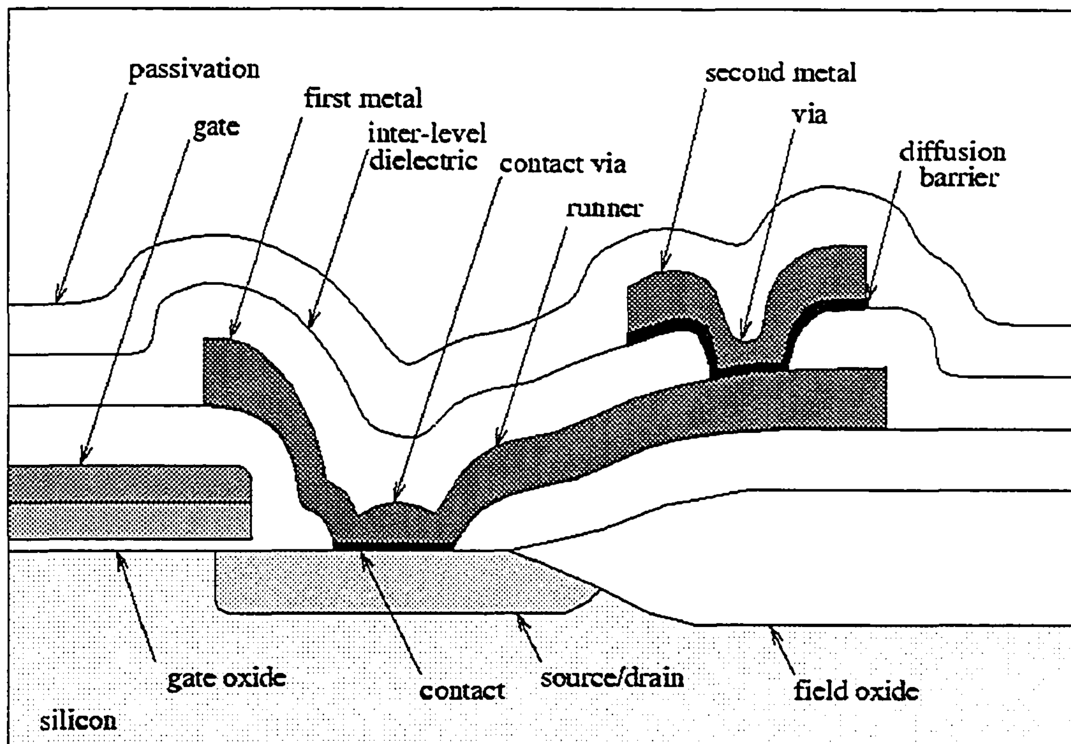

Fig. 1.1 Cross-section of a hypothetical IC structure with a two level metallization scheme, identifying the complexity of the structure and the various thin films. Intel Pentium 4 uses 65nm process, which incorporates 7 layers of metal [8]. Figure courtesy of S.K. Dew.

Reproduced with permission of the copyright owner. Further reproduction prohibited without permission.

Usually, the condensation of free atoms to form a thin film is followed by a more or less layered growth of the deposit. Depending on the deposition technique, the deposited material may not grow in a uniform manner, and may become faceted or develop columns, voids, grains and other inhomogeneities [2]. This implies that the internal structure of the thin films, "microstructure" is complex in nature. These microstructures determine the properties of the thin films [9] and are difficult to engineer. Researches conducted over the past years [10–29] have shown that microstructure and properties of the deposited film are influenced by the process parameters and conditions, as well as system geometry. The changes in the microstructure of the films as a result of the variation in the process parameters are largely attributed to the changes in the energy flux at the substrate [12], since the mobility of the impinging atom (adatom) and its ability to arrange in a low-energy state depends to a great extent on the deposition energy. Since the properties of the film clearly affect the film's suitability for a given purpose, it is important to study the energy flux to a depositing film and the role of the process parameters. In some cases, the transient behaviour may be of particular importance.

The purpose of this study is to measure the energy flux at the substrate, and relate the energy flux to the depositing conditions for a particular coating technique. In this chapter, thin films (applications and deposition techniques), sputtering as a deposition technique, and the role of process conditions on film microstructure are discussed. In Chapter Two,

Reproduced with permission of the copyright owner. Further reproduction prohibited without permission.

the theory of energy sources in a sputtering deposition process is discussed. Chapter Three discusses the methods of thermal energy measurements, and outlines the calibration and characterization of the calorimeter used in this study. The experimental results are presented in Chapter Four. A theoretical model is developed in Chapter Five to explain the sources of the thermal flux to the substrate, and compared to the experimental results. Numerical simulation of gas heating is presented in Chapter Six. Recommendations and final conclusions are presented in Chapter Seven.

1.1 Thin Film Deposition Techniques

As mentioned earlier, thin films can be deposited using a variety of techniques and processes. Some of these processes are physical vapour deposition (PVD), chemical vapour deposition (CVD), and electro-chemical deposition (ECD). CVD processes consist of high pressure CVD, low pressure (LPCVD), plasma enhanced (PECVD) and metal organic (MOCVD). The major advantages of CVD processes are the frequent near-conformality of the deposited thin films and the consequent ability to fill vias having small diameters and high aspect ratios [30,31]. A via as shown in Fig 1.1, is a hole etched through insulation material between metal layers, so as to create a conducting path when filled with conductive material. ECD processes have also been shown as a good interconnect fill technology for ULSI metallization [32–37]. These processes consist of

Reproduced with permission of the copyright owner. Further reproduction prohibited without permission.

electroless deposition and electro-plating. A major challenge for both CVD and ECD, however, is finding appropriate reaction chemistries and conditions. PVD processes consist of evaporation, ion plating and sputtering [38]. Unlike CVD, PVD is a highly non-equilibrium process, such that the coatings may be deposited onto virtually any substrate. With the versatility of PVD technology, a wide variety of inorganic materials – metals, alloys, compounds and mixtures thereof can be deposited on a variety of substrates.

The choice of the deposition technique depends on the material and the type of application. For integrated circuit (IC) metallization, there has been no material or process with all the ideal characteristics. Sputtered aluminum has historically been used over the years as the contact metal on devices as well as the higher-level interconnection [3,39] with CVD SiO_2 insulation. With the evolution of ULSI, where several multilevel interconnections are required, emphasis is now directed towards ECD copper, Cu (lower resistivity) and CVD or spin-on low dielectric materials [40–46]. For instance Intel Pentium 4, a 65 nm technology process, uses 7 layers of Cu [8], and virtex™ II Pro FPGA uses 9 layers of copper [47]. Nonetheless, PVD Al will continue to be used for some IC interconnections/wirings (especially for the low-cost, high-volume DRAM market) for years to come [48], and PVD Cu seed layers, adhesion layers and diffusion barriers are still required even for CVD and ECD processes.

Reproduced with permission of the copyright owner. Further reproduction prohibited without permission.

The most widely used PVD technique for microelectronics is sputtering in a plasma environment [2,17,49–56]. PVD technology first came into existence when Faraday in 1857 exploded metal wires in a vacuum [38]. This then found numerous applications in thin film deposition [51]. To form any deposit, three steps must be considered, namely, (a) vaporization of the material to be deposited, (b) transport of the vapours between the source and the substrate, and (c) condensation of the vapours followed by nucleation and growth of the film. In PVD, the steps can be independently influenced to obtain the desired film properties [38].

1.2 Sputtering Process

Sputtering is a means of causing the ejection of atoms from a surface by bombarding it with energetic ions [57]. It involves momentum exchange between the incident ions and the particles of the target material. The sputtered material is ejected primarily in atomic form. The substrate for the sputtered material to be deposited on is placed some distance from the target. Sputter deposition is a vacuum coating process. However, the source of the bombarding ion is plasma of an inert gas, such as argon, which is introduced into the evacuated chamber at a certain low pressure (between 1 and 100 mTorr) depending on the type of sputtering process. A glow discharge (electric discharge) helps in ionizing the

Reproduced with permission of the copyright owner. Further reproduction prohibited without permission.

working gas to produce the plasma. To accelerate the positive gas ions towards the target, it is maintained at a negative potential (~-500 V).

Sputtered films are said to have properties which are often superior to those produced by evaporation sources because of the higher kinetic energy with which the sputtered particles are ejected from the target. This high energy has a favourable influence on film adhesion and growth [58,59]. The average initial energy of sputtered atoms is in the range of 10 – 40 eV, whereas evaporated atoms typically have energies of 0.2 to 0.3 eV [60]. Other advantages of sputtering over evaporation include better trench filling capabilities, and process modification (such as ionized or reactive deposition). Apart from the energy of the sputtered atoms, the plasma is a potential source of energy to the growing film. For instance, the ultraviolet radiation from argon plasma has energy of about 12 eV, and the visible radiation has energy of about 2 eV. Generally, the sputtering process is considered a relatively high-energy process compared with many coating technologies. The major disadvantage of sputtering is that of the equipment cost.

In sputtering processes, ionized gas particles (usually from inert gases such as argon) are accelerated by an intense electric field in the cathode fall region (between positive space charge and target surface) of the glow discharge [38,55,61] towards the target (cathode). As illustrated in the sketch of Fig 1.2, these energetic ions knock off the surface atoms of

Reproduced with permission of the copyright owner. Further reproduction prohibited without permission.

the target. Some of the gas ions are reflected as neutrals. Secondary electrons are also ejected, and help in maintaining the discharge. They are accelerated away from the target by the high field and undergo ionizing collisions in the plasma. In a magnetron discharge, these electrons are deflected by imposed magnetic fields and partially confined near the cathode surface thereby improving the ionization efficiency.

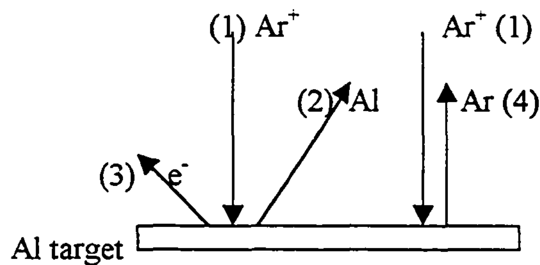

Fig. 1.2 Sketch of a sputtering process. On ions bombardment (1), target particles (2) and electrons (e^-) (3) are ejected. Some neutralized ions may be reflected (4).

Between the target and the substrate are the plasma, gas atoms, emitted (sputtered) atoms from the target, and the reflected neutral gas atoms [62,63]. Thus, as the sputtered atoms travel towards the substrate, they collide with other particles and are scattered [64–67]. Some are ionized by electron collisions, while most remain as neutrals [62]. The ratio of the ionized sputtered atoms to the neutral atoms depends on the plasma density, the distance between the target and the substrate, the magnetron power, and the electron temperature [68–74]. The common sputtering processes available can be divided into three regimes. These are: (a) low pressure, typically below 0.1 mTorr – characteristic of

Reproduced with permission of the copyright owner. Further reproduction prohibited without permission.

most ion-beam and enhanced magnetron sputtering processes or electron cyclotron resonance (ECR) plasmas [75,76], (b) intermediate pressure, typically in the range of 0.5 to 30 mTorr – characteristic of most magnetron and some radio-frequency (rf) diode sputtering processes [1,76], and high pressure, typically above 50 mTorr – characteristic of most rf – diode and all d.c. – diode sputtering systems [1,40,75–78]. In the diode sputtering system, there is no magnetic field arrangement as is obtained with magnetron system. In the rf sputtering system, rf voltages are capacitively coupled across a non-conducting targets, so as to remove charge accumulations on the target surface.

The Magnetron sputtering process is the most widely used sputtering process in industrial settings [55,70]. This is especially true in microelectronics, such as for IC metallization, magnetic and magneto-optical coatings used in hard drives and other magnetic storage media, optical coatings, biomedical coatings, automotive manufacture and advanced food packaging. The basic magnetron sputtering process is shown in Fig. 1.3.

Reproduced with permission of the copyright owner. Further reproduction prohibited without permission.

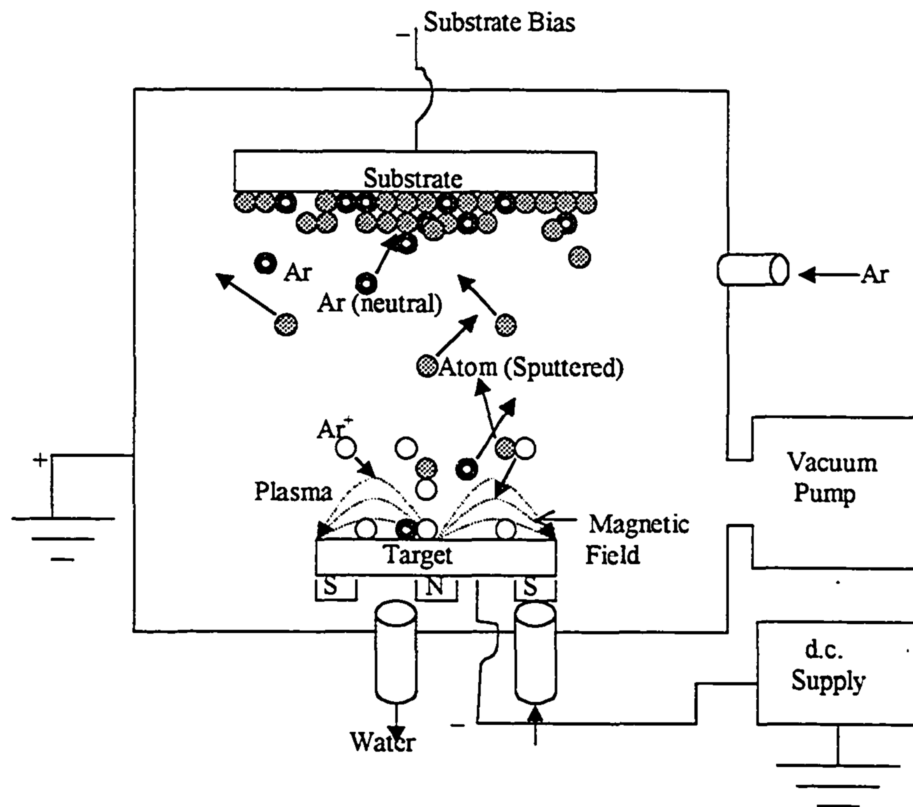

Fig. 1.3 Basic magnetron sputtering system. A potential applied to the target creates a glow discharge plasma. Ions from the plasma are accelerated into the target and cause target material to be ejected into the vacuum chamber filled with low-pressure argon gas. Magnets confine the plasma near the target for greater efficiency.

1.2.1 Description of the Physical Process

Sputtering is usually done in a plasma environment. Plasma is a collection of charged and neutral particles resulting from the partial ionization of atoms or molecules of a gas

Reproduced with permission of the copyright owner. Further reproduction prohibited without permission.

generally by an external electric field [79]. The essential mechanisms in plasmas are excitation, relaxation, ionization and recombination, and may be characterized in terms of macroscopic variables such as pressure, density and temperature.

The target (source of the thin film material) is usually biased negatively to accelerate the argon ions from the plasma towards it. The incident ion knocks atoms out of their equilibrium sites in the target, launching them ballistically through the material to undergo further collisions, which eventually may cause the ejection of atoms from the surface of the target. Thus, the bombardment of the ions on the target induces a collision cascade within the target material [80]. The number of atoms participating in a collision cascade is dependent primarily on the available energy [81]. The average number of ejected atoms per bombarding ion is referred to as the sputtering yield, Y_s [82]. If the density of recoils is sufficiently low, such that most collisions involve one moving and one stationary particle, then the collision cascade is linear. Sigmund's schematic depiction of the linear collision cascade is shown in Fig. 1.4. The yield depends on the energy of the bombarding ion, masses and types of incident and target atom species, and the binding energy of the target material [83–85]. For ion energies between 200 and 600 eV, the yield increases linearly with the ion energy [83].

Reproduced with permission of the copyright owner. Further reproduction prohibited without permission.

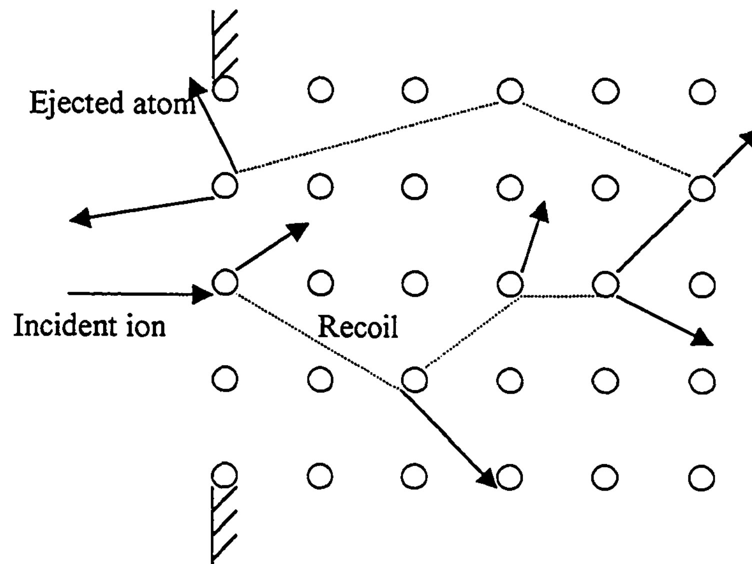

Fig. 1.4 Schematic representation of linear collision cascade.

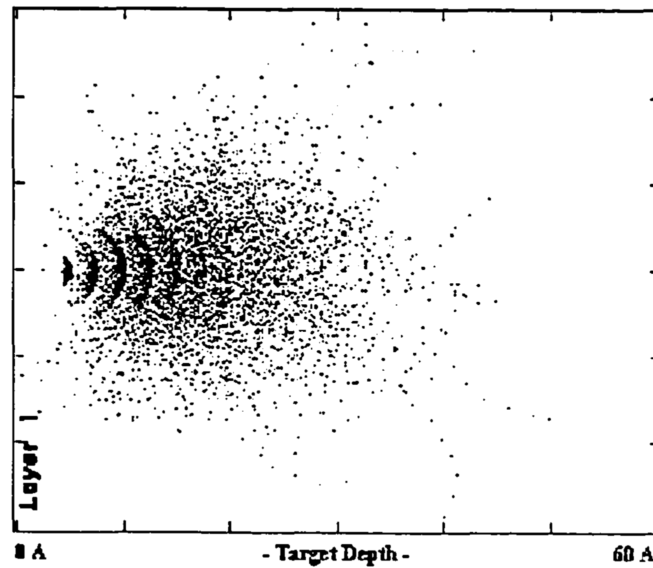

Fig1.5 Depth of penetration of ions in matter as a result of collision cascades.

Reproduced with permission of the copyright owner. Further reproduction prohibited without permission.

From the collision cascade model, it is evident that the ejection of a sputtered particle from a target requires a sequence of collisions. Thus, though sputtering is a surface event, the energy of the incident ion is partitioned over a region of the target material that may extend 50 to 60 Å or more below the target surface [61]. Fig. 1.5, which was generated using the SRIM 2000.39 program [86], shows the longitudinal extent to which normally incident ions may reach as a result of this collision cascade The source of the bands shown that figure is not known, and may probably be due to assumptions made in the calculations involved, which of course is outside the scope of the present study. However, sputtering momentum exchange occurs primarily within a region extending only about 10 – 15 Å below the surface [87].

As the incident ion hits the target, a fraction of the kinetic energy of the incident particle is transferred to the target atoms. During the collision cascade, the recoils have a distribution of kinetic energies, with average energy falling continually with the number of collisions. The range of recoils is relatively small compared with the range of the initial projectile. Only those recoils, which are near the surface (within the escape depth), will be able to escape. To escape, the recoils must have sufficient energy to overcome the potential barrier, usually referred to as the binding energy or heat of sublimation, U_b. The direction of travel of the recoils would also determine the fraction of those with sufficient

Reproduced with permission of the copyright owner. Further reproduction prohibited without permission.

energy, which are also close enough to the surface to finally escape from the surface of the target. This fraction is a function of depth at which the recoils are created. The ejected particles have kinetic energies, which are only a small fraction of the incident ion energy. The energy and the angle relative to the normal of the incident ions determine the energy and angular distributions of the ejected particles [61,88].

Sputtered atoms are emitted from the surface in a mostly random manner. The angular distribution is generally described by a cosine function, normalized to the emission at the surface normal. However, depending on the choice of incident particle, energy, sample species and orientation, departures from this cosine distribution are routinely observed [88–90]. It is has also been shown that the form of the erosion profile affects the angular distribution of the sputtered atoms [91,92]. The erosion profile depends on the arrangement of the magnets of the magnetron.

If the mass of the incident ion is less than that of the target material, it is possible that the ion will be reflected backward (after neutralization) in a single collision, and the energy of the reflected neutral may be a significant fraction of its initial energy. When the target mass is less than that of the incident ion, the ion can be reflected backward only as a result of more than one collision and this reflection therefore is less likely to occur. The ions are neutralized just before hitting the target. These reflected neutrals still retain

Reproduced with permission of the copyright owner. Further reproduction prohibited without permission.

significant energy, and can have long path lengths (in tens of centimetres) between collisions with the sputter gas atoms. Hence, they suffer fewer collisions and lose that energy more slowly than do the depositing atoms. If they hit the substrate, they may deposit a significant energy onto it.

As stated earlier, the ejected particles collide with other particles (especially gas atoms) on their way towards the substrate and lose part of their initial energy. Depending on the number of collisions, the energy of some of the sputtered atoms is reduced to the thermal energy of the gas before they are deposited onto the substrate. Those atoms whose energies are reduced to the thermal energies are said to be thermalized. According to Westwood [93], sputtered atoms can be considered thermalized after six to ten collisions with the background gas, but this depends strongly on the relative masses of the gas and the sputtered atoms. Fast atoms make fewer collisions than the thermalized ones, since their path lengths are longer [94].

Thermalization by gas scattering is an important process in sputter deposition to control the energy deposition by the sputtered atoms themselves [65]. An accurate knowledge of the energy spectrum of the atoms ejected from the surface of the target, the decrease of collision cross-section with increasing energy, the scattering of atoms on collision, and the range of path lengths between collisions are essential in calculating thermalization

Reproduced with permission of the copyright owner. Further reproduction prohibited without permission.

events [28]. Usually, the flux of atoms emitted from the cathode is assumed [16,53–56,62,95–97] to obey the theoretical expression for the ejection energy and angular distributions derived by Thompson [98]. However, at low ion energies, it has been shown that the energy and angular distributions of sputtered atoms deviate from the Thompson's model [61,88], which assumes a well-developed collision cascade. But at ion energies of above 400 eV, the distributions approximate the Thompson's model [61].

The number of gas phase collisions the ejected particles experience depends on their energy. Collision cross-section has been shown to decrease considerably as energy is increased from 10 to 100 eV [94]. The description of collisions between atoms requires the knowledge of the interaction potential between these atoms, as this determines the cross-section scattering angles, and the energy lost in a collision. A number of different interaction potentials between atoms are available in the literature [99–104]. The screened Coulomb potentials, based on the Thomas-Fermi model of an atom, present a realistic view of atomic interactions [61,100,105]. The range of path lengths between collisions are assumed [106] to follow a Poisson distribution and take account of the fact that more energetic atoms travel further and transfer disproportionately more energy to the substrate [55,61,107].

Reproduced with permission of the copyright owner. Further reproduction prohibited without permission.

The energy lost in all the collisions is transferred to the background gas. This causes heating and rarefaction of the gas, thereby changing its scattering properties in a non-linear and non-uniform manner.

1.3 Effect of Energy on Thin Film Microstructure

Energy exchange within the sputtering system is determined by two sets of parameters, external and internal. The external parameters are the controllable experimental factors such as power, voltage, current, dc or rf excitation, the geometry and the composition/pressure of the background gas. The internal parameters are factors such as the degree of ionization, potential drop in the plasma sheath, masses of the component particles and the free paths of the various different particles. These internal parameters influence the flux of particles as well as the energy flux towards the substrate. The film microstructural evolution is primarily determined by these internal parameters [108]. The two sets of parameters are coupled in a complicated manner.

Energy is deposited onto the substrate from various sources. Some of these sources include: (a) the kinetic energy and the energy of condensation of the sputtered particles, (b) the energy of the reflected neutrals, (c) the plasma irradiation, (d) the energy from

Reproduced with permission of the copyright owner. Further reproduction prohibited without permission.

charged particles (such as electrons) at the substrate region, (e) thermal radiation from heated objects in the system.

This deposited energy heats up the substrate, and causes its temperature to rise. This affects the surface mobility of the deposited atoms, and hence the properties of the resulting thin film. Film growth can be divided into: (a) nucleation, (b) growth of the nuclei and (c) formation of more or less connected networks with potentially some interfacial voids [109]. When adatoms impinge on a surface, they may have a degree of mobility on the surface before they nucleate and condense [110–112]. During film growth, adsorbed atoms (adatoms) redistribute by surface diffusion with respect to already existing film nuclei on the substrate. Short diffusion lengths lead to larger numbers of disordered and separated nuclei. Longer lengths result in more continuous films with larger polycrystallites. The diffusion length, L, is a strong function of the substrate temperature, and is given by the Arrhenius relation as:

$$L = \sqrt{Dt} \tag{1.1}$$

$$D = D_0 \exp\left(-{E_s}/{kT}\right) \tag{1.2}$$

Where D is temperature dependent diffusion coefficient, t is the mean time for surface diffusion and E_s is the activation energy for surface diffusion.

Reproduced with permission of the copyright owner. Further reproduction prohibited without permission.

From the above, it is evident that the properties of thin films may generally be temperature related. Energetic bombardment of the film by the deposited species, which causes the substrate temperature to rise, have been shown to alter the film properties such as stress, grain size, etc [12,14,15,17,19,113]. The density and energy of the plasma at the substrate region have been shown to also affect the properties of the deposited film [16,114,115]. Gas pressure, as a process parameter, affects the kinetic energy of the deposited species as well as the characteristics of the plasma, hence it may be said to have an important indirect effect on the microstructural evolution of the film.

Sputter deposited films may have tensile or compressive stress [14,19]. For a magnetron sputter deposited film, there often exists a transition pressure below which the coatings are in compression and exhibit high optical reflectances and low resistivities, while above the transition pressure the coatings are in tension and show decreased reflectances and increased resistivities. Muller, [17], in determining the evolving structure and stress of a sputter deposited film as a function of the kinetic energy of adatoms and fast neutrals arriving at the substrate showed that the initial increase in tensile stress may be linked to a microstructural change from micro-columnar growth to a more densely packed atomic network with closed micropores. The subsequent decrease in stress is attributed to a less defect-rich, better-ordered adsorbate structure formed at higher kinetic energies of the arriving species. Stress varies in a similar fashion as a function of the incident kinetic

Reproduced with permission of the copyright owner. Further reproduction prohibited without permission.

energy for both sputtered atoms and fast neutrals. Thus, certain energy is needed to increase atomic mobility at the surface, but too high an energy can cause a drastic increase in the defect formation [116]. Experiments have been conducted to illustrate how energetic ion-surface collisions can influence submonolayer island densities during growth of a Pt(111) surface by sputter deposition [23,117].

Movchan and Demchishin [118], classified evaporated films into three zones according to the ratio of the substrate temperature during deposition to the melting point of the film, T/T_m for various materials as shown in Fig. 1.6. Zone 1 structure at T/T_m <0.3 is characterized by low adatom mobility, rapid vapour quenching rates [119], and consists of columns with domed tops separated by voided boundaries. Zone 2 structure, corresponding to $0.3<T/T_m<0.5$, consists of densely packed columnar grains with smooth matte surface. Zone 3 structure, with $T/T_m>0.5$, occurs at high temperature where bulk diffusion process are active and consists of equiaxed grains with a bright surface. This zone model was later confirmed experimentally [12,119–122] and by simulations [123,124]. Thornton extended this to sputtering in the presence of energetic bombardment (for example, by reflected neutrals) by adding an additional axis to account for the effect of sputtering gas [12,120]. He showed that there exists a transition zone at T/T_m in the range 0.1 – 0.4, which consists of a dense array of fibrous grains separated by

Reproduced with permission of the copyright owner. Further reproduction prohibited without permission.

more nearly conventional grain boundaries. Such coatings are found to yield high lateral strengths [14,15].

Thornton's zone model is shown in Fig. 1.7. An increase in pressure increases the tendency of zone 1 structure to persist to higher values of the T/T_m. At higher T/T_m, the intergrain voids begin to fill in and the structure passes into transition zone (zone T), with relatively smooth "fine-domed" surface. The film features of zone 2 exhibit faceted surfaces and are independent of pressure. At the very high end of T/T_m, (zone 3), the faceted grains gradually changed to equiaxed structure, though a few faceted surfaces still remain. Generally, transition points were noted to vary because surface mobilities, heats of condensation and vapour pressures do not vary linearly with melting point [12].

Given the role of energy on the evolution of microstructure of the growing film, it is therefore of interest to study the various sources of energy in a typical deposition system such as magnetron sputtering, and the effect of the process parameters on these energy sources and on the total deposited energy at the substrate. The next Chapter will explore the theoretical understanding of the various energy sources, and how some of them scale with the process parameters such as pressure and distance.

Reproduced with permission of the copyright owner. Further reproduction prohibited without permission.

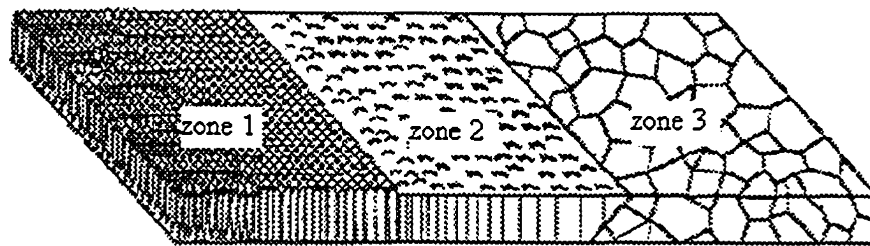

Temperature →

	Zone 1	Zone 2	Zone 3
Metals	$< 0.3T_m$	$0.3 - 0.45T_m$	$> 0.45T_m$
Oxides	$< 0.26T_m$	$0.26 - 0.45T_m$	$> 0.45T_m$

Fig.1.6 Structural zones in condensate.

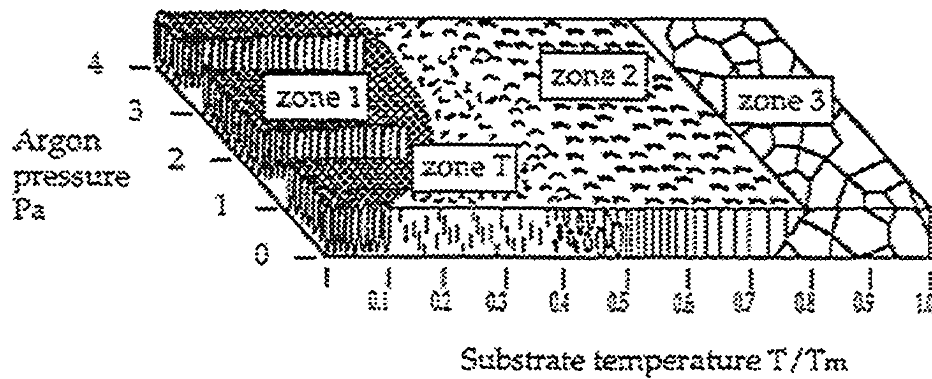

Fig. 1.7 Thornton's zone models showing the dependence of coating structure on substrate temperature and gas pressure [125]. Figure courtesy of R.N. Tait.

Reproduced with permission of the copyright owner. Further reproduction prohibited without permission.

Chapter 2

Theory of Energy Flux in a Sputter Deposition System

2.1 Introduction

Sputtered particles interact with the gas and plasma species through collisions. During this process, energy and momentum of the particles and those of the plasma species are exchanged. This energy transfer is complex. Understanding this is complicated, since it is not possible to increase or decrease the flux of only one kind of species by experimental means, and it is difficult to separate the influences of the different species on the substrate heating. As stated earlier, the energy exchange mechanism within a sputtering system is determined by two sets of parameters: external and internal. The external parameters can be controlled or adjusted. The internal parameters cannot be directly set. Since the interaction between the sets of the parameters determines the total energy flux to the substrate, its determination can be used as a tool to infer the inter-relationship between the parameters. Such determination may be done by understanding the sources of the energy flux within a sputtering system, how the energy is transported to the substrate, and the scaling of the energy with process parameters.

Reproduced with permission of the copyright owner. Further reproduction prohibited without permission.

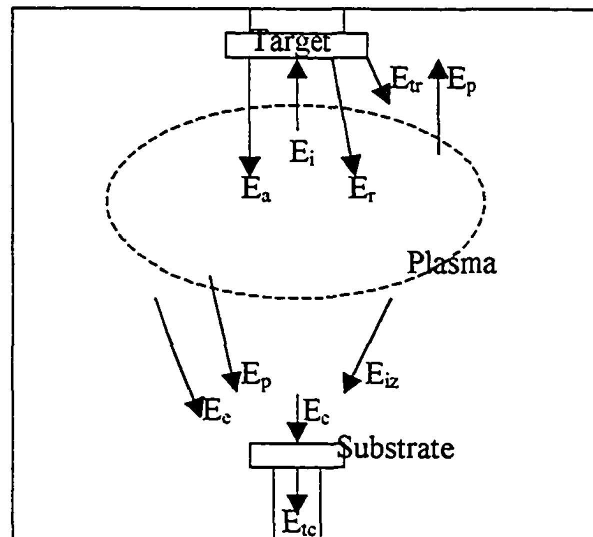

Fig. 2.1 Schematic representation of the sources of energy flux in a sputter deposition system. E is the energy flux, and the subscripts i, a, r, c, p, e, iz, tr and tc represent incident ion, sputtered particle, reflected neutral, condensation, plasma radiation, electron, positively ionized gas atom, thermal radiation, and thermal conduction through the substrate holder and probably to the gas.

2.2 Sources of Energy

Several sources contribute to the energy and momentum deposited into the gas and onto the substrate. The most essential are the sputtered atoms, energetic ions, reflected neutrals, electron bombardment, and emission (plasma irradiation) in the discharge space. These are schematically represented in Fig. 2.1. In certain cases, the hot cathode and the

Reproduced with permission of the copyright owner. Further reproduction prohibited without permission.

shield around the target (cathode), if not properly cooled enough, may contribute a significant amount of energy deposited within the chamber [126–128].

Thornton [129], considered four basic energy sources to the growing film, namely; (a) heat of condensation; (b) kinetic energy of the sputtered atom; (c) plasma radiation; (d) ion neutralization and reflection at the cathode. However, charged particles are also considered to contribute to the total energy at the substrate region, depending on the substrate bias potential [127,128,130,131], and the strength of the magnetic field of the magnetron.

2.2.1 Sputtered Particles

The contributions of the sputtered particles are mainly from the heat of condensation (energy given off by the particles during deposition onto the substrate) and the kinetic energy. The kinetic energy of the particles is determined by the average energy of the particles ejected at the target and their transport to the substrate. This energy is derived from the fraction of energy transferred from the incident ion on the target. This will be discussed further in section 2.3. In transport towards the substrate, the sputtered particles usually suffer some collisions with the gas and lose some of the kinetic energy. Since at typical deposition pressures, the mean free paths of theses particles are comparable to the

Reproduced with permission of the copyright owner. Further reproduction prohibited without permission.

target-substrate dimensions, small changes in conditions can have a large impact on transported kinetic energy.

2.2.2 Reflected Neutrals

The reflected neutrals are the neutralized gas ions, which are reflected after a small number of collisions in the target. The ions bombard the target surface with certain velocities. If the mass of the incident ion is less than that of the target material, it is likely that the ion will be reflected backward in a single collision, and the energy of the reflected ion may be a significant fraction of its initial energy. When the target mass is less than that of the incident ion, the ion can be reflected backward only as a result of more than one collision. The ions are neutralized just before hitting the target and are reflected as neutrals. These reflected neutrals still possess significant energy, and can have long path lengths (in tens of centimetres). They suffer fewer collisions and lose that energy more slowly than do the depositing atoms. If they hit the substrate, they may deposit significant energy onto it.

Reproduced with permission of the copyright owner. Further reproduction prohibited without permission.

2.2.3 Plasma Radiation

This is the energy emitted within the plasma as a result of the excitation and ionization events. These events are said to be caused by electrons with energies above the inelastic collision cross section threshold [129]. The average energy spent by an electron in making an ion is about 26.4 eV for argon [132]. The difference between this energy and the ionization energy of the gas (15.8 eV for argon) is radiated from the plasma. The amount of energy lost from the plasma by radiation depends on the population of the excited levels. Ionizing low-pressure argon plasma has been reported to have over-populated excited levels [ref: 133 and references therein]. The contribution of this energy to the total energy flux is determined by the sputtering yield and gas pressure.

2.2.4 Charged Particles

As stated earlier, charged particles have been shown to also contribute significantly to the total energy at the substrate region, depending on the substrate bias potential. At potentials higher than the floating potential, positive ions have been shown to contribute an insignificant amount of energy to the growing film [130,131]. When the substrate is at the plasma potential, electrons have been shown to contribute about 29% of the total energy per deposited particle, at 5 mTorr in one direct current (dc) magnetron sputtering

Reproduced with permission of the copyright owner. Further reproduction prohibited without permission.

system [127]. It has also been shown that, for another dc magnetron sputtering system at gas pressure of about 10 mTorr, with an escape probability of high energetic electrons of the order of 1% from the confinement of the magnetic field, about 50% of the total energy is transported by electrons to the coating [131]. However, the energy due to the electrons depends on the strength of the magnetic field of the magnetron, magnetron power and gas pressure as well as on the gas-target species. The contributions of the ions to the total energy flux are generally considered when the substrate potential is lower than the floating potential. The results of these references [127,128,131] indicate that the importance of electrons to the deposited energy at the substrate should not be ignored if an appropriate model for the determination of the deposited energy is to be obtained.

2.2.5 Thermal Radiation

Though the target may be water cooled, the thermal link between the shield around the target and the cooling surface may be weak. A weak thermal link will cause a significant difference in temperature between the surfaces. This may result in a significant amount of thermal radiation towards the substrate depending on the difference in temperature between the substrate and the hot body. In some cases, to avoid the effect of thermal radiation, measurements of the energy deposited within the chamber are done within a few minutes of switching on the plasma [130]. At steady state, radiation from the cathode

Reproduced with permission of the copyright owner. Further reproduction prohibited without permission.

can be a significant source of energy in a sputtering system [127,128,134,135]. In this study, thermal radiation is included in the model for the determination of energy deposited at the substrate

2.3 Particle Matter Interaction

As the ions bombard the cathode, some of their energies are transferred to the lattice atoms. The fraction of energy transferred to the target from the projectile in a binary elastic collision is: [84,136]

$$T(\delta_{pr}) = \gamma(\cos\delta_{pr})^2 \tag{2.1}$$

$$\gamma = \frac{4M_g M_t}{(M_g + M_t)^2} \tag{2.2}$$

where M_g and M_t are the masses of the gas and target atoms respectively, and δ_{pr} specifies the angle of travel of the recoil with respect to the projectile's initial velocity vector. The initial energy distribution of the sputtered atom is usually assumed to obey the Thompson distribution [98]; this distribution is given by [137]:

$$f(E)dE = C\left(1 - \sqrt{\frac{U+E}{\gamma E_i}}\right)\frac{E}{(U+E)^3}dE \tag{2.3}$$

Where U is the binding energy of the target material, E_i is the average energy of the incident ions (which depends on the dc target voltage, V_t), and C is a normalization

Reproduced with permission of the copyright owner. Further reproduction prohibited without permission.

constant. The average ion energy for a typical magnetron plasma is proportional to the target voltage with the constant of proportionality close to unity for cases where the dark space thickness is considerably small compared to the mean free path for charge exchange collisions [138]. The Thompson distribution formula has been found to approximate the energy spectrum of sputtered atoms when the incident energy is high enough. Yamamura [61] showed that at 100 eV, the energy spectrum of copper atoms had a strong deviation from Thompson's distribution for all angles of incidence considered. At 400 eV, the energy spectrum of sputtered atoms approaches Thompson's energy distribution especially for oblique incidence of the ions. Thus, for energies higher than 400 eV, the Thompson distribution can be used as the initial conditions for sputtered atoms.

For a well-defined collision cascade, the spatial distribution is expected to follow a cosine distribution. However, depending on the incident energy and the target mass, the angular distribution may deviate from the cosine distribution for a normal incidence of bombarding ion [61,88,139–141]. Under-cosine distribution (enhanced emission at oblique angles) is usually obtained at low ion energy [88], often complicated by crystallographic orientations. As the ion energy increases, the distribution changes and approaches a cosine distribution, and may be transformed to over-cosine (higher emission near the surface normal). Fig. 2.2 shows a typical sketch of this transformation for

Reproduced with permission of the copyright owner. Further reproduction prohibited without permission.

varying ion incident energy. As the energy decreases, the shape of the distribution changes to an under-cosine (heart-like) shape at low ion energies. This implies that, even in the absence of collision, the deposition efficiency at some distance from the target would be ion energy dependent. This will have an effect on the deposition rate modeling.

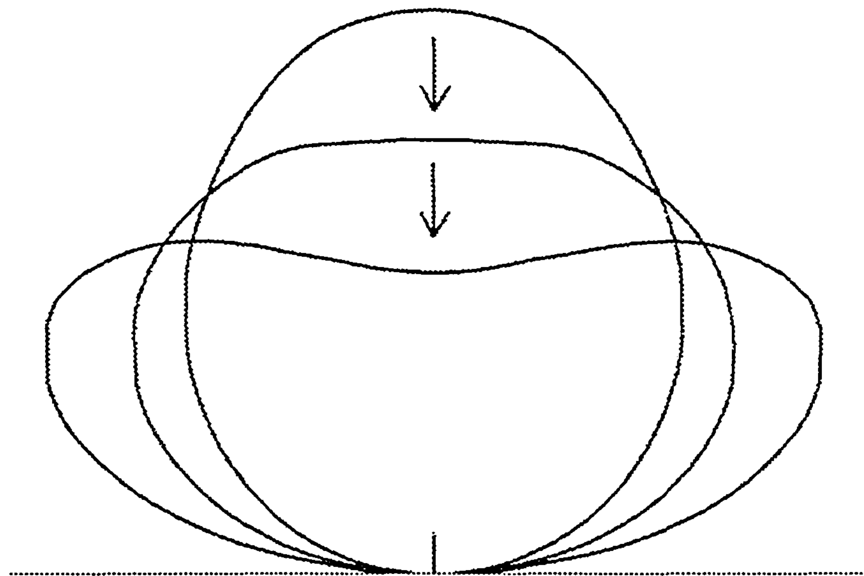

Fig. 2.2 Sketch of the dependence of the angular distribution of sputtered atoms on the incident ion energy for normal incidence. The arrows show how the distribution changes when ion energy decreases [88].

Reproduced with permission of the copyright owner. Further reproduction prohibited without permission.

2.4 Transport Process

Energetic particles created at the cathode and within the plasma move randomly between the cathode and the substrate. These particles can collide with each other, but most collisions are with background gas molecules. Because the particles coming from the cathode generally have greater energy than the background gas, on the average there is a net transfer of energy to the gas during each collision. Such collisions can be classified as: (1) elastic collisions in which the kinetic energy is conserved, and (2) inelastic collisions in which some of the kinetic energy is transferred into potential. The energy transferred to the gas may result in excitation and/or ionization. This energy transferred is given by Eq. (2.2), and is determined by the scattering angle. Of course, with either type of collision, both particles' trajectories are altered.

2.4.1 Sputtered Atoms and Reflected Neutrals

As the sputtered atoms and reflected neutrals travel between the target and the substrate regions, they collide with the gas molecules and are scattered. This collision is a random process, which may be described by a Poisson distribution [55,61,142]. The distance between collisions (free path), λ is related to the mean free path, λ_m by [106]:

Reproduced with permission of the copyright owner. Further reproduction prohibited without permission.

$$f(\lambda)d\lambda = \frac{1}{\lambda_m}\exp\left(-\frac{1}{\lambda_m}\right)d\lambda \tag{2.4}$$

Where, λ is distance from one collision to the next and λ_m is the mean free path, which increases with the velocity and energy of the atom. For an elastic collision between a sputtered atom of energy, E_a and a gas atom, the mean free path can be approximately related to the average kinetic energy, $E_g = 3kT/2$ at a gas temperature T and pressure P by [143,144]:

$$\lambda_m = \left(\frac{\gamma B E_g^{1/4}}{6}\right)E_a^{1/4} \tag{2.5}$$

$$B \cong \frac{0.012}{M_g^{1/2}}\left(1+\frac{M_t}{M_g}\right)^{1/2}\left(1+\left(\frac{M_g}{M_t}\right)^{2/3}\right)^{3/4}\frac{T}{P}\ [\mathrm{cm(eV)^{-1/2}}] \tag{2.6}$$

Where k is Boltzmann constant and γ is given in Eq. (2.2). Elastic collisions degrade energy of both the sputtered fluxes and the reflected neutrals on their way to the substrate. A correction factor $\left(1+M_g/M_t\right)^{-1}$ is however applied to B for cases where M_t is less than M_g [56]. After each collision, the ratio of the final energy, E_f to the initial energy, E_{in} before the collision may be expressed as [93,145]:

$$\frac{E_f}{E_{in}} = \exp(-\alpha) \tag{2.7}$$

Reproduced with permission of the copyright owner. Further reproduction prohibited without permission.

Where $\alpha = 1 - \left\{ \frac{(1-M)^2}{2M} \right\} \ln \left\{ \frac{(1+M)}{(1-M)} \right\}$ for $M < 1$

$$\alpha = 1 - \left\{ \frac{(M-1)^2}{2M} \right\} \ln \left\{ \frac{(1+M)}{(M-1)} \right\} \quad \text{for } M > 1 \qquad (2.8)$$

with $M = M_g / M_t$

If the particle travels through a distance, d, then, after d/λ number of collisions, the final average energy of the particle, if it were ejected or reflected with an energy, E_{in}, is

$$E_f = E_{in} \exp\left(-\frac{\alpha d}{\lambda} \right) \qquad (2.9)$$

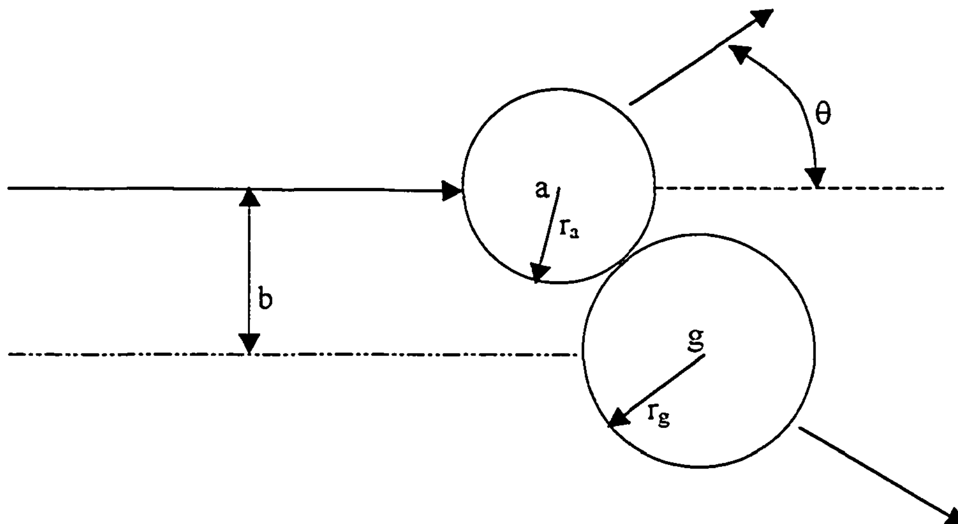

Fig. 2.3 Sketch of collision between different atoms. The gas atom is assumed at rest. The incident atom moves from the left towards the gas atom.

Reproduced with permission of the copyright owner. Further reproduction prohibited without permission.

Changes in gas temperature due to gas heating [59,63,146] affect the free path as expressed in Eq. (2.6) above, and hence the final energies.

Fig. 2.3 shows a diagram of the collision between two atoms (sputtered atom or reflected neutral and gas atom). The gas atom is at rest in this frame, while, the sputtered atom or reflected neutral moves from the left. The impact parameter, *b*, which defines the distance of closest approach, determines the scattering angle, θ. Dependence of the scattering angle on the impact parameter is determined by the type of model used in explaining the collision process. For a binary elastic hard-sphere model, the centre of mass frame scattering angle is given by: [64,147]

$$\theta_{cm} = \pi - 2\arcsin(b/d) \tag{2.10}$$

where $d = r_a + r_g$ is the maximum radius of interaction of the two atoms. As the two bodies approach each other, they are subjected to both forces of attraction and repulsion. If the collision is elastic and the forces act along the line joining the two particles with no transverse forces, the scattering angle may be shown to be related to the potential energy, *V(r)* by [105]:

$$\theta_{cm} = \pi - 2\int_{r_{min}}^{\infty} \left(\frac{b.dr}{r^2\sqrt{1 - \frac{V(r)}{E_c} - \frac{b^2}{r^2}}} \right) \tag{2.11}$$

Reproduced with permission of the copyright owner. Further reproduction prohibited without permission.

where E_c is the centre of mass energy and b is the impact parameter, which defines whether the collision is head-on or merely glancing.

2.4.2 Electrons and Ions

Electrons are emitted at the cathode and are accelerated away into the cathode sheath with energies close to $|eV_d|$, where V_d is the discharge voltage. Usually, the cathode sheath is thin ~0.5 – 1 mm [148,149]. Thus, electrons generally traverse it with negligible collisions with the background gas. The electrons are trapped in the magnetic field and begin to orbit around the field lines. Electrons, however, can escape by undergoing collisions [149,150]. Such electrons are collected by all grounded conductive parts of the device, which constitute the anode of the discharge. In the glow, the energy deposition is enhanced by the magnetic field. Ionization and excitation processes occur within this glow [150]. The excited atom may be de-excited by losing some of its energy to another colliding particle or by emitting electromagnetic radiation.

Electrons may lose energy as a result of elastic and inelastic electron-atom collisions as well as through Coulomb collisions. Losses by electrons through Coulomb collisions are important only in the low energy range [149]. The electron density is proportional to the applied power density [151]. Electron temperature depends on the gas-target

Reproduced with permission of the copyright owner. Further reproduction prohibited without permission.

combination, and correlates inversely with pressure [152]. Since the gas density within the plasma is dependent on gas temperature, it may be assumed that the electron temperature would increase due to gas heating.

2.5 Heat Transfer

Heat transfer from a heated region to the substrate is considered as a possible source of energy flux toward the substrate. It is a complex process, and is usually categorized into three basic types or modes [153–157]. These are conduction, convection and radiation. In the situation under consideration, the transfer of heat involves at least two of these modes. In gases, conduction is by diffusion of atoms or molecules [158]. The phenomenon of heat transfer by convection occurs only in fluids (liquids and gases), by means of particle displacement, and is usually accompanied by conduction [158]. Thermal radiation is a process of propagation of energy in the form of electromagnetic waves.

Non-radiative heat transfer between two bodies depends strongly on the temperature difference between the two bodies and their thermal link. From classical theory, the rate of conductive heat transfer between surfaces is given by the form of Fourier's law, which may be expressed as [159,160].

Reproduced with permission of the copyright owner. Further reproduction prohibited without permission.

$$\frac{q}{A} = \kappa_T' \frac{T_1 - T_2}{x_2 - x_1} \tag{2.12}$$

Eq. (2.12) may be expressed as:

$$\frac{q}{A} = \frac{T_1 - T_2}{r} \tag{2.13}$$

Where q is the rate of heat transfer, A is the area of the cross section, $x_2 - x_1 = \Delta x$ is the separation of the surfaces, $T_1 - T_2 = \Delta T$ is the temperature difference between the surfaces, and κ_T' and r are respectively the effective thermal conductivity and thermal resistance determined by the combined effect of conduction and convection. For heat transfer between a surface and a gas, the thermal conductivity and convection coefficient depend on the gas pressure, especially at pressures below 100 Pa [161]. The heat transported by the gas decreases with pressure reduction. To determine the relative importance of convective heat transfer over the conductive one, the Peclet number is usually used. The Peclet number is defined by [66,162–165]:

$$Pe = c_p \rho v L / \kappa \ , \tag{2.14}$$

Where v is the gas flow velocity, c_p is the specific heat capacity at constant pressure, ρ is the gas density, L is the characteristic diffusion length, and κ is the thermal conductivity of gas. When $Pe < 1$, the conductive heat transfer dominates. For the conditions considered here, the Peclet number is less than 0.02., so clearly the dominant mode is

Reproduced with permission of the copyright owner. Further reproduction prohibited without permission.

conduction. The thermal resistance, r_g for a gas at low pressure ("residual gas") is given by [166]

$$r_g = \left(\frac{\beta - 1}{\beta + 1}\right)\left(\sqrt{\frac{8\pi m T_g}{k}}\right)\frac{1}{PA} \tag{2.15}$$

Where β is the ratio of specific heat at constant pressure to that at constant volume, A is the area of the heating surface, m and T_g are the gas mass and temperature respectively. The accommodation coefficient here is assumed equal to one. For typical conditions considered here r_g is 5000 to 30000 K/W.

Thermal radiation emitted from a surface depends principally on the temperature of the surface. From Stefan-Boltzmann law [167], for a perfect black body, the radiation emitted from the body is given by:

$$\frac{q}{A} = \sigma T^4 \tag{2.16}$$

Generally, not all bodies are perfect emitters, hence the emitted radiation may be given by:

$$\frac{q}{A} = \varepsilon \sigma T^4 \tag{2.17}$$

Where ε and σ are respectively the emissivity of the surface of the body, and Stefan-Boltzmann constant.

Reproduced with permission of the copyright owner. Further reproduction prohibited without permission.

If two bodies are at temperatures T_1 and T_2 respectively, there is an interchange in radiation between the bodies. The net radiation exchange depends on the temperatures and geometry (shape) factors of the bodies [168].

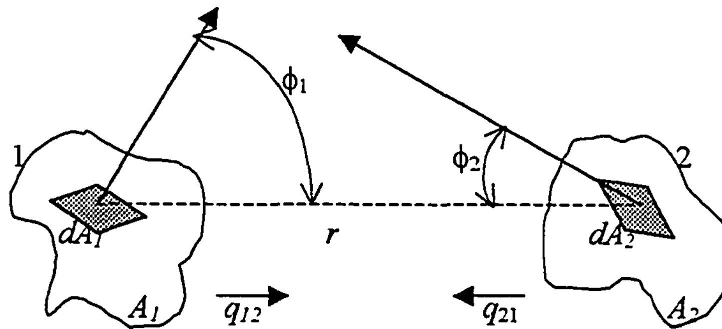

Fig. 2.4 Radiation between two finite bodies separated by a non-absorbing medium

Fig. 2.4 shows a sketch of two typical finite bodies separated by a non-absorbing medium, but between which there is a net interchange of thermal radiation. Body 1 is at a distance, r from body 2. The net radiation between the two gray bodies is given as [153]:

$$q = F_{1-2}\sigma\left(\varepsilon_1 A_1 T_1^4 - \varepsilon_2 A_2 T_2^4\right) \tag{2.18}$$

In the sputter deposition system, the target and the shield around the target may be treated as a small gray body in a gray enclosure [169], if the difference in temperature between the substrate and the chamber walls is small. The gray enclosure behaves as a black body through the opportunities for ultimate absorption offered by repeated reflection from its

Reproduced with permission of the copyright owner. Further reproduction prohibited without permission.

walls [154]. All the emission from the target, q_{12} will ultimately be absorbed by the enclosure. However, only a fraction of the emission from the walls will be absorbed by the target, depending on the view factor, $F_{1\text{-}2}$, of the wall with respect to the target and the emissivity of the target. Bayley, *et al*, [154] showed that the net radiation flux from the heating source to the walls of the enclosure is given by:

$$\frac{q}{A_1} = \varepsilon_1 \sigma \left(T_1^4 - T_2^4 \right) \tag{2.19}$$

2.6 Effect of Gas Phase Collisions: Gas Heating and Rarefaction

The volume in front of a sputtering cathode must be viewed as a dynamic region [170]. Within this volume are the plasma and the energetic species such as the sputtered atoms and reflected neutralized gas atoms. These species can potentially deposit energy into that volume. Other potential sources of energy include the emission from the plasma and thermal radiation from hot bodies. The energetic fluxes are said to be non-uniform. The deposition of energy from those sources into the volume has the effect of raising the temperature of the gas within this volume, which can cause rarefaction of the gas and may affect the properties of the local particles [63]. There has been evidence of a reduction in electron temperature and density as a result of the gas heating [68,70,71].

Reproduced with permission of the copyright owner. Further reproduction prohibited without permission.

In order to estimate the extent of gas heating, sputtered atoms are considered the dominant source of the heating [63], because the mean free path of the sputtered atoms is much less than the mean free path of the reflected neutrals since the average energy of the neutrals is much higher [94]. Doughty *et al*, [126] stated that the symmetric charge exchange is responsible for heating the gas in the cathode fall for an abnormal discharge. However, the energy transferred to the gas through this process is considered small compared to that transferred from the sputtered atoms. The amount of energy transferred from low energy electrons to the gas is limited by the immense difference in the mass of the collisions partners.

If the sputtered atoms are ejected with an average kinetic energy, E_a, then the energy due to these particles can be given as [63]:

$$E_{ip} = IY_s E_a \tag{2.20}$$

Where I is the magnetron discharge current. If the heated region is treated as a sphere with a radius, r, which is much less than the radius of the chamber, R, and since conduction is considered the more important heat transfer mode here (see section 2.4), then the difference in temperature between the heated sphere and the chamber walls is given by:

$$\Delta T = T - T_w \approx \frac{E_{ip}}{4\pi\kappa}\left(\frac{1}{r} - \frac{1}{R}\right) \tag{2.21}$$

Reproduced with permission of the copyright owner. Further reproduction prohibited without permission.

Where κ is the thermal conductivity of the gas and T_w is the temperature of the chamber walls. For argon gas and the sputtering system under consideration (R = 24 cm), and typical process conditions in which the currents are 0.21 and 0.74 A and the corresponding voltages of 350 and 430 V respectively, in which the kinetic energies of the ejected Al particles are respectively 10 and 8.5 eV, a plot of the variation in temperature difference of gas with pressure is shown in Fig. 2.5. The diameter of the heated sphere is taken to be three mean free paths, with the assumption that most of the kinetic energy of the sputtered particle is lost after the first three collisions [63]. The mean free path was determined for a given E_a using Eq. (2.6) in terms of gas temperature, T, and pressure, P, and T_w = 300 K. From Fig. 2.5, it is noted that the gas temperature depends strongly on the kinetic energy of the particles and gas pressure.

Gas heating is sensitive to the sputtering yield, thermal conductivity of gas, average kinetic energy of the sputtered material, and the discharge current as well as the dynamics of the sputtered atoms and the background gas. Rossnagel [63] showed that for a given set of materials, the gas heating depends approximately on the square root of the discharge current.

Reproduced with permission of the copyright owner. Further reproduction prohibited without permission.

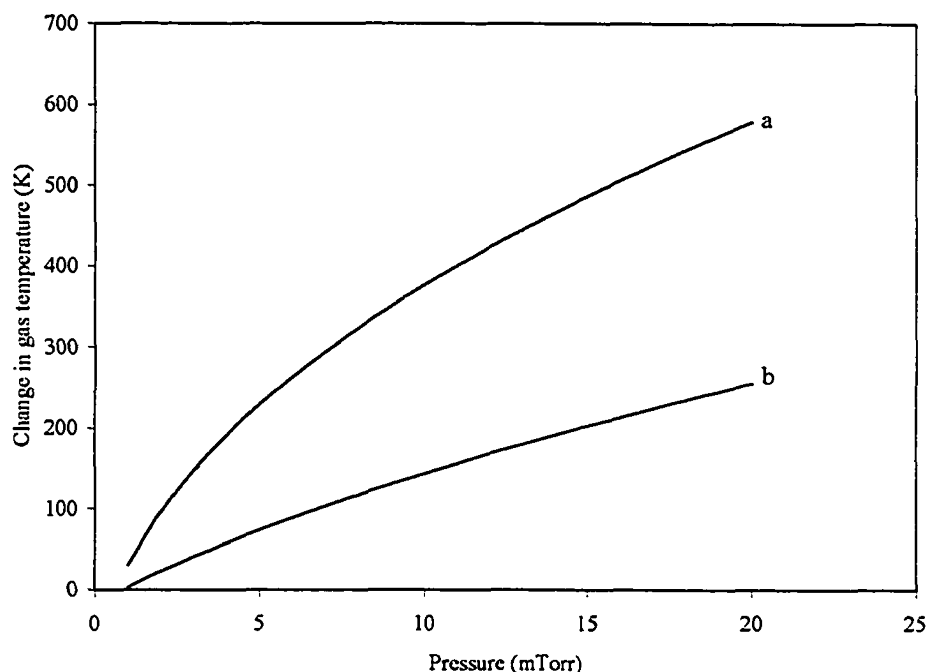

Fig. 2.5 Estimated changes in gas temperature with pressure due to gas heating in a typical sputtering chamber of radius 24 cm, for sputtered Al particles of average energy (a) 10 eV and (b) 8.5 eV which correspond to discharge voltages of 350 V and 430 V, and currents of 0.21 and 0.74 A respectively.

Lighter gas tends to have a reduced effect due to both lower sputtering yield and a higher thermal conductivity [63, 146]. Turner [146], using Ar as the filling gas and C, Al, Ti, Cu, W and Au as sputtered materials, and maintaining current and voltage at 1.0 A and 500 V respectively, calculated the gas heating effect, and showed that C, because of its low value of sputtering yield and its small collision cross section with Ar, would result in negligible heating, whereas significant heating was found for all other elements. It was

Reproduced with permission of the copyright owner. Further reproduction prohibited without permission.

further showed that the heating effect at high pressure (~ 75 mTorr) appears to be primarily determined by the sputtering yield, since at high pressures, the majority of the sputtered atoms are nearly thermalized by a short distance away from the cathode [55, 171,172]. Thus, it may be said that the magnitude of the heating effect is determined by the energy content of the sputtering flux. At low pressure (< 15 mTorr), the degree of gas heating appears to be determined primarily by a combination of collision cross section and the sputtering yield.

As the distance between the target and substrate is increased, high energy sputtered atoms are more likely to have collisions with the filling gas atoms and transfer energy to the filling gas rather than to the substrate or walls of the chamber. This may result in an increase in the maximum temperature of the gas for a given input power. However, in the limit of very high pressures, maximum temperature will become independent of distance, since the power input to the filling gas is localized relatively near the cathode so that the heat flow from the filling gas to the cathode dominates that to the substrate, and the temperature maximum is adjacent to the cathode [146].

Reproduced with permission of the copyright owner. Further reproduction prohibited without permission.

Generally, as a consequence of the increase in temperature, the gas density is reduced locally in this region. However, Urbassek [59] showed that the pressure would still be above average. This implies that the discharge gas does not acquire mechanical equilibrium near the cathode, and the pressure gradient induces a flow along the axis of the target and away from it, which, closes in a large vortical motion. Heat transport is mainly by conduction as a result of the strong steady state temperature gradient, while the convective energy transfer is negligible. The range of the sputtered particles is increased, since the sputtered particles stopping is decreased due to the gas density reduction. The substrate is therefore bombarded with higher energy fluxes.

2.7 Scaling of Particle Flux and Kinetic Energy with Pressure and Distance

Apart from the initial distributions of the sputtered particle flux and energy, the deposited flux and energy depends on the number of collisions (a factor of the pressure-distance product) suffered by the particles. In this section, we shall use the SIMSPUD [173] program to show how they scale with pressure and distance. SIMSPUD is a three-dimensional Monte Carlo vapour transport model. It provides information about sputter distribution characteristics, such as the kinetic energy and deposition efficiency, at the substrate. It uses the Thompson distribution model in determining the energy and angular distribution of the sputtered atoms. Using SIMSPUD, Fig. 2.6 shows the dependence of

Reproduced with permission of the copyright owner. Further reproduction prohibited without permission.

the kinetic energy of sputtered aluminum atoms upon the pressure distance-product. It clearly shows that most of the atoms are thermalized at about 200 mTorr-cm. The solid line is an empirical fit to an exponential function, and is expressed by:

$$\frac{E_f}{E_i} = \exp(-0.12Pd) \tag{2.22}$$

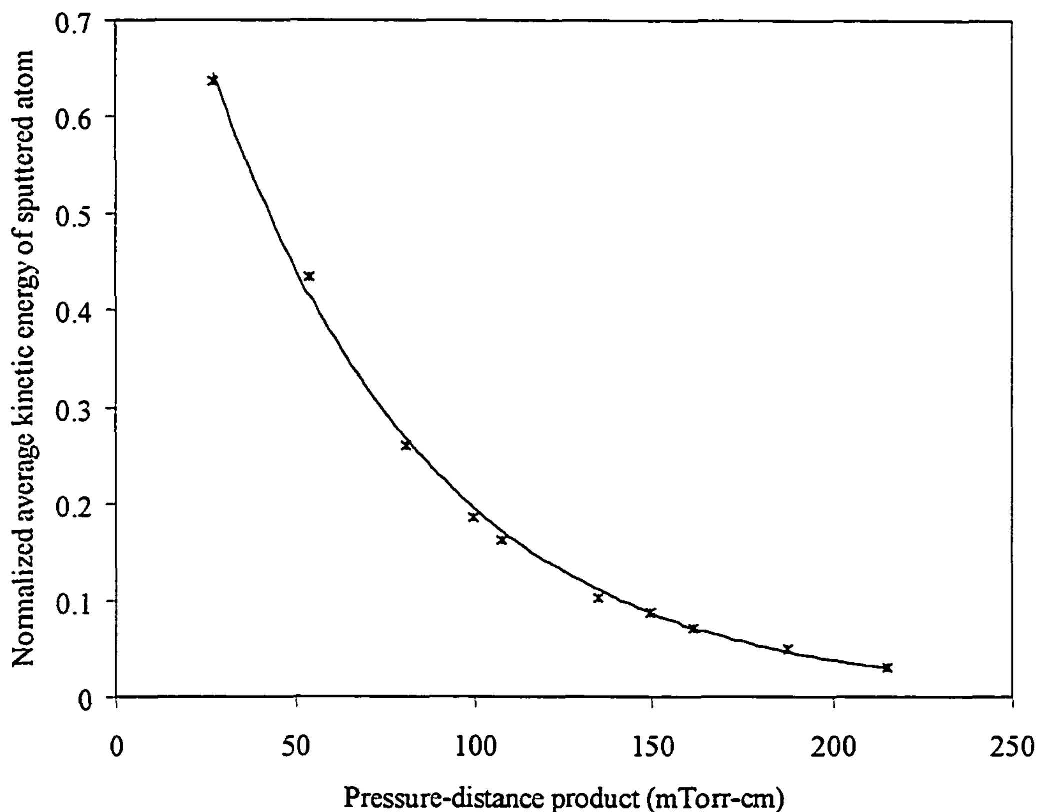

Fig. 2.6 Average final kinetic energy of sputtered atoms as a function of pressure-distance product, obtained using SIMSPUD. The solid line is an exponential fit to the data points.

Reproduced with permission of the copyright owner. Further reproduction prohibited without permission.

The initial sharp fall in the energy curve indicates the significant amount of energy deposited into the gas within a few mTorr-cm of the target due to scattering events with the background gas atoms. This contributes to gas heating observed within the plasma region [63], with a resulting gas rarefaction. For instance, Rossnagel [63] obtained for a gas / target system with high sputter yield and relatively heavy gas atoms, about 85 % reduction in gas density at 50 W/cm^2. However, SIMSPUD does not include a rarefaction model, hence, it is expected that it might overestimate the scattering events. The implication is that the onset of thermalization process might be extended further.

Scattering events complicate the distributions of the sputtered atoms as they move toward the substrate. To account for this, SIMSPUD uses a hard sphere model to determine the scattering events. The use of a binary elastic hard sphere model over-estimates the scattering events, but simplifies the calculations. Scattering events depend strongly on the collision cross-section of the colliding particles. This cross section has been shown to be energy dependent [98]. For sputtered particles of energies in the range of 1 – 200 eV, SIMSPUD uses an empirical fit of this dependence of the form [174]:

$$\sigma(E) = \sigma(E_0)\left(\frac{E}{E_0}\right)^{-0.29}, E > E_0 \quad (2.23)$$

Where $E_0 = 1$ eV.

Reproduced with permission of the copyright owner. Further reproduction prohibited without permission.

The normalized values of the deposition efficiency, η (ratio of flux deposited at the substrate to flux ejected at the target) are determined for different gas pressures and plotted in Fig. 2.7 along with an empirical fit to an exponential function of the form [127]

$$\eta = \exp(-\beta P) \tag{2.24}$$

At high pressures, only a small fraction of the ejected atoms at the target reach the substrate, as indicated by the low deposition efficiency.

Apart from scattering, geometrical factors and the nature of the ejection of the particles, even for normal ion incidence, affect the deposition efficiency. This is demonstrated in Fig. 2.8, in which the simulated gas pressure was set at zero, and the deposition efficiency estimated with distance. The solid line is an empirical fit to the simulation results using an exponential function, and expresses the particle flux, ϕ with distance [175]:

$$\phi_d = \phi_0 \exp(-cd) \tag{2.25}$$

where ϕ_0 is the emitted flux determined by the product of current density and the sputtering yield, c is a constant determined by the angular distribution of the emitted particles at the target. This clearly demonstrates that, given the cosine emission pattern of the emitted flux, even without scattering due to collision with the gas, the deposition efficiency depends on distance from the target. This is contrary to what is used elsewhere [24,176–178].

Reproduced with permission of the copyright owner. Further reproduction prohibited without permission.

These scaling laws will be used in obtaining the deposition and energy models in Chapter 5.

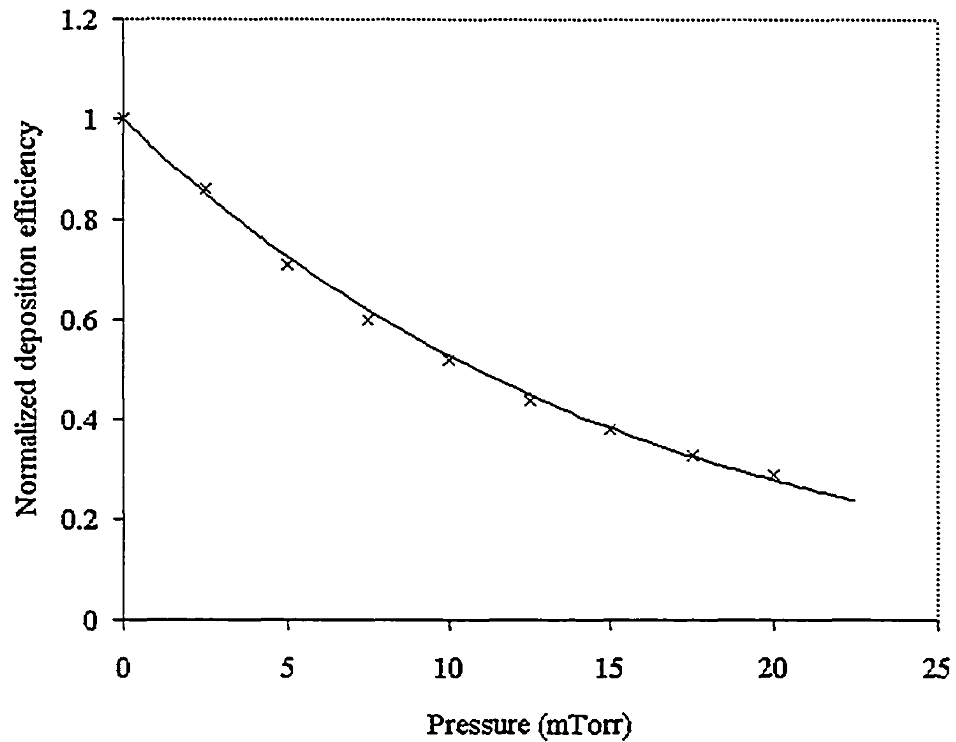

Fig. 2.7 Simulated deposition efficiency (normalized to zero pressure). The solid line reflects a fit to an exponential function.

Reproduced with permission of the copyright owner. Further reproduction prohibited without permission.

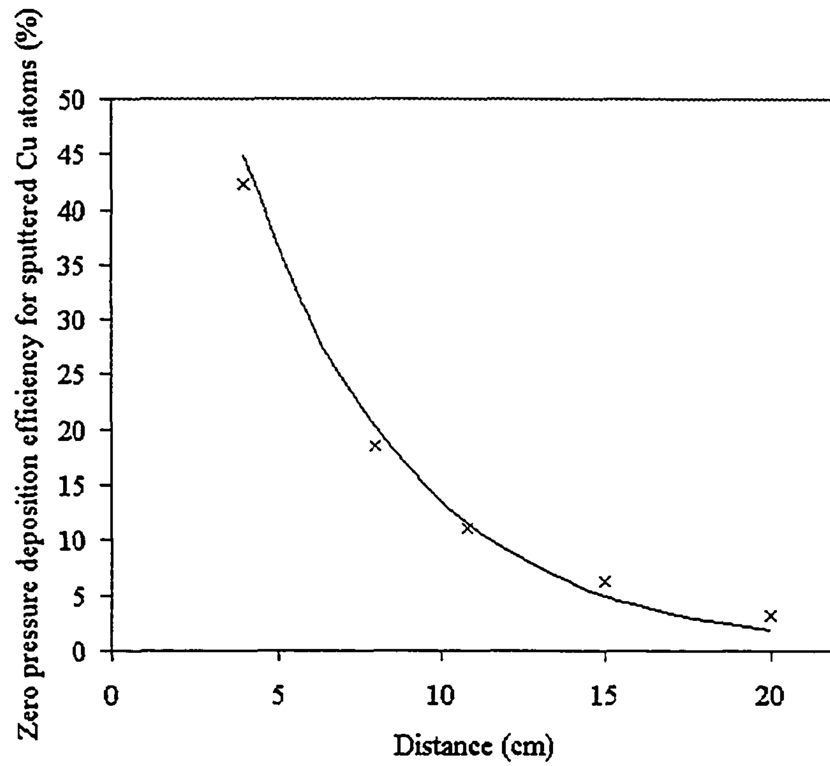

Fig. 2.8 Dependence of deposition efficiency on substrate-target distance. The data points were obtained using SIMSPUD. The solid line is a fit to the simulated data.

Reproduced with permission of the copyright owner. Further reproduction prohibited without permission.

Chapter 3

Calorimeter and Experimental Design

3.1 Calorimeter

This work is concerned with the measurement of heat flows in a sputter deposition system. One useful technique to accomplish this is through calorimetry [179]. In a calorimeter, energy added translates directly into a temperature increase, which can be more easily measured. A calorimeter consists of an absorber to contain the deposited energy, a sensor to measure the temperature of the absorber, and a weak thermal link to a heat sink to return the absorber temperature to some equilibrium value following an event [180]. If an event deposits energy on the calorimeter, the rise in temperature would be given as the ratio of the deposited energy to the thermal capacity of the calorimeter. Following the event, the increase in temperature will decay toward zero with a time constant equal to the ratio of the thermal capacity to the thermal conductance of the thermal link. Thus, in designing a calorimeter, the basic factors of interest are the temperature sensitivity of the sensor, the thermal capacity of the absorber and the thermal

Reproduced with permission of the copyright owner. Further reproduction prohibited without permission.

conductance of the interface between the sensor and the absorber. High sensitivity is obtained for very low capacity and/ or conductance.

Silicon has excellent thermal and mechanical properties for use in the design and construction of calorimeters [180–182]. Silicon thermistors appear to be nearly ideally suited as thermometers for high-resolution micro-calorimeters [183]. They can readily be integrated into a monolithic silicon detector structure using standard integrated circuit techniques, and the size can be easily made sufficiently small such that it makes a negligible contribution to the total heat capacity.

3.2 Energy Flux Measurement

When a material absorbs heat energy, its temperature rises. The change in the temperature is directly proportional to the change in the internal energy (heat absorbed) of the material. The heat absorbed, ΔQ is expressed as:

$$\Delta Q = mc\Delta T \tag{3.1}$$

Where m and c are respectively the mass and specific heat capacity of the material, and ΔT is the change in temperature. The mc product defines the thermal capacity, C_T of the material. Thus, the energy absorbed may be inferred from the knowledge of the change in temperature. Physical and optical properties of the material, such as size, resistance,

Reproduced with permission of the copyright owner. Further reproduction prohibited without permission.

absorption, refractive index, [180,181,184–189] may be affected due to the heat absorbed by the body. The temperature dependence of these properties is of great importance in the design of calorimeters for heat /or temperature measurement.

Temperature is one of the key parameters in ultra-large scale integration manufacturing. Accurate knowledge of the temperature and its control is required to ensure the desired film growth rates and film qualities during the film processing [190,191]. It is well known that surface mobility and reaction rates are greatly influenced by temperature of the substrates [190,192,193].

Many techniques for determining temperature have been developed over the years. Some require physical contact between the measuring device and the specimen, and others require non-contact methods such as radiometry and luminescence. Thermocouples or thermistors have been widely used for the contact method. The major advantage of this is their ability to make low temperature measurements (< 700 K) using a simple setup. Unfortunately they require mechanical contact with the specimen. In many cases this contact is not ideal and leads to the formation of a temperature gradient between the specimen and the thermocouple [186,194]. The temperature jump that exists between the surface of a wall and the surrounding gas, especially at low pressures, [68,161] may also be a problem in using such discrete devices. Radiometric methods measure the radiation

Reproduced with permission of the copyright owner. Further reproduction prohibited without permission.

emitted from a heated body. In some radiometers, the total emission, $I = \varepsilon\sigma T^4$ is measured, in others, the emission is in limited spectral ranges [195]. In both cases, the radiation from the target is determined by its temperature and emissivity. This method is applicable mostly at higher temperatures (> 900 K) and requires corrections for the emissivity [196] and other factors.

A solution would therefore be the use of the temperature dependent resistance of homogeneously heated thin films or embedded sensors. The main advantage of this technique is that the sensing element is buried inside the absorber, and hence does not require attachment of the thermal sensor to the specimen. The approach taken in this work is to use a polysilicon thin film thermistor fabricated using a modified complementary metal-oxide semiconductor (CMOS) process. A thin silicon dioxide layer covers this to act as an absorber and to prevent electrical shorting when depositing metal films. The only problem with this may be due to the self-heating effect [183,197] by the sensing current. This problem can be minimized by applying a low bias voltage [176] across the terminals of the thermometer, and by the use of a high resistance thermometer.

The measurement of the increase of the substrate temperature has been a well-established method for the determination of the integral thermal flux to the substrate [129,130,151,198,199]. Another method for the determination of the thermal flux at the

Reproduced with permission of the copyright owner. Further reproduction prohibited without permission.

substrate is the steady state determination of the temperature gradient along the sample holder [134,135,200]. This method does not account for the front-side heat fluxes due to, for example, radiation or gas transport.

While the material body gains heat from the heat source, it also loses some of the heat to the surroundings through conduction, convection and/or radiation. If the rate of heat transferred to the body is q_{tr} and the rate of heat lost from the body is q_l, then the heat balance equation is of the form:

$$q_{tr} = mc\frac{dT}{dt} + q_l \tag{3.2}$$

Where t is the time taken. The rate of heat loss depends on the temperature difference between the body and the surroundings. At steady state, the rate of heat transferred to the body is equal to the rate of heat lost from the body, hence,

$$q_{tr} = q_l \tag{3.3}$$

If the difference in temperature is not very large, heat lost by radiation may be negligible, therefore, the rate of heat lost may be said to be a linear dependence with the temperature difference. This may be expressed as:

$$q_l = \frac{T - T_a}{r} \tag{3.4}$$

T_a is the ambient temperature and r is the thermal resistance. By measuring the temperature, T of the body or the temperature difference at steady state, the heat flux to

Reproduced with permission of the copyright owner. Further reproduction prohibited without permission.

the body can be estimated, provided that the thermal resistance is known. However, r can be estimated from a transient response of the sensor during heating and cooling as will be demonstrated in section 3.4.2 below.

3.3 Micromachined Temperature Probe

As stated earlier, silicon is well suited for use in the construction of a calorimeter because of its excellent properties. It lends itself to the fabrication of large arrays, and standard CMOS processing can be used in fabricating the calorimeter. As a thermal probe, it can be used as a sensing or a heating device [201]. Its temperature dependent resistance property is used here in the design of the calorimeter.

The temperature dependent resistance of a material is commonly given by the power series:

$$R(T) = R_0[1 + \alpha(T - T_0) + \beta(T - T_0)^2 + \gamma(T - T_0)^3 + \cdots \quad (3.5)$$

Where R_0 is the resistance of the material at a reference temperature, $T = T_0$, and α, β and γ are material related constants. For the polysilicon used here, and for the temperature changes in this work (see section 3.4.1), it is sufficient to truncate the power series as

$$R(T) = R_0[1 + \alpha(T - T_0)] \quad (3.6)$$

Reproduced with permission of the copyright owner. Further reproduction prohibited without permission.

Fig. 3.1 shows the layout of the first iteration (sensor 1) of the micro-senor/absorber. It was fabricated using 1.5μm CMOS process courtesy of the Canadian Microelectronics Corporation. A layer of serpentine-shaped polysilicon is embedded in a silicon dioxide platform. The polysilicon is used as the sensing element, while the silicon dioxide (SiO_2) serves as the absorber. The width of the polysilicon is 5μm and its total length is about 940μm for a room temperature resistance of 1500 Ω and temperature coefficient of resistance, $\alpha = 1.097 \times 10^{-3}$ /°C. Thirty-six of these are connected in an addressable 6 × 6 mesh network to give six terminals at either end. The advantages of this network connection are the reduced effective resistance (reduced self-heating) and reliability in case of any defects in a particular resistor(s). The chip is mounted on a 24-pin DIP ceramic package. For this application, the six terminals at each end are connected together to utilize all 36 units in parallel. All electrical conducting leads/terminals are covered by a small amount of varnish for electrical insulation.

A second design (sensor 2) was also tested, and is shown in Fig. 3.2. Sensor 2 consists of 12 cells. Each cell has two micro resistors (concentric heaters) to allow radial heat flow to be zeroed. In order to increase the sensitivity of the sensor, it was suspended on a diaphragm. This reduces the thermal capacity of the material around the polysilicon, and thermally isolates it from the silicon substrate.

Reproduced with permission of the copyright owner. Further reproduction prohibited without permission.

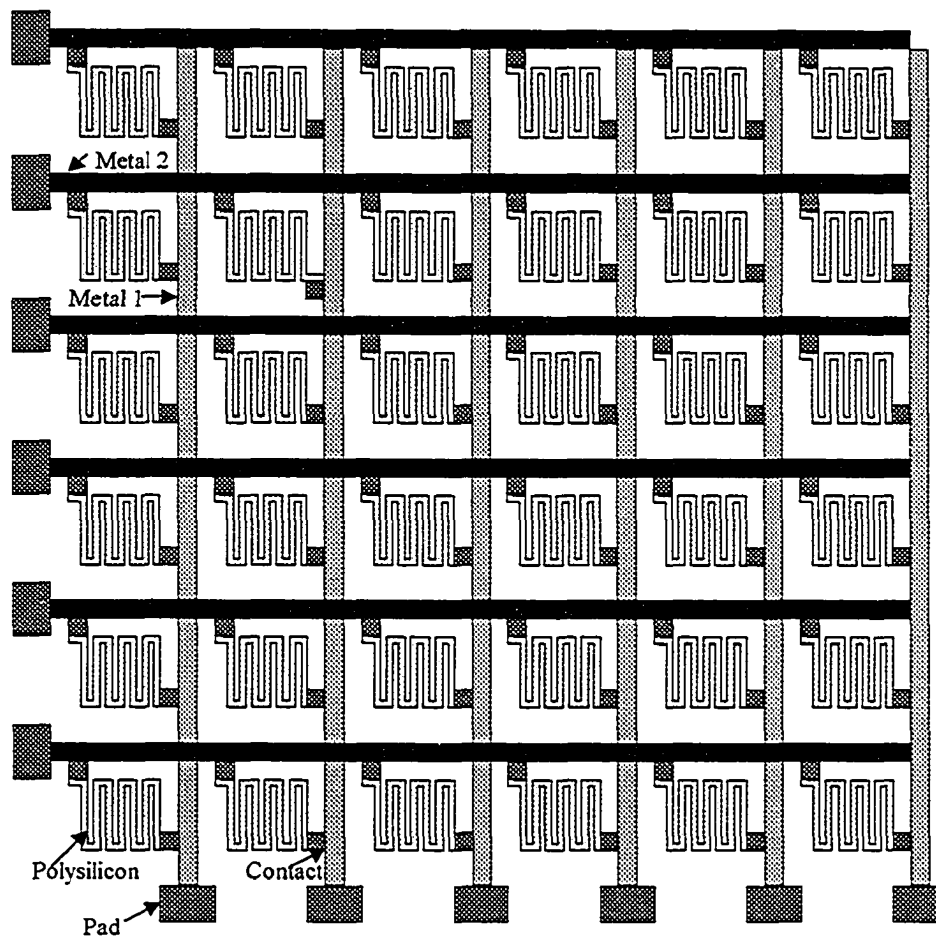

Fig. 3.1 CMOS temperature probe layout showing 36 polysilicon resistors connected in an addressable 6 x 6 mesh network.

Reproduced with permission of the copyright owner. Further reproduction prohibited without permission.

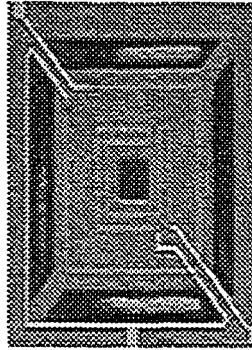

Fig. 3.2. Photograph of one of the cells of sensor 2 showing the arrangement of the sensing elements and the etched silicon underneath the SiO_2 covered polysilicon (The design was done by Keith Brown).

The transient thermal response of the probe can be modelled by the differential equation:

$$C_T \frac{dT}{dt} = q_{in} - \frac{(T - T_a)}{r} - q_w \tag{3.7}$$

where, C_T is the thermal capacity of the absorber, q_{in} is the power input to the probe, and q_w is the power lost due to non-linear processes such as radiation. T is the temperature of the sensor, T_a is the temperature of the heat sink, and r is the thermal resistance to heat flowing between T and T_a. For the temperature differences involved here, q_w tends to be small compared with the other terms. Thus:

$$\frac{dT}{dt} = \frac{q_{in}}{C_T} - \frac{(T - T_a)}{rC_T} \tag{3.8}$$

Reproduced with permission of the copyright owner. Further reproduction prohibited without permission.

3.4 Characterization and Calibration of the Sensor

The following treats the determination of the temperature coefficient of resistance, thermal resistance and thermal capacity of the sensors.

3.4.1 Temperature Coefficient

The temperature coefficient of resistance for the probe was determined by measuring the changes in resistance of the probe with temperature. The probe was hung inside a programmable 1 cubic foot Omegalux (LMF 6525) resistive oven. The maximum temperature was programmed to 150 °C to prevent the oxidation of the wires, which may occur at higher temperatures. The resistance of the sensor was measured with an ohmmeter. A J-type thermocouple, which was placed close to the sensor at a distance of less than 1 cm, was used in measuring the temperature. Fig. 3.3 shows the plot of the resistance of both sensor designs against temperature. The solid line is a fit of Eq. (3.10) to the experimental data. A change in temperature of ΔT corresponds to a change in resistance, ΔR. If the resistance of the sensor at $T_0 = 0$ is R_0, then the resistance at $T = \Delta T$ is:

$$R = R_0 + \Delta R \tag{3.9}$$

Reproduced with permission of the copyright owner. Further reproduction prohibited without permission.

Eq. (3.5) expresses the dependence of the probe resistance on temperature. If it is truncated to the third power, the change in resistance of the probe with temperature is:

$$\frac{\Delta R}{\Delta T} = R_0\left(\alpha + 2\beta T + 3\gamma T^2\right) \tag{3.10}$$

From the theoretical fit to the experimental data, the values of α, β and γ were calculated as 9.34×10^{-4}/°C, 7.67×10^{-7}/°C^2 and 7.97×10^{-12}/°C^3 for sensor 1 and 1.30×10^{-3}/°C, 1.67×10^{-7}/°C^2 and 6.13×10^{-12}/°C^3 for sensor 2, respectively. For the temperatures considered in this study and given the very low values of β and γ, the second and higher power series of Eq. (3.5) can be neglected, such that the dependence of the sensor resistance can be expressed in the form of Eq. (3.6), which will simplify analysis. Thus, for modest temperatures, the resistance of the polysilicon used in fabricating the sensor can be said to have a linear dependence on temperature. The change in temperature of a material depends upon the input energy according to Eq. (3.1), thus, the resistance of the sensor would have a linear dependence on the applied power (see Fig. 3.6).

Reproduced with permission of the copyright owner. Further reproduction prohibited without permission.

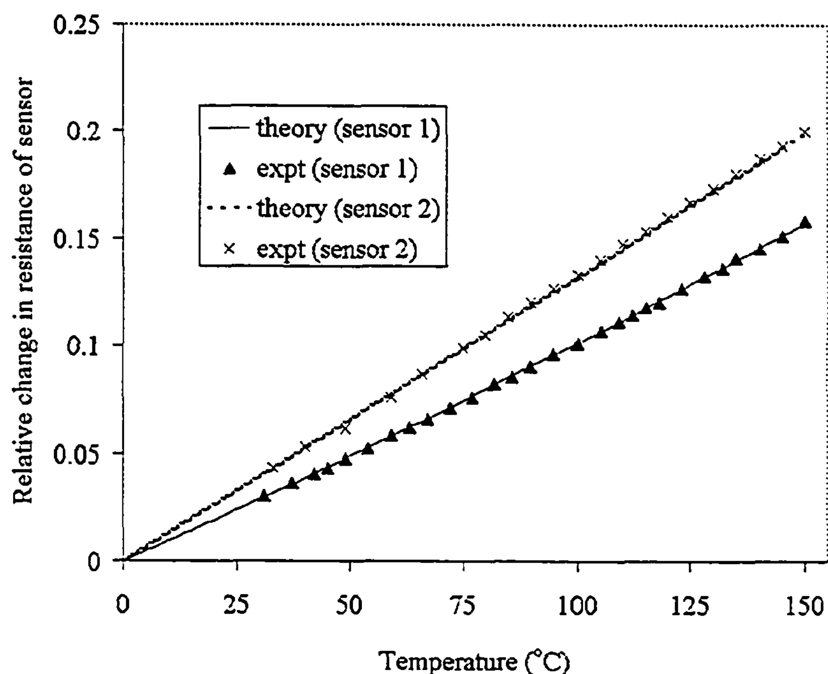

Fig. 3.3. Dependence of the resistance of sensor on temperature. The solid line and dashes are the theoretical fit to the experimental data for sensors 1 and 2 respectively.

3.4.2 Heating Mode: Dynamic Response

As stated before, the probe can be used as a heater and a sensor. When used as a heater, the discharge is turned off, and the source of heat in this mode is localized to the die area. A constant voltage was maintained across the terminals of the polysilicon resistor, and current was measured over time at an argon pressure representative of the experimental

Reproduced with permission of the copyright owner. Further reproduction prohibited without permission.

conditions. The resistance as a function of time was determined from the current – voltage values. The dynamic response of sensor 1 at different voltages and at a gas pressure of 7.5 mTorr is shown in Fig. 3.4. Eq. (3.8) describes how the temperature of the probe varies with time when an input power is applied. The applied power in this case is the joule heat, which is given by:

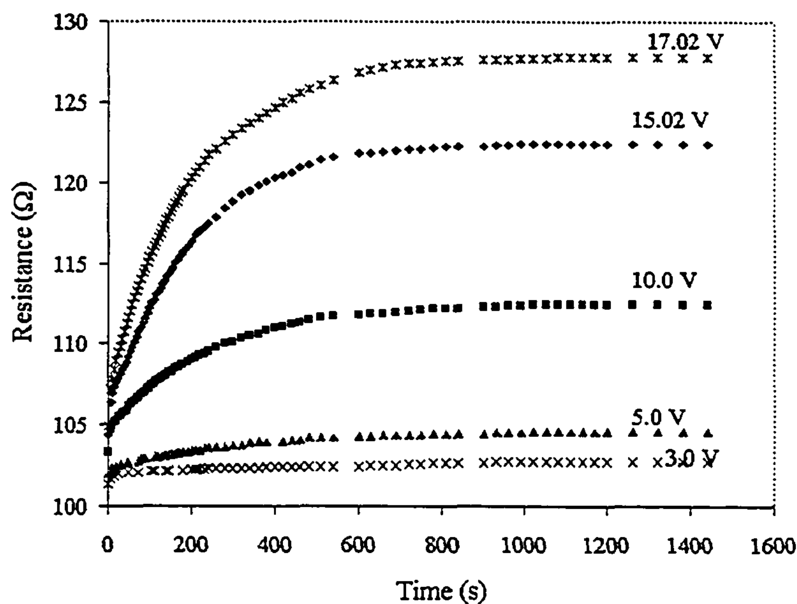

Fig. 3.4 Response of sensor 1 to different applied voltages at a gas pressure of 7.5 mTorr. The indicated different values of the initial resistance were due to the variation in the starting temperatures for each run, and also because more than one sensor was used for all the sets.

Reproduced with permission of the copyright owner. Further reproduction prohibited without permission.

$$q_{in} = \frac{V^2}{R(T)} \tag{3.11}$$

Where V is the voltage maintained across the resistor's terminals. The change in temperature with time may be expressed in terms of the change in resistance with time as:

$$\frac{dT}{dt} = \frac{dT}{dR}\frac{dR}{dt} \tag{3.12}$$

From Eq. (3.6),

$$\frac{dT}{dR} = \frac{1}{\alpha R_0}, \tag{3.13}$$

thus, $$\frac{dR}{dt} = \frac{\alpha R_0 V^2}{C_T R} - \frac{(R - R_0)}{r C_T} \tag{3.14}$$

The dynamic responses of sensor 1 at 12 volts and sensor 2 at 14.6 V, both at a gas pressure of 5 mTorr are shown in Fig. 3.5 (a) and (b) respectively. The power supply was switched off at $t = 740$ s, and 1620 s for sensors 1 and 2. Also shown on this graph are the theoretical fits (solid line and dashes) to Eq. (3.14), which describes the dynamics of the system well. From this fit, the effective thermal capacity and thermal resistance were estimated as 2.2 J/K and 121.5 K/W for sensor 1 and 4 J/K and 94 K/W for sensor 2 respectively. Sensor 2 has two distinct time constants of 2.5 and 376 s. This is due to the etching of the silicon underneath the polysilicon. As can be seen from Fig 3.5, the sensitivity of sensor 2 is doubled as a result of the reduction in the thermal mass of the absorber. However, the overall time constant is increased from about 267 to 376 s.

Reproduced with permission of the copyright owner. Further reproduction prohibited without permission.

To study the effect of applied power on the sensor, different voltages were applied and the corresponding steady state resistances determined. The initial resistance of different sensors may not be the same, thus, it was appropriate to calibrate the sensor in terms of the relative change in resistance, ΔR_{rel}. Where,

$$\Delta R_{rel} = \frac{R - R_0}{R_0} \tag{3.15}$$

It is noted from Fig. 3.6 that the relative change in resistance has a linear dependence on input power at low power levels, with an overall sensitivity of about 139 K/W. However, at powers higher than 1.95 W, the dependence is no longer linear. Further increase in power beyond this results in a sudden increase in temperature, oscillation, and subsequent breakdown of the sensing element. This places an upper limit in temperature change on the calibration of about 250 K. This limit is entirely adequate for the measurements presented in Chapter 4.

Reproduced with permission of the copyright owner. Further reproduction prohibited without permission.

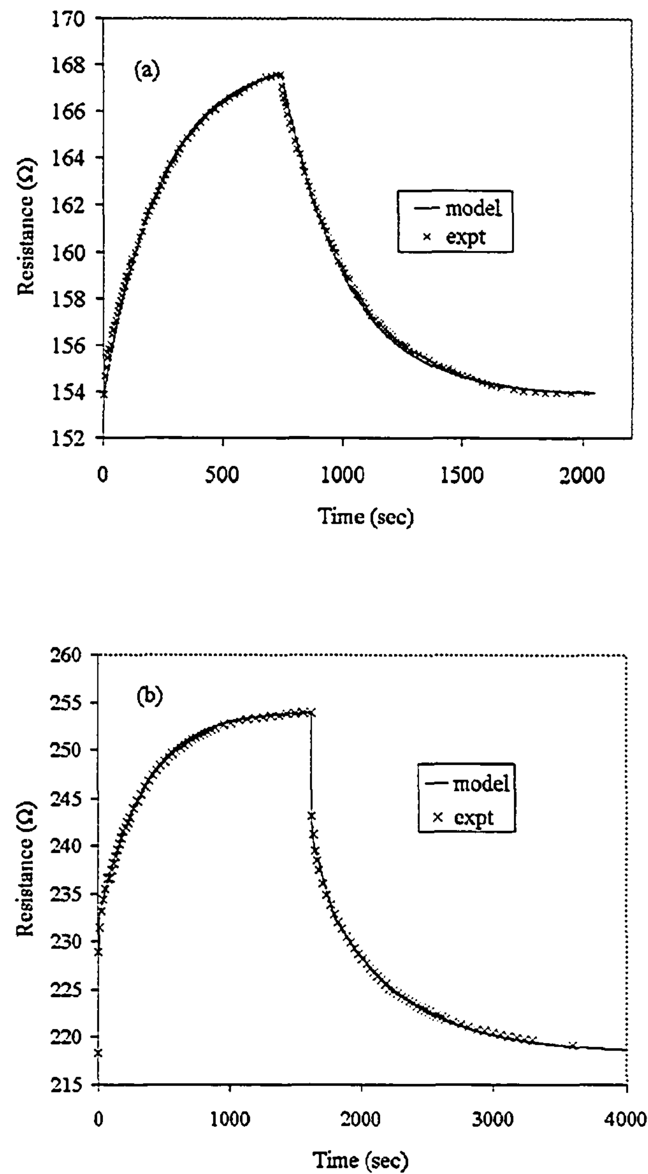

Fig. 3.5 Changes in sensor resistance with time during heating and cooling of (a) sensor 1 and (b) sensor 2. A constant voltage of 12 and 14.8 V was applied to the terminals of sensor 1 and 2, and switched off after 740 and 1620 seconds respectively.

Reproduced with permission of the copyright owner. Further reproduction prohibited without permission.

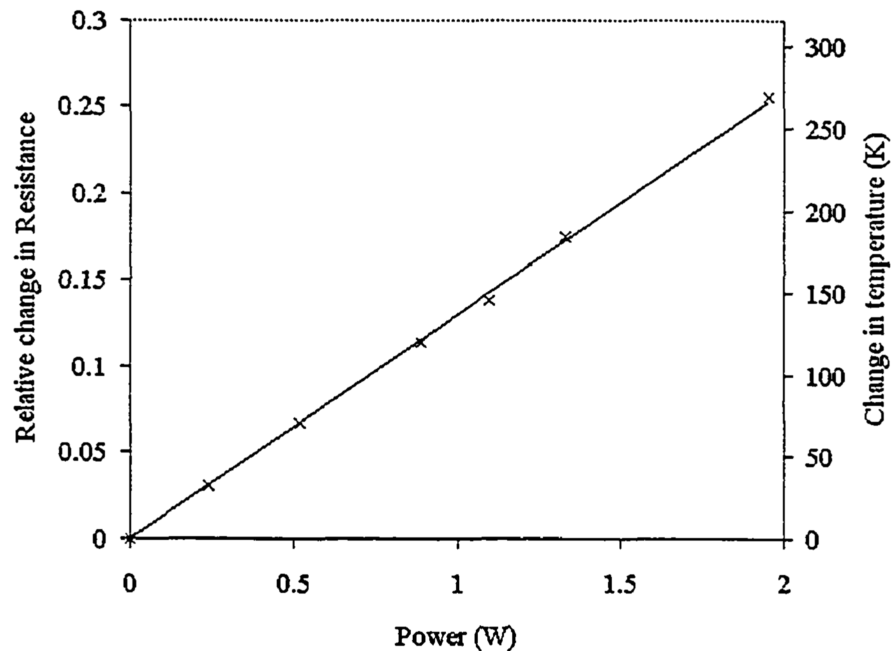

Fig. 3.6 Dependence of sensor 1 resistance and temperature on applied power. The experimental data points of the relative change in resistance are represented by (x), while the solid line is a linear trend of the experimental data. The change in temperature axis compares the estimated change in temperature of the sensor with the relative change in resistance.

The heat exchange between the heating element of the sensor and its surroundings takes place by thermal conduction through the physical elements of the sensor, package and the substrate holder, as well as by thermal conduction and convection through the gas, and by radiation. Of course, the gas transport component of this depends on the gas pressure.

Reproduced with permission of the copyright owner. Further reproduction prohibited without permission.

The effect of pressure on the dynamic response of the sensor 1 is shown in Fig. 3.7. At low pressures, the effect is negligible. However, at high pressures, the effect becomes more significant. This is as expected, since heat conduction and convection by the gas depend strongly upon gas pressure. The effect of pressure on the thermal resistance of the link is shown in Fig. 3.8. In this instance, the sensor terminals and all electrical conducting leads (except the active area) were covered with epoxy. The results show that for pressures between 1 and 10 mTorr, an increase in pressure only caused a slight decrease in the thermal resistance. At pressures above 10 mTorr, however, an increase in pressure results in more significant decrease in the thermal resistance. In this regime, heat transport through gas conduction becomes significant. However, it should be noted that for these pressures, the gas flow rates were also increased so as to attain the required pressures. For our present study, pressures have been limited to more typical pressures of 5 – 10 mTorr, so it is reasonable to assume a constant value for the thermal resistance.

Reproduced with permission of the copyright owner. Further reproduction prohibited without permission.

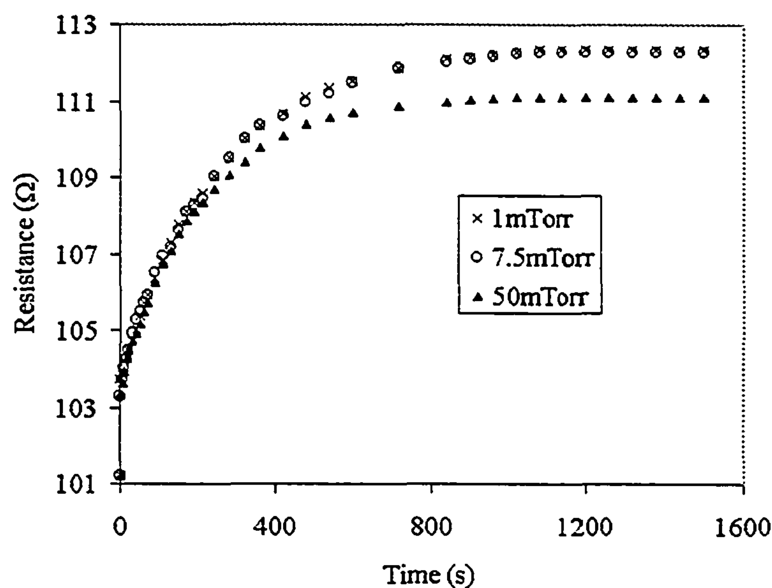

Fig. 3.7 Variation in sensor 1 resistance with time as a function of gas pressure during heating at a constant voltage of 10V.

3.4.3 Sensing Mode

In order to measure heat fluxes during deposition, the internal heater is not powered (beyond the minimal current needed to measure its resistance), and the thermal power transferred to the probe is given by Eq. (3.2). In terms of the electrical resistance, R of the sensing element, this may be expressed as:

Reproduced with permission of the copyright owner. Further reproduction prohibited without permission.

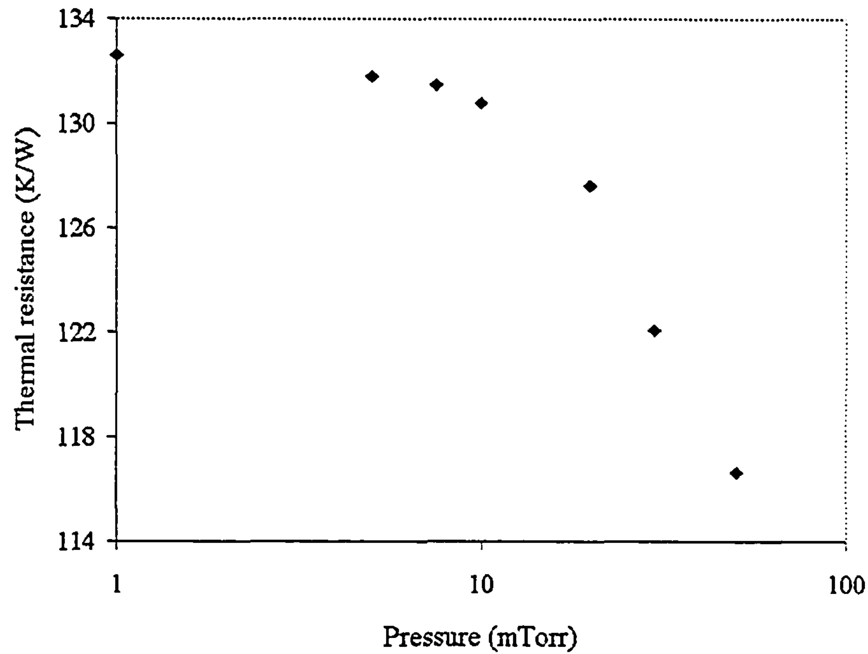

Fig. 3.8 Effect of pressure on the thermal resistance of the sensor/package (electrical terminals and contacts were covered with epoxy).

$$q_{tr} = \frac{C_T dR}{\alpha R_0 dt} + q_L \quad (3.16)$$

As stated earlier, the thermal power is lost through the thermal link and through radiation from the surface of the sensor. If the power lost through radiation is assumed small compared to that through the thermal link then the thermal power lost may be expressed by Eq. (3.4).

Reproduced with permission of the copyright owner. Further reproduction prohibited without permission.

The thermal resistance, r, may vary slightly during sputter deposition from the calibrated value due to gas heating and rarefaction. The thermal capacity, C_T can change significantly because the heating is no longer localized and the thermal capacity of more of the thermal pathway must be included, as it too is heated. The corresponding adjustments to the calibration were determined by examining the transient response immediately after switching off the plasma. The cooling behaviour is then described by

$$0 = \frac{C_T}{\alpha R_0}\frac{dR}{dt} + \frac{R - R_{RT}}{\alpha R_0 r_1} \qquad (3.17)$$

Hence

$$\frac{dR}{dt} = -\frac{(R - R_{RT})}{r_1 C_{T1}} \qquad (3.18)$$

Fig. 3.9 shows the experimental plot and the numerical fit (solid line) to the data points. From the numerical fit, the thermal resistance (r_1) and the thermal capacity (C_{T1}) were determined as 120 K/W and 3.8 J/K respectively. The higher thermal capacity here than in the case of the heating mode clearly shows the effect of the 24 DIP package in the absorption of heat as well as the direction of heat flow to the sensor, especially at steady state. Given Eq. (3.8), the first order substrate temperature response may be determined as [151, 202]:

$$T_s(t) = T_a + r_1 q_{in}(1 - \exp(-t / r_1 C_{T1})) \qquad (3.19)$$

Reproduced with permission of the copyright owner. Further reproduction prohibited without permission.

Hence, the thermal power density, q_{in} as a function of time can be estimated from Eq. (3.19) by measuring the temperature dependent resistance of the sensor

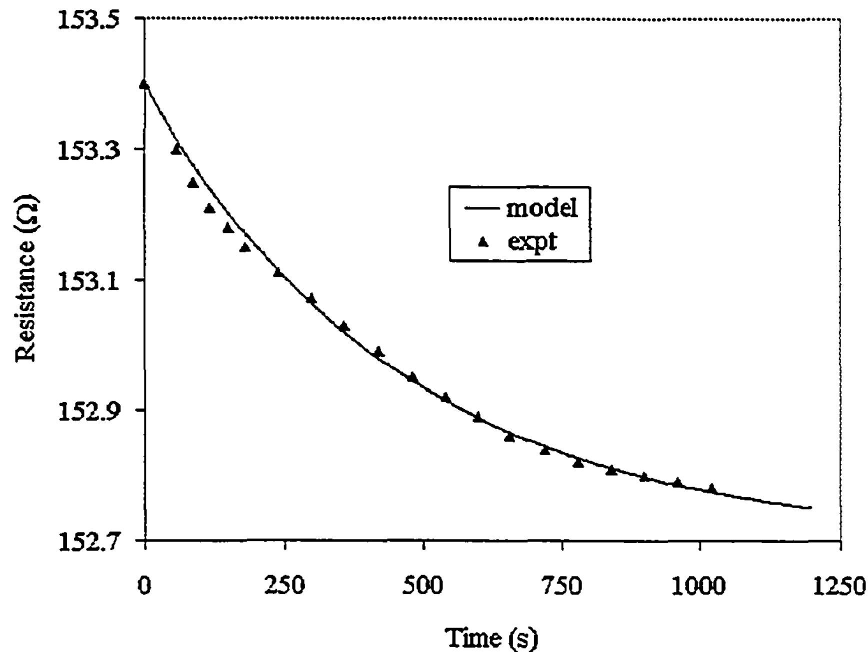

Fig. 3.9 Change in sensor 1 resistance with time after the plasma is switched off at a gas pressure of 5 mTorr and magnetron power of 200 W (substrate-target distance of 21 cm, plasma was previously switched on for 11 minutes to allow for near steady state conditions). The solid line is a numerical fit to the data points.

Reproduced with permission of the copyright owner. Further reproduction prohibited without permission.

3.5 Experimental design

As a test system, a Kurt J. Lesker sputter deposition system with two water-cooled planar 3-in. magnetron sources mounted in the chamber was used. Only one target was used at a time. Al and Cu target materials of purity 99.999% each were employed for the study. Gas flow rate was generally maintained at 9.8 sccm. The discharge was operated at constant power mode, with the voltages in the range 300 – 520 V. The deposition times were between 20 and 25 minutes to allow for steady state to be attained. The temperature sensor [127] located in the substrate region was used to measure the deposited energy at the substrate. A Langmuir probe [128] was also used to characterize the plasma near the substrate.

The experimental setup is based on the arrangement shown in Fig. 3.10, and the main dimensions are as follows: D_C = 49 cm; W_T = 8.5 cm; W_S = 4.5 cm; H_H = 20 cm; D_H = 1.2 cm; H_S = 10 cm; S_1 = 21 cm; S_2 = 10.8 cm. The target surface area was 45.6 cm^2. The target material was clamped to a water-cooled copper plate of the target, and the steel ground shield was fixed to the target by means of three screw bolts. The sensor was mounted on a 24-pin DIP ceramic package (see Fig. 3.11) and attached to the substrate holder plate directly above the target in use. The terminals of the sensing element were connected to a digital multi-meter used in measuring the sensor resistance.

Reproduced with permission of the copyright owner. Further reproduction prohibited without permission.

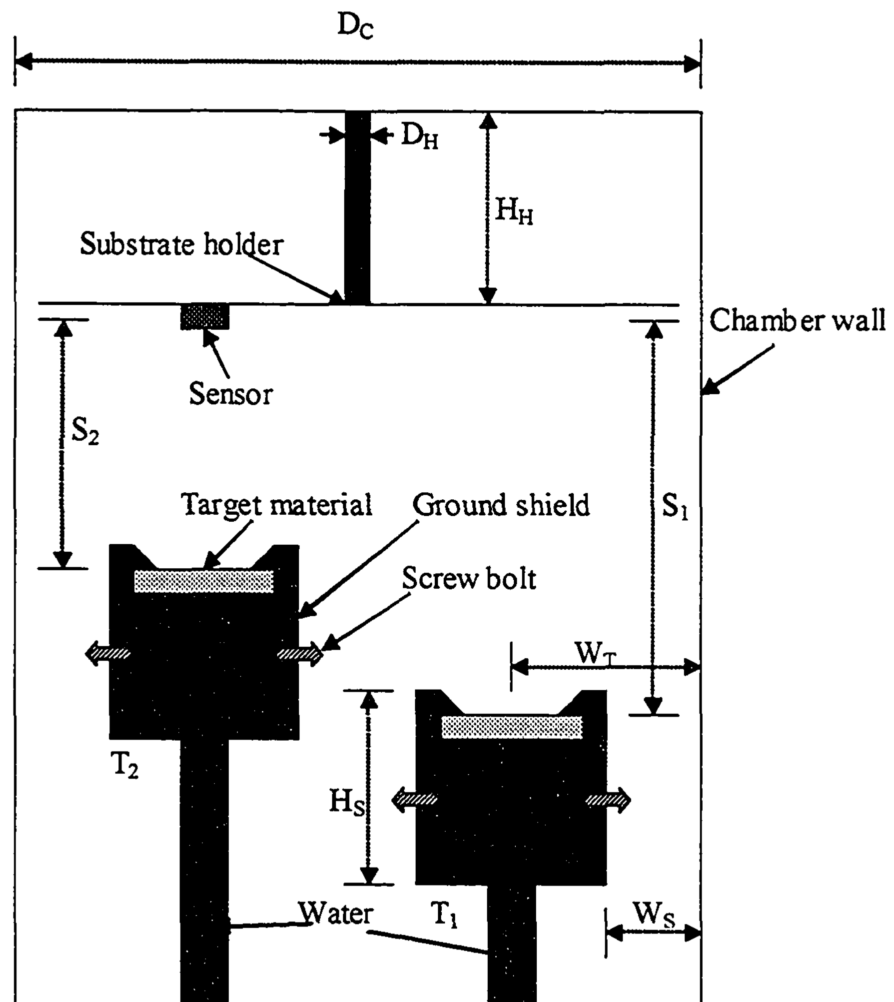

Fig. 3.10 Schematic diagram of the system used showing the locations of the sensor and target material. T_1 and T_2 are respectively targets 1 and 2.

The dimensions of the package are as follows: $L_1 = 3$ cm; $L_2 = 1.5$ cm; $B_1 = 0.67$ cm; $B_2 = 1$ cm; $B_3 = 1.5$ cm; $H_1 = 0.1$cm; $H_2 = 0.25$ cm; $H_3 = 0.9$ cm. The sensor chip surface area was approximately 0.12 cm^2, and its thickness was 0.1 cm.

Reproduced with permission of the copyright owner. Further reproduction prohibited without permission.

Top View:

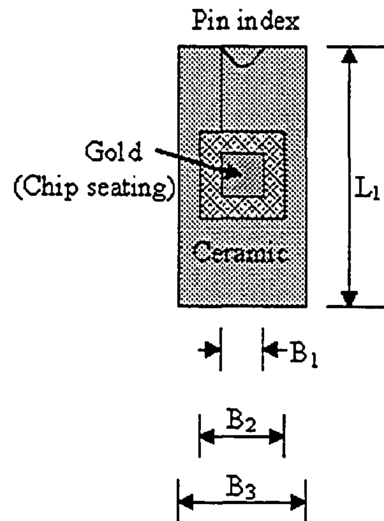

Side view cross-section:

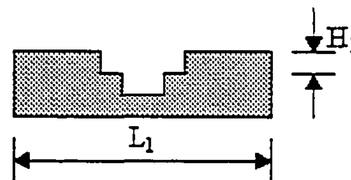

Side view: showing pins.

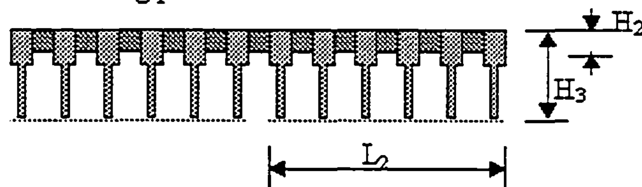

Fig. 3.11 Top, sectional and side views of the 24-pin DIP ceramic package used in wire bonding the to sensor chip.

Reproduced with permission of the copyright owner. Further reproduction prohibited without permission.

Chapter 4

Process Conditions and Results

4.1 Process Conditions

As stated earlier, several factors determine the film growth rate of any material and the amount of energy deposited at the substrate in a sputtering system. The basic factor is the flux of sputtered material arriving at the substrate. Others include the substrate effects from charged particles, neutral particles, electromagnetic radiation, sticking coefficient of sputtered particles, adatom mobility, bonding, and re-emission or backscattering of particles from the substrate [58]. These factors are difficult to control directly. Some of them, however, may be controlled in magnetron sputtering by adjusting the process parameters or conditions.

Most magnetron targets operate in the pressure range from 1 to 40 mTorr with cathode potentials of 300 – 500 V. In some cases, it may be desirable to deposit at higher pressures, since higher pressures can enhance gas-atom interactions in the plasma or at the substrate. For a given target material and gas, the parameters that can be easily adjusted are the pressure, cathode potentials, current or the applied power, and the

Reproduced with permission of the copyright owner. Further reproduction prohibited without permission.

substrate – target distance. The cathode voltage follows only a weak dependence on current of the form [152]:

$$I = kV^n \tag{4.1}$$

Since the applied power is the product of current and voltage, current and voltage may be varied by varying the power. In this work, the applied power, pressure and the substrate-target distance were adjusted to determine the substrate heating effect. Al and Cu were chosen as target materials to investigate both light and heavy (with respect to the argon sputtering gas) atoms.

Table 4.1: Mean discharge voltage and current during the deposition of aluminum at constant power mode for different magnetron powers, gas pressure of 5 mTorr and substrate – target distance of 10.8 cm.

Magnetron power (W)	Mean voltage (V)	Mean current (A)
75	359	0.21
100	375	0.27
200	410	0.49
250	425	0.59
300	430	0.70

* For all experimental settings, the maximum variability in voltage and current were 5 V and 0.01 A respectively.

Reproduced with permission of the copyright owner. Further reproduction prohibited without permission.

4.2 Results

4.2.1 Effect of Applied Power

During the deposition of aluminum, the magnetron discharge was operated at five different power levels: 75, 100, 200, 250 and 300 W. The chamber base pressure (before introducing argon) for each power level was of the order of 2.0×10^{-6} Torr. The argon gas pressure was maintained at 5 mTorr and the substrate – target distance was kept at 10.8 cm. The deposition time was 20 minutes to allow for a near steady state to be attained. Table 4.1 shows the mean discharge current and voltage for each magnetron power. The transient response of the polysilicon sensor was determined by measuring the resistance using a digital ohmmeter at one minute interval for each power level. The relative change in resistance of the probe was determined and plotted against time, as shown in Fig. 4.1. The response curves clearly show that the system is characterized by long time constants. In section 3.4.2, it was shown that the time constant for the sensor was about 5 minutes, thus the long time constant observed in this case may be due to the heating up of some other elements within the sputtering chamber.

Reproduced with permission of the copyright owner. Further reproduction prohibited without permission.

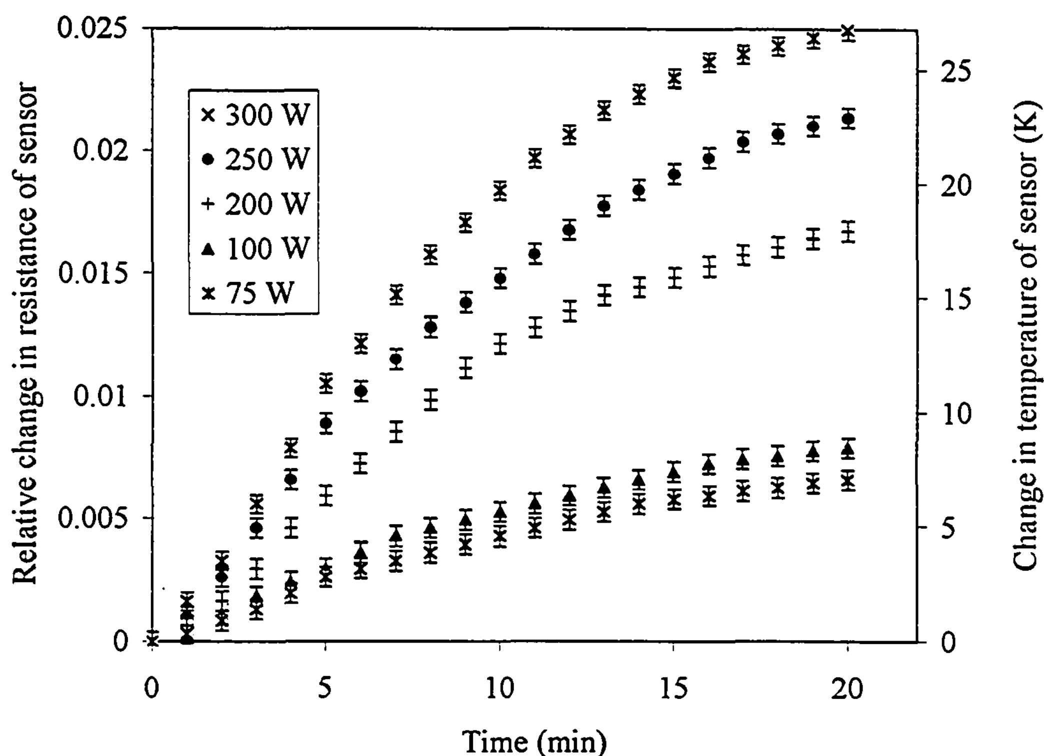

Fig. 4.1 Sensor responses during the deposition of aluminum at a gas pressure of 5 mTorr and substrate-target distance of 10.8 cm for different magnetron powers.

4.2.2 Effect of Pressure

To study the effect of pressure on the deposited energy at the substrate, the above experimental process was repeated but with the gas pressure maintained at 10 mTorr. Table 4.2 shows the mean voltage and current. As can be noted in the measured data, the discharge voltages were less than those measured at the same power but at a gas pressure

Reproduced with permission of the copyright owner. Further reproduction prohibited without permission.

of 5 mTorr. This is an indication that the discharge impedance decreases with pressure. Fig. 4.2 shows the variation in the resistance of the sensor with time. The relative changes in resistance of the sensor were less than those at 5 mTorr for each magnetron power, indicating a reduced total energy flux to the substrate.

Table 4.2: Mean discharge voltage and current during the deposition of aluminum at constant power mode for different magnetron powers, gas pressure of 10 mTorr and substrate – target distance of 10.8 cm.

Magnetron power (W)	Mean voltage (V)	Mean current (A)
75	330	0.23
100	351	0.29
200	385	0.52
250	397	0.63
300	408	0.74

Reproduced with permission of the copyright owner. Further reproduction prohibited without permission.

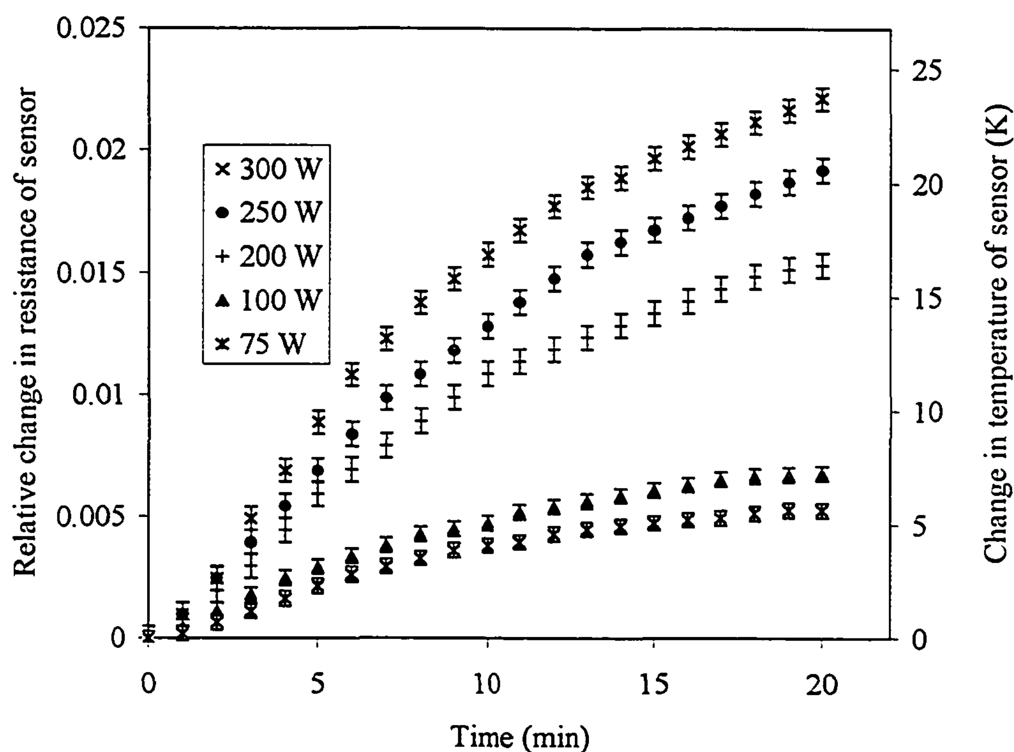

Fig. 4.2 Sensor responses during the deposition of aluminum at gas pressure of 10 mTorr, and different magnetron powers, substrate-target distance of 10.8 cm.

4.2.3 Effect of Substrate-Target Distance

The substrate – target distance was increased to 21 cm in order to study the effect of distance on the amount of deposited energy at the substrate. Magnetron powers were maintained as above for gas pressures of 5 and 10 mTorr respectively. Fig. 4.3 shows the relative change in resistance with time at gas pressure of (a) 5 mTorr and (b) 10 mTorr. The deposition times were between 20 and 25 minutes

Reproduced with permission of the copyright owner. Further reproduction prohibited without permission.

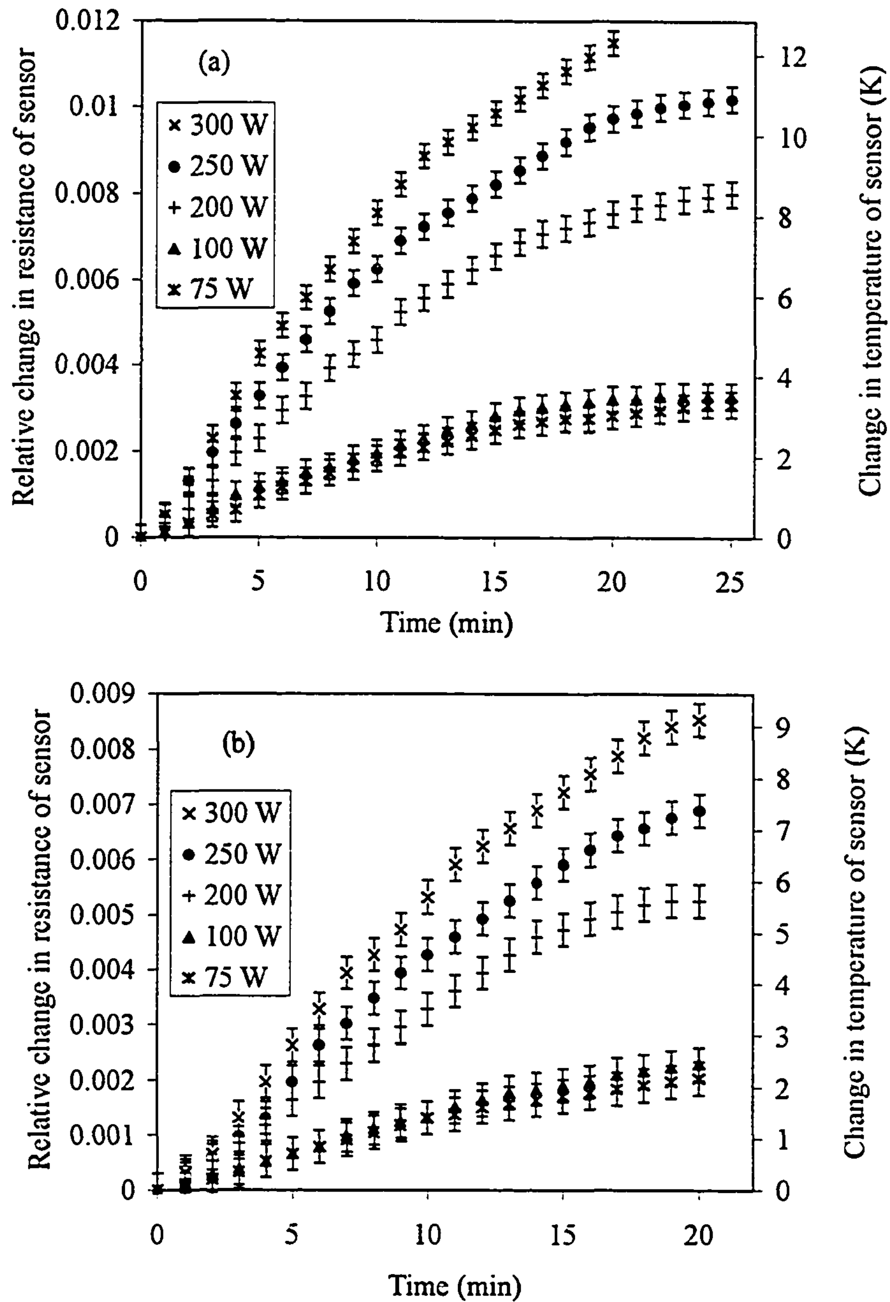

Fig. 4.3 Sensor responses at substrate-target distance of 21 cm, pressure of (a) 5 mTorr and (b) 10 mTorr.

Reproduced with permission of the copyright owner. Further reproduction prohibited without permission.

4.2.4 Effect of Target Material

To study the effect of different target materials on the deposited energy at the substrate, Al was replaced with Cu. Two magnetron power levels (75 and 300 W) at two different gas pressures (5 and 10 mTorr) were employed for the study. Mean currents and voltages obtained are shown in Table 4.3. The experimental data for the relative change in resistance with time is shown in Fig. 4.4.

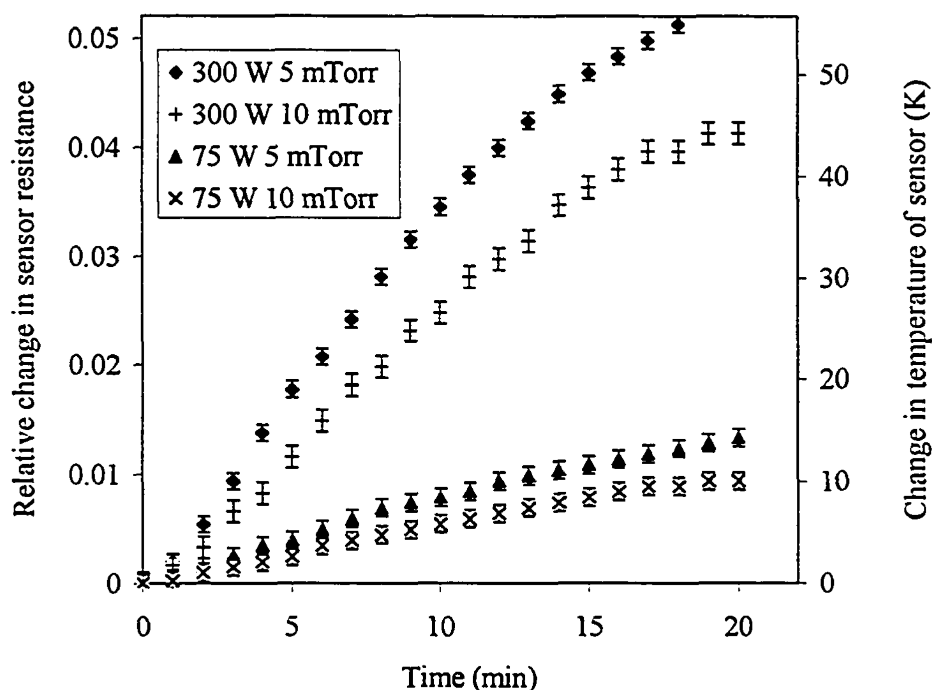

Fig. 4.4 Sensor responses during the deposition of Cu at a substrate-target distance of 10.8 cm, magnetron powers of 75 and 300 W, and gas pressures of 5 and 10 mTorr.

Reproduced with permission of the copyright owner. Further reproduction prohibited without permission.

Table 4.3: Mean discharge voltage and current during the deposition of Cu at constant power mode for two different magnetron powers for gas pressures of 5 and 10 mTorr and substrate – target distance of 10.8 cm.

Magnetron power (W)	Pressure (mTorr)	Mean voltage (V)	Mean current (A)
75	5	413	0.18
300	5	519	0.58
75	10	398	0.19
300	10	488	0.62

4.2.5 Effect of Substrate Bias

The substrate was biased at potentials between -10 and 10 V, in order to study the effect of charged particles on the deposited energy. The magnetron power was maintained at 200 W, gas pressure at 5 mTorr and the target-substrate distance at 10.8 cm. The steady state resistance of the sensor for each bias potential was measured. Table 4.4 shows the initial and final steady state resistances of the sensor for each potential employed. At a bias potential of 10 V the sensor broke down, probably as a result of the large energy flux towards it. Even replacement sensors could not withstand such a flux of energy.

Reproduced with permission of the copyright owner. Further reproduction prohibited without permission.

Table 4.4: Measured resistances of temperature sensor at different bias potentials at a magnetron power of 200 W, gas pressure of 5 mTorr and substrate – target distance of 10.8 cm.

Bias potential (V)	+Room temperature resistance of sensor (Ω)	Steady state resistance of sensor (Ω)
- 10	599	605
- 5	517	524
0	152.4	155
5	517	544
10	599	-*

+ Breakdown of some the wire bondings /or internal resistors caused the large difference observed in the room temperature resistance.

* The sensor element broke down, probably due to excessive heating

4.2.6 Determination of Plasma Properties

To determine plasma properties such as plasma and floating potentials, electron density and temperature, a Langmuir probe was inserted a few millimetres in front of the substrate. Currents were measured for different probe potentials. Fig. 4.5 shows the absolute currents for the different probe potentials at a magnetron power of 200 W, gas pressure of 5 mTorr and probe distance of about 10.8 cm from the target. From the figure, plasma and floating potentials were estimated as 2 and -15 V respectively.

Reproduced with permission of the copyright owner. Further reproduction prohibited without permission.

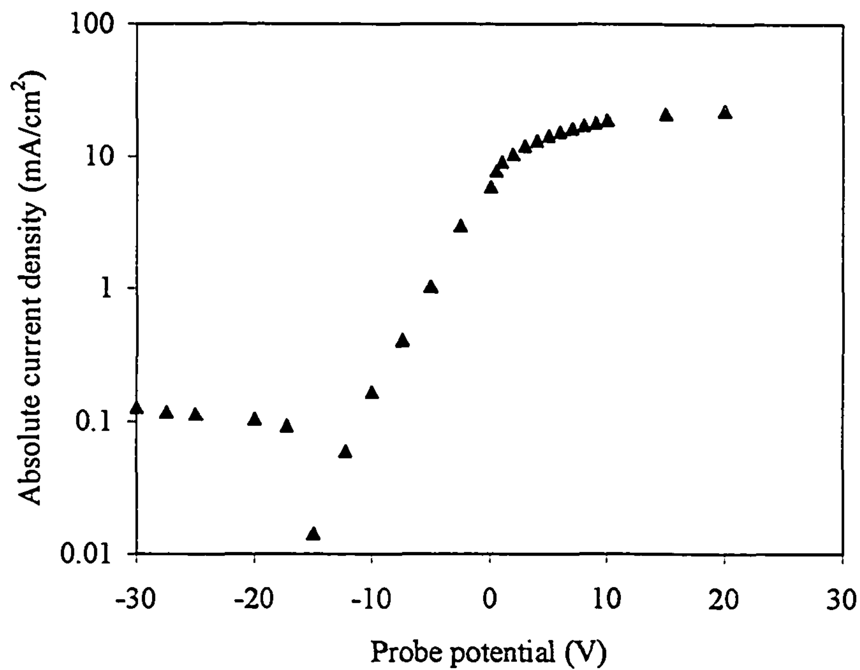

Fig. 4.5 Current voltage characteristics of a Langmuir probe in the substrate region a distance of 10.8 cm from the target for a magnetron power of 200 W and gas pressure of 5 mTorr.

4.3 Analysis of Results

The heat exchange between the sensor and its surroundings takes place mainly by thermal conduction through the physical elements of the sensor, package and the substrate holder. The gas transport component which depends on pressure and flow rate among others was

Reproduced with permission of the copyright owner. Further reproduction prohibited without permission.

shown in sections 2.5 and 3.4.2 to be negligible for the pressures under consideration. Heat transport by thermal radiation from the sensor is also negligible, since the difference in temperature between the ambient and that of the sensor was observed to be small. Thus, the first order sensor response may be expressed as in Eq. (3.19). In terms of the electrical resistance, R, of the sensor, the energy flux to the sensor may be expressed as:

$$q_{in}(t) = \frac{R - R_{RT}}{R_{RT} r_1 \alpha A (1 - \exp(-t/r_1 c_1))} \quad (4.2)$$

The values of r_1 and c_1 were determined in section 3.4.3 to be 120 K/W and 3.8 J/K respectively.

4.3.1 Variation in the Deposited Transient Energy Flux with the Magnetron Power

Figs. 4.1 and 4.2 show the relative change in sensor resistance as a function of time for different magnetron powers and pressures. These show behaviour close to the expected first order response. The curves indicate responses with long time constants, probably due to heating of the chamber elements. Clearly, the system takes a very long time to reach steady state. A typical deposition would occur during the transient stage, because of the large thermal mass of the chamber itself. Fig. 4.6 shows the energy flux as a function of time during the deposition of Al at different magnetron powers and at a substrate-target distance of 10.8 cm for (a) 5 mTorr and (b) 10 mTorr.

Reproduced with permission of the copyright owner. Further reproduction prohibited without permission.

Because of the long times involved, "near steady state" values were taken at 20 minutes, and are shown in Fig. 4.7, which indicates a trend of a linear increase in thermal flux with increasing magnetron power. For aluminum at 5 and 10 mTorr, the power transfer efficiency (ratio of the power density at the substrate to the input magnetron power) to an area at the substrate located 10.8 cm from the target is 1.6×10^{-4} and 1.4×10^{-4} cm^{-2} respectively. This value varies with pressure because of changes in ionization efficiency in the plasma and in the energy absorption rate of the gas for energetic particles coming from the target and the plasma. At a substrate-target distance of 21 cm, the power transfer efficiency reduces to 7.0×10^{-5} and 5.2×10^{-5} cm^{-2} for the two gas pressures respectively. This clearly shows that the energy transfer efficiency depends on the gas pressure and the distance of the substrate from the target.

Reproduced with permission of the copyright owner. Further reproduction prohibited without permission.

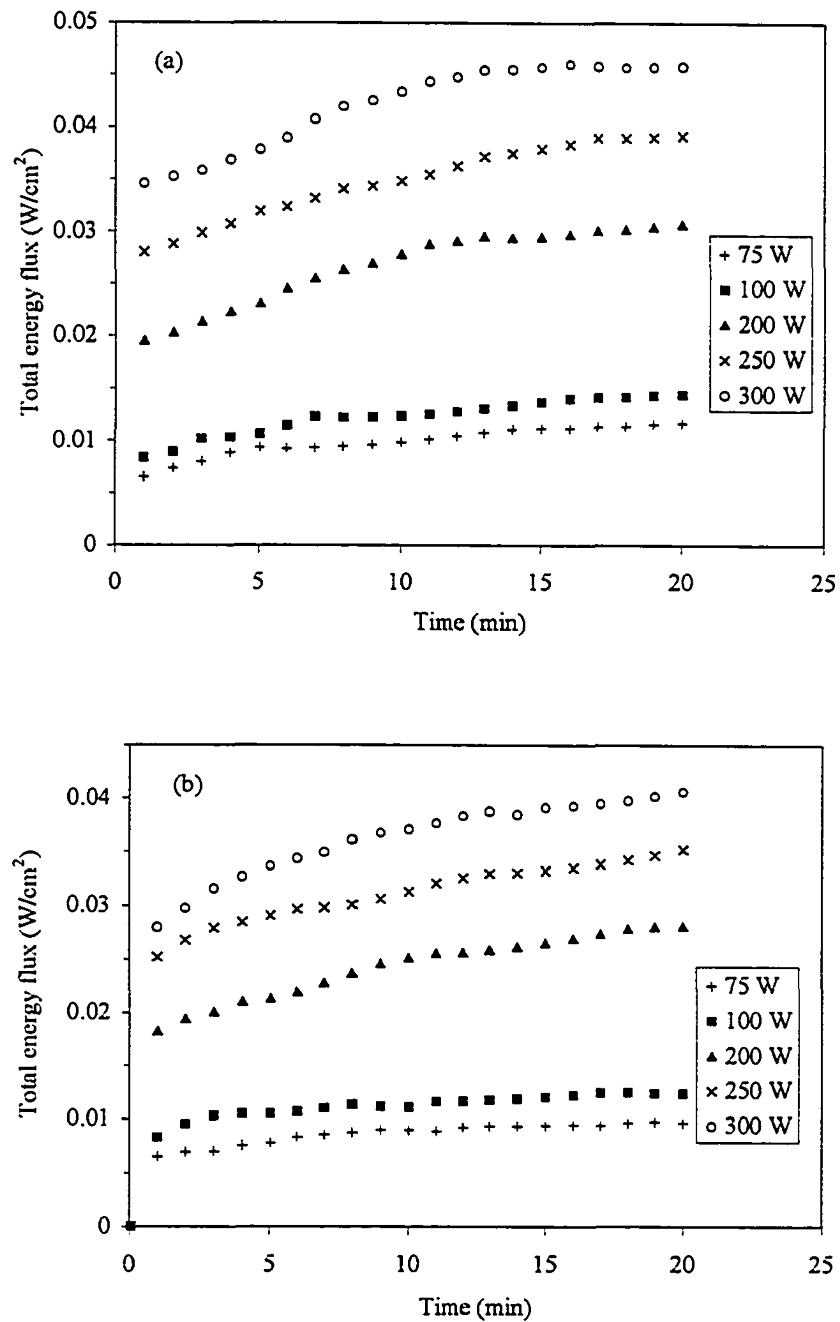

Fig. 4.6 Total energy flux at the substrate region as a function of time at a substrate-target distance of 10.8 cm and different magnetron powers for a gas pressure of (a) 5 mTorr and (b) 10 mTorr.

Reproduced with permission of the copyright owner. Further reproduction prohibited without permission.

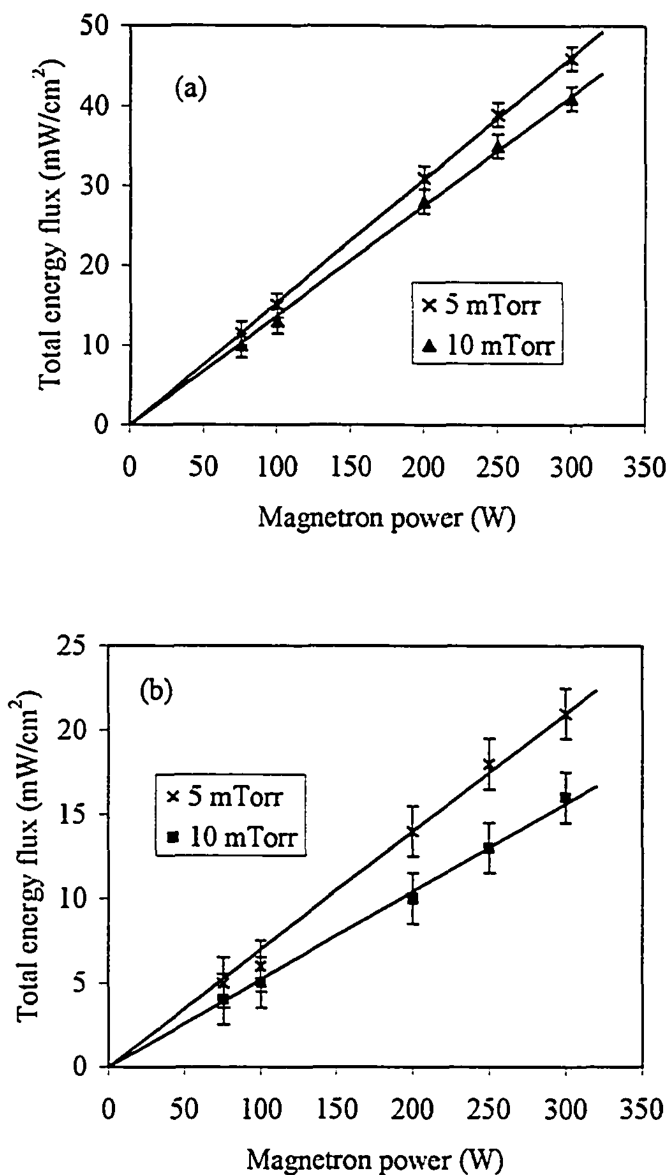

Fig. 4.7 Steady state energy flux at the substrate region as a function of magnetron power at a substrate-target distance of (a) 10.8 and (b) 21 cm for two different pressures during the deposition of Al.

Reproduced with permission of the copyright owner. Further reproduction prohibited without permission.

To examine the sensitivity to material, Fig. 4.8 shows the steady state energy flux to the substrate located at 10.8 cm from the target for the sputter deposition of copper, at 5 and 10 mTorr. The solid lines are the linear fit to the experimental data (no energy is deposited at zero magnetron power). Though there are insufficient data points, it is evident that the deposited thermal flux deviates from a direct proportionality to magnetron power. If a direct proportion is approximated to compare to aluminum, the power transfer efficiency to an area at the substrate located 10.8 cm from the target is 3.6×10^{-4} and $2.6\times10^{-4}\,cm^{-2}$ respectively. These values are higher than those of aluminum. These higher values and the deviation from the linear dependence may be attributed to the effect of the reflected neutrals on the total deposited energy. The contribution of the reflected neutral depends on the mass ratio of the target material to that of the incident ion. For the light aluminum target, the contribution of the reflected neutral is negligible; whereas, for copper, the contribution is significant. The contribution of the reflected neutrals depends on the discharge voltage. Hence, its power dependence is not linear. The high sputtering yield of copper may also help explain the high total energy flux seen for copper due to the higher particle flux towards the substrate.

Reproduced with permission of the copyright owner. Further reproduction prohibited without permission.

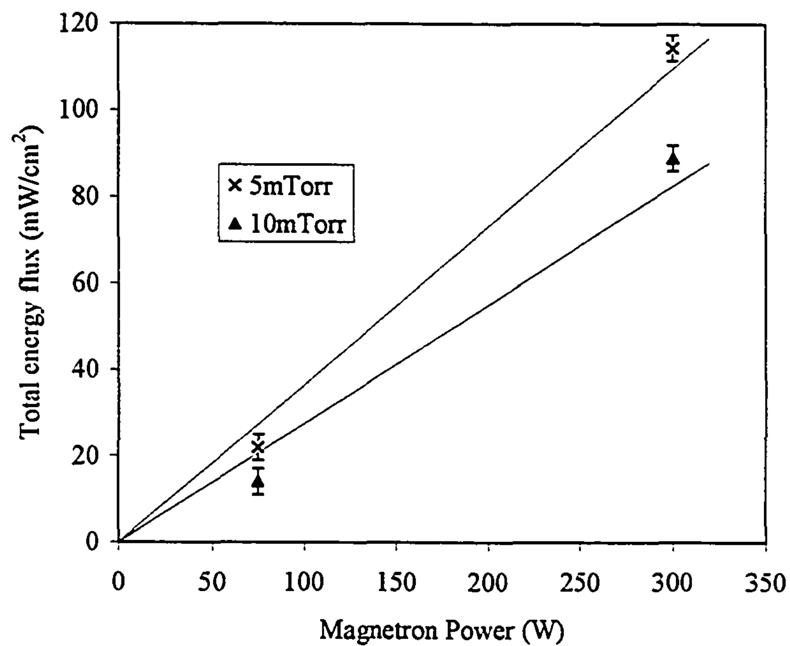

Fig. 4.8 Steady state energy flux at the substrate region as a function of magnetron power at a substrate-target distance of 10.8 cm during deposition of copper.

4.3.2 Energy Flux as a Function of Bias Potential

The energy influx due to the kinetic energy of charge carriers (electrons and ions) depends on the carrier density and temperature, and electric field in the substrate region. The mean kinetic energy of the carriers is determined by the potential difference, $V = V_{pr} - V_{pl}$, where V_{pr} and V_{pl} are respectively the probe and plasma potentials. The current – voltage characteristic of a probe at the substrate is shown in Fig. 4.5 (absolute current values). The curve reaches zero near V_{pr} = -15 V. This represents the floating

Reproduced with permission of the copyright owner. Further reproduction prohibited without permission.

potential of the plasma. The plasma potential is estimated from the knee of the curve as 2 V (± 1 V). This is consistent with the values usually used as the local plasma potential [151, 203]. The electron temperature and density during the sputtering of Al at a gas pressure of 5 mTorr and magnetron power of 200 W were estimated to be about 2.4 eV and 2.4 x 10^9 cm^{-3} respectively.

At potentials higher than the floating potential, the energy flux increases with voltage due to increasing electron current density and energy. However, at potentials higher than the plasma potential, the current density only increases slightly due to saturation, though the electrons now arrive with higher kinetic energies. If it is assumed that the plasma potential is independent of the probe potential, then the energy flux at the probe is given approximately by:

$$p = p_o + j_e(V_{pr} - V_{pl}), \qquad V_{pr} > V_{pl} \tag{4.3}$$

p_o is the energy flux at a probe potential equal to the plasma potential. Using the values of the saturated current density j_e, the thermal flux at potentials higher than the plasma potential are estimated and plotted in Fig. 4.9, along with the directly measured energy fluxes at lower potentials.

The very strong sensitivity of energy flux to probe voltage clearly indicates the important role electrons can play in heating the film and the substrate during deposition. On the other hand, ions are clearly not as important to the energy flux as even quite negative

Reproduced with permission of the copyright owner. Further reproduction prohibited without permission.

voltages do not significantly raise the overall energy flux. This is consistent with the results of Wendt, *et al* [130].

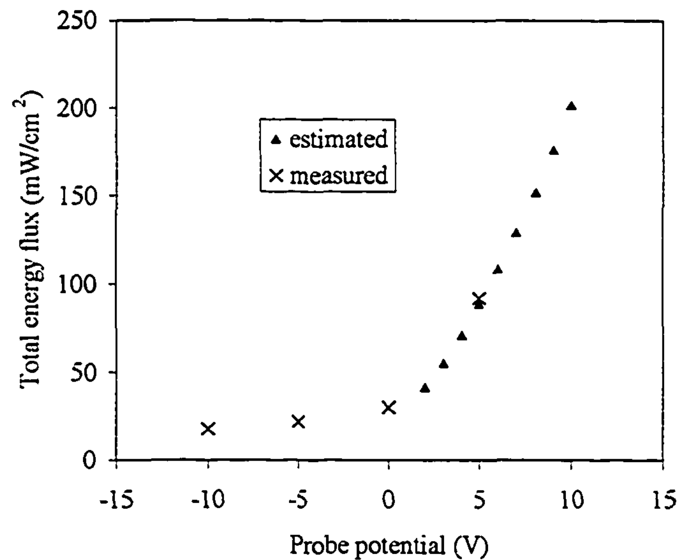

Fig. 4.9 Total energy flux at the substrate as a function of probe potential for a magnetron power of 200 W, substrate-target distance of 10.8 cm and gas pressure of 5 mTorr.

4.3.3 Total Energy per Deposited Atom

A useful way to interpret energy flux measurements is to consider them on a per deposited atom basis. As stated earlier, several factors contribute to the total energy per

Reproduced with permission of the copyright owner. Further reproduction prohibited without permission.

atom at the substrate. The contribution of each factor depends on the magnetron power and pressure.

The total energy per deposited atom E_{tot} may be evaluated by normalizing the energy flux at the substrate to the atomic deposition rate ϕ_{at}. Thus,

$$E_{tot} = q_{tr} / \phi_{at} \tag{4.4}$$

where $\phi_{at} = (d_r N_A \rho)/M$, and d_r is the average deposition rate determined from the film thickness measured using a stylus profilometer, N_A is Avogadro's constant, ρ is the density, which is usually less than the bulk density (about 0.8 times the bulk density was assumed) and M is the molar mass.

The total energy per deposited atom as a function of the magnetron power for two different gas pressures is plotted in Fig. 4.10. The experimentally determined values for the total energy per deposited atom are in the range 31 – 59 eV depending on the magnetron power and gas pressure. The results show that, at both 5 and 10 mTorr, the energy per atom decreases with increasing magnetron power. Of course both the energy flux and deposition rate increase with power. However, the deposition rate increases more quickly than the energy flux, hence the downward trend observed in Fig. 4.10.

Reproduced with permission of the copyright owner. Further reproduction prohibited without permission.

The decrease in the energy per atom with power may also be attributed to gas heating and rarefaction observed especially at high magnetron powers. Rarefaction of the filling gas adjacent to the cathode increases the impedance of the plasma and therefore affects the current-voltage characteristics of the discharge [152]. Dickson, *et al* [71] noted that a possible effect of gas heating is a decrease in electron density in ionized physical vapour deposition (IPVD). Rossnagel [63], showed that gas heating and rarefaction depend on the square root of the discharge current, which increases with magnetron power. Thus, increased gas heating with magnetron power limits the increase in the electron contribution to the total energy. Also, gas density reduction causes an increase in deposition efficiency through reduced gas scattering as well as a reduction in the contribution to the energy flux due to plasma radiation.

Fig. 4.10 also shows that by increasing the gas pressure from 5 to 10 mTorr, the energy per deposited atom increases. However, as the magnetron power is increased, the difference in the energy per deposited atom between the two pressures decreases. Such that at higher magnetron powers it trends toward being constant irrespective of both power and pressure. The observed trend shows that the plasma effects are more important, at least at lower power levels. As mentioned above, increasing pressure increases gas scattering, and hence decreases the probability of a sputtered atom depositing on the substrate.

Reproduced with permission of the copyright owner. Further reproduction prohibited without permission.

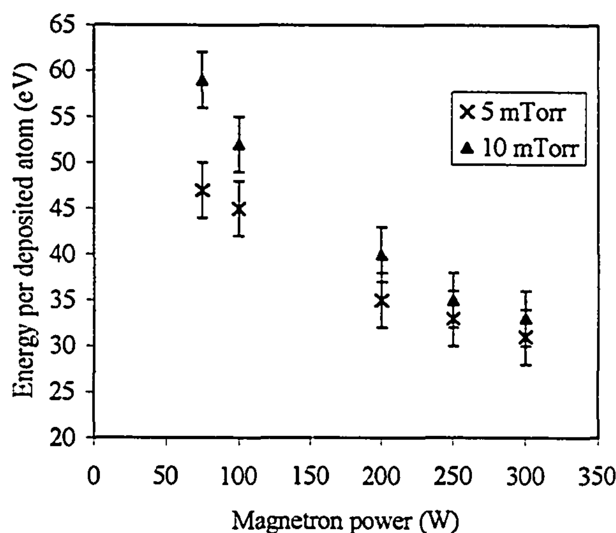

Fig. 4.10 Total energy per deposited aluminum atom as a function of magnetron power at gas pressures of 5 and 10 mTorr using a substrate-target distance of 10.8 cm.

Table 4.5 shows a summary of the estimated individual contributions to the total energy per deposited Al atom at the substrate for a magnetron power of 200 W and a substrate – target distance of 10.8 cm [127]. Contribution of the sputtered atom is the sum of its condensation and kinetic energy. The condensation energy per atom of Al is about 3.33 eV [129]. Using SIMSPUD [173], at a target voltage of 415 V, gas pressure of 5 mTorr, and distance of 10.8 cm, the kinetic energy of the sputtered atom is estimated as 5.1 eV.

Reproduced with permission of the copyright owner. Further reproduction prohibited without permission.

If the energy at potentials higher than the plasma potential is assumed to be mainly from electrons, then the contribution of electrons to the total power flux is given by Eq. (4.3). Thus, the contribution of electrons may be estimated from the difference between the measured power at the floating potential and that at the plasma, to give about 10.6 eV per deposited atom. The contribution of the plasma radiation is estimated as 12.9 eV (details are presented in section 5.2). The sum of these contributions compares with the measured. The major sources of energy are the plasma radiation and electrons. For the un-biased substrate, the positive ions are not a significant source compared to other sources. The value for the sputtered atoms consists of both the condensation energy and the kinetic energy. By separating them, the contribution due to the kinetic energy alone is about 5 eV at that distance. This value is about the same range as that due to thermal radiation from the hot ground shield around the target.

It is expected that the estimated values may deviate from the actual values given the method of estimation. For instance in estimating the kinetic energy, the gas heating effect was not taken into consideration. Thus, by scaling this effect in SIMSPUD, the value of the kinetic energy was found to increase by about 0.8 eV. So this was taken as an indication of the uncertainty of this contribution. Some of the radiant energies (such as plasma radiation) may be reflected from the surface of the growing film, thus, the actual absorbed radiant energy may be less than the estimated value. However, through multiple

Reproduced with permission of the copyright owner. Further reproduction prohibited without permission.

reflections from the rough surface [204] of the film and the surrounding walls, some of the reflected energy may be deposited onto the growing film. It should also be noted that the reflection coefficient decreases with energy [205]. By taking into consideration the view factor of the sensor with respect to the source, the uncertainty in estimating this energy was obtained at about 2 eV. Also the estimation of the contribution of electrons is strongly affected by the uncertainty in measuring the electron current at the tip of the Langmuir probe as well as the indirect determination of the plasma potential. The accumulative effect of these is estimated to be about 1 eV.

Table 4.5: Estimated contributions to the total energy per deposited Al atom at the substrate for a magnetron power of 200 W, pressure of 5 mTorr and substrate – target distance of 10.8 cm.

Factors	Energy per deposited atom (eV)	Percentage contribution (%)
Sputtered atom	8.4 ± 0.8	23
Electrons	11 ± 1	30
Plasma irradiation	13 ± 2	36
Thermal irradiation	4.2 ± 0.5	11
Sum	37 ± 4	100
Measured	39 ± 3	

Reproduced with permission of the copyright owner. Further reproduction prohibited without permission.

Chapter 5

Theoretical Models and Discussions

Thornton [129] provided the basis for interpreting the energy flux to a growing film in terms of the energy per deposited atom. Since it is not plausible to measure this energy directly, it is always determined from the total deposited energy and the total depositing flux. Thus, for a theoretical determination of this energy, a model of the deposition rate with that of the total energy is required. Knowledge of the functional dependence of those factors contributing to the total energy on the external parameters, which can be controlled, is very important for accurate modeling of the energy deposition in a sputter system.

5.1 3-D Deposition Rate Model

It is convenient to idealize the depositing flux as a mix of slow and fast particles [206]. Atoms emitted from the target are generally fast, but they slow down as a result of collisions with the gas atoms. An accurate model of depositing flux must consider the contributions of both populations. In the treatment below, the fast particles are those,

Reproduced with permission of the copyright owner. Further reproduction prohibited without permission.

which traverse ballistically in straight lines to the substrate without scattering. The slow particles are presumed to transport by diffusion.

The flux of particles emitted at the target surface may be determined from the product of the differential sputtering yield and the target ion current density. The sputtering yield depends on the ion energy and the target material sputtering threshold [207]. Ion energy is proportional to the target voltage with the constant of proportionality close to unity for cases where the dark space thickness is small compared to the mean free path for charge exchange collisions.

For planar magnetron sputtering, the ions are usually assumed to have normal incidence at the surface. Hence, for simplification purposes, the total sputtering yield is used, and the emitted flux for normal incident ion would be the product of the ion current density, j, and the total target sputtering yield, Y, as a function of the emission position on the target. The ion current density may be determined from the total discharge current. In a magnetron system, the dependence of current on voltage is given in Eq. (4.1). The values of κ and n depend strongly on the target-gas combination, system geometry, magnetic field and other experimental parameters. Target-gas combinations with higher yield have a lower value of n than those with a low yield. Fig. 5.1 shows the experimental I-V values

Reproduced with permission of the copyright owner. Further reproduction prohibited without permission.

for copper and aluminum, as well as a fit of Eq. (4.1) to the experimental data, for a gas pressure of 5 mTorr for the magnetron sputter system used.

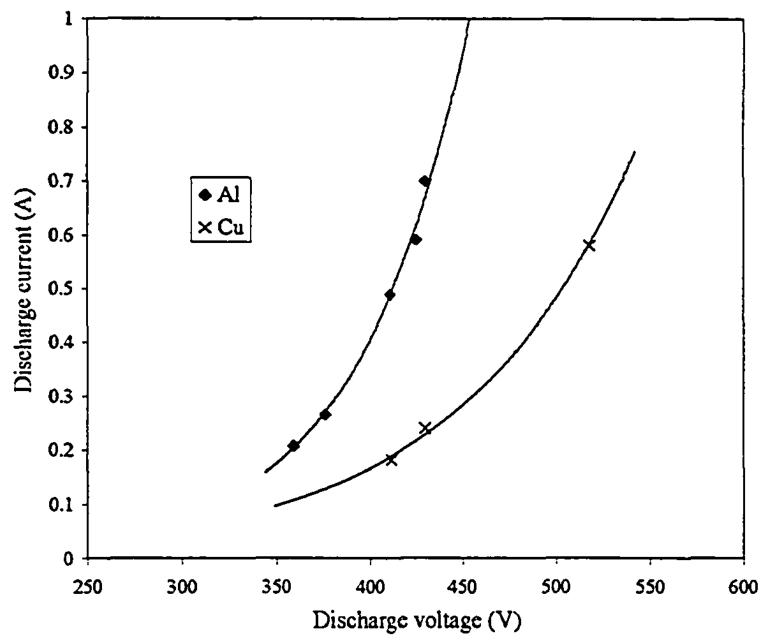

Fig. 5.1. Current – voltage characteristics of a dc magnetron discharge for Al and Cu at a gas pressure of 5 mTorr. The solid curves are fits to Eq. (4.1).

Reproduced with permission of the copyright owner. Further reproduction prohibited without permission.

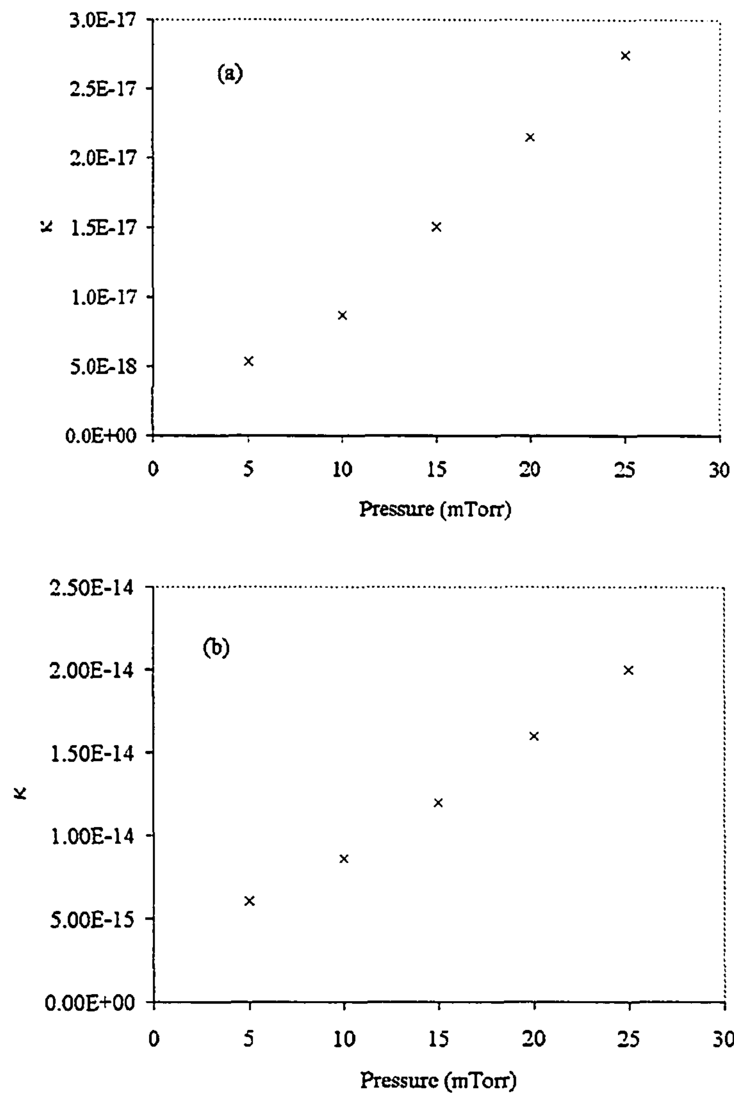

FIG. 5.2. Variation in the experimental value of κ (admittance factor) on gas pressure during the deposition of (a) Al and (b) Cu, given the 75 mm magnetron sputter deposition system used.

Reproduced with permission of the copyright owner. Further reproduction prohibited without permission.

The values of n calculated at this pressure for this system were 5.15 and 6.5 for Cu and Al, respectively. Similarly, the calculated values of κ were of the order of 10^{-15} and 10^{-18} for Cu and Al respectively, to give current in amperes. In another K. J. Lesker Magnetron System (herein referred to as system 2), the corresponding values are of the order of 6.04 and 10^{-15} for Cu, and 6.72 and 10^{-18} for Al, respectively. Since κ is a function of the system impedance, it varies with pressure. Fig. 5.2 shows the dependence of κ on pressure for (a) Al and (b) Cu. At pressures below 15 mTorr, κ seems to have an exponential dependence on pressure, whereas, at higher pressures, it seems to indicate a linear dependence on pressure.

A planar magnetron has the inherent problem of inhomogeneous erosion of the target surface, due to the magnetic arrangements. The ejection points are within an annulus referred to as the "erosion ring" between radial distances r_1 (inner radius) and r_2 (outer radius) from the centre of the target. As the depth of the erosion increases, the separation between r_1 and r_2 decreases (r_1 moves farther away from the target centre and r_2 moves towards it). Thus, for a given discharge current, the resulting current density increases with the depth of erosion. The above has an effect on the deposition uniformity and profile. The location of the onset of a more uniform film would be determined by r_1, since it determines the filling of flux along the central axis.

Reproduced with permission of the copyright owner. Further reproduction prohibited without permission.

Since the depositing flux is the sum of the fast moving and the slow moving flux, the following will treat these two types of flux emitted from a circular planar target.

5.1.1 Fast Moving Particles

It is common to express the flux density of the fast atoms at the substrate, a distance ρ from the target as: [177,178,206]

$$\phi_f = \phi_d \exp\left(-\frac{\rho}{\lambda_m}\right) \tag{5.1}$$

This may be expressed as [175];

$$\phi_f = \phi_d \exp(-\mu P \rho) \tag{5.2}$$

where μ is dependent on the mean free path of the atoms, determined by the gas-target combination and the applied power due to gas rarefaction effect. The total energy put into the gas depends on average kinetic energy, E, of the ejected atom from the target, sputtering yield, Y, and the discharge current, I. The gas heating effect is limited by the part of the energy conducted to the chamber walls, which of course depends on the thermal conductivity, κ of the gas. According to Rossnagel, [63] the density, n_g of the hot gas is given by:

Reproduced with permission of the copyright owner. Further reproduction prohibited without permission.

$$n_g = \left(\frac{2n_0T_0\pi f\kappa}{EIY\sigma}\right)^{0.5} \tag{5.3}$$

where n_0 and T_0 are respectively the density and temperature of the unheated gas, σ is the collision cross-section for momentum transfer, and f is equal to the number of mean free paths away from the cathode (which was assumed to be 3). In this case, the mean free path is taken as:

$$\lambda_m = \frac{kT}{P\sigma} \tag{5.4}$$

Since the pressure in the plasma region is assumed the same as the system pressure, then Eq. (5.3) may be written in terms of the gas temperature as:

$$T = \left(\frac{\sigma PEIY}{k6\pi\kappa}\right)^{0.5} \tag{5.5}$$

By replacing Eq. (5.4) in Eq. (5.5) and combining it with Eq. (2.5), σ may be eliminated, and the hot gas temperature obtained as:

$$T = \frac{E^{1/3}}{(1.5k)^{1/9}}\left(\frac{IYP}{\gamma A\pi\kappa}\right)^{4/9} \tag{5.6}$$

If Eq. (5.6) is substituted into Eq. (2.5), μ can be obtained as:

$$\mu = \left(\frac{\pi\kappa}{IYP}\right)^{5/9}\frac{1}{(1.5k)^{1/9}A^{4/9}E^{2/3}} \tag{5.7}$$

Eq. (5.7) shows the effect of those factors, which contribute to the gas heating on the parameter μ.

Reproduced with permission of the copyright owner. Further reproduction prohibited without permission.

The value of ϕ_d is the zero pressure flux, which has been assumed elsewhere [176–178] to be the product of the current density, j and the total sputtering yield, Y (for planar magnetron, the ions usually strike the target with normal incidence). However, given the emission pattern of the sputtered flux, even if there were no gas phase collisions (zero pressure condition), it will scale with distance, and may be determined in terms of the angular distribution of the emitted particles at the target (which is determined by the discharge voltage) [88,207].

To account for the under/over cosine distribution for normal incidence, the $\cos^{\alpha}\theta$ is often used [208]. In order to properly account for the shape profile, Yamamura, *et al*, [209] proposed a fitting formula of the form:

$$S(\theta) \approx \cos\theta\left(1+\beta\cos^2\theta\right) \tag{5.8}$$

where θ is the ejection angle of the sputtered atoms with respect to the surface normal and β is a fitting parameter. The fitting parameter depends on the mass and binding energy of the target material, mass of gas, and ion energy. It may be expressed as:

$$\beta = B\ln Q - B_c \tag{5.9}$$

$$Q = \left(\frac{M_t E_0}{M_g U_s}\right)$$

where M_t is the mass of the sputtered atom, U_s is the binding energy of the sputtered material and E_0 is the incident ion energy. For Ar^+ on Cu at 100, 600, 1000, 5000 eV,

Reproduced with permission of the copyright owner. Further reproduction prohibited without permission.

they obtained the best-fit β-values of −0.611, 0.284, 0.603 and 1.25, respectively. The values of B and B_c, were respectively approximated as 0.488 and 2.44. These values are in most cases independent of the target material. Eq. (5.8) implies that the negative β value predicts the under-cosine distribution, while the positive β value predicts the over-cosine distribution. Thus,

$$\phi_d = j(r)YS(\theta) \tag{5.10}$$

Using Eqs. (5.2) and (5.7), and from Fig. 5.3 (a), the flux density of the particles sputtered from an element area dA_T of the target reaching an element area dA_S of the substrate may be expressed as:

$$d\phi_f = jY\exp(-C\rho)dA_T d\Omega / dA_S \tag{5.11}$$

where $C = \mu P$, $d\Omega = dA_S \cos\theta / \rho^2$, $\cos(\theta) = z/\rho$. For a planar circular target, $dA_T = rdrd\varphi$. The total flux density of the fast moving sputtered particles at the substrate may be obtained by integrating Eq. (5.11) over the area of the target etch track as:

$$\phi_f = \int \frac{j(r)Yz^2\left(1+\beta\left(z/\rho\right)^2\right)}{\rho^4} \exp(-C\rho) rdrd\varphi \tag{5.12}$$

Reproduced with permission of the copyright owner. Further reproduction prohibited without permission.

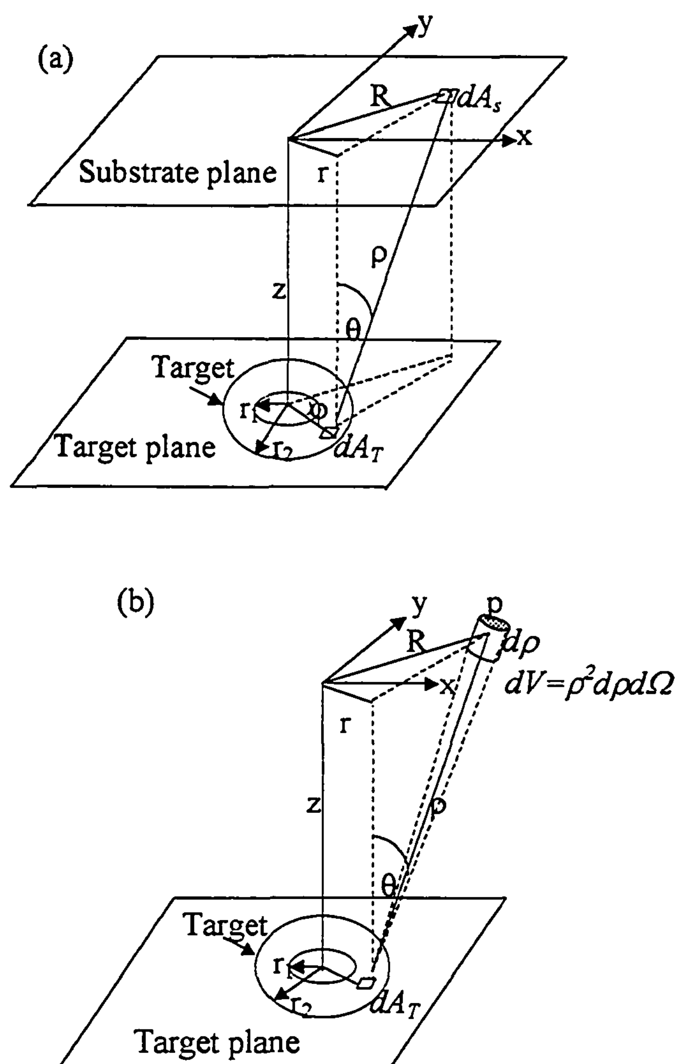

Fig. 5.3 System geometry used in modeling the flux of (a) fast and (b) slow moving atoms from the target plane onto the substrate plane.

Reproduced with permission of the copyright owner. Further reproduction prohibited without permission.

Using the geometry of Fig. 5.3 (a), $\rho = \sqrt{\left(z^2 + r^2 + R^2 - 2rR\cos\varphi\right)}$. Where $r_1 \le r \le r_2$, $0 \le \varphi \le 2\pi$ and $R = \sqrt{\left(x^2 + y^2\right)}$ Eq. (5.12) may be integrated numerically for the total depositing rate of the fast moving particles at the substrate.

5.1.2 Slow Moving Particles

These are the scattered particles, which move by diffusion [206, 210]. The concept of diffusion applies to the flow of one medium in another under the influence of the density gradients and the thermal motion of the particles in the two media (gas and sputtered particles) [211]. Here the simple form of diffusion in which the concentration of the diffusing matter (slow moving particles) is small in comparison with the concentration of the medium (gas) in which it is diffusing is considered.

As a result of the slowing down process through gas scattering, the source term for the diffusion equation is not located at the target. Rather, a distributed source model is needed [210]. With this model, sputtering can then be considered a source for diffusion only after the sputtered particles are scattered by collision. The concentration, n, of the sputtered atoms, which have made at least one collision, may be obtained by considering Fig. 5.3 (b). The particles emitted from an element area of the target, which have reached a point, p without scattering is:

Reproduced with permission of the copyright owner. Further reproduction prohibited without permission.

$$\Phi_f = jYS(\theta)rdrd\varphi d\Omega \exp(-C\rho) \tag{5.13}$$

If pressure were zero (no gas phase scattering), the total particles at p would be:

$$\Phi_0 = j(r)YS(\theta)rdrd\varphi d\Omega$$

Thus, the particles scattered from the streaming flux is:

$$\Phi = j(r)YS(\theta)rdrd\varphi d\Omega[1 - \exp(-C\rho)] \tag{5.14}$$

The density (in atoms cm^{-3} s^{-1}) of the particles scattered into an element volume, $dV = d\Omega \rho^2 d\rho$, from the flux emitted from the target element is given by [212]:

$$\frac{d\Phi}{dV} = \frac{CjYS(\theta)}{\rho^2} rdrd\varphi \exp(-C\rho) \tag{5.15}$$

Since this represents the rate of change of the density of the particle, it may be used as the source density of a conservation equation as [210]:

$$\frac{d}{d\rho}\left(-D\frac{dn}{d\rho}\right) = \frac{CjYS(\theta)}{\rho^2} rdrd\varphi \exp(-C\rho) \tag{5.16}$$

where D is the diffusion coefficient. But, from Fick's first law, the diffusing flux is given by: $\phi_s = D\frac{dn}{d\rho}$, thus,

$$\phi_s = \int \frac{CjYz\left(1 + \beta\left(z/\rho\right)^2\right)}{\rho^3} rdrd\varphi \exp(-C\rho)d\rho, \qquad 0 \le \rho \le \infty \tag{5.17}$$

The total diffusing flux at the point, p, due to the emitted flux from all the target elements is:

Reproduced with permission of the copyright owner. Further reproduction prohibited without permission.

$$\phi_s = zCjY \int_{r_1}^{r_2} \int_0^{2\pi} \int_0^{\infty} \frac{rdrd\varphi\left(1+\beta\left(\frac{z}{\rho}\right)^2\right)}{\rho^3} \exp(-C\rho)d\rho \tag{5.18}$$

This flux diffuses into all directions. Since, the solid angle of the point as seen from all space is 4π, the flux diffusing in a given direction would be [213]:

$$\phi_s = \frac{zCjY}{4\pi} \int_{r_1}^{r_2} \int_0^{2\pi} \int_0^{\infty} \frac{rdrd\varphi\left(1+\beta\left(\frac{z}{\rho}\right)^2\right)}{\rho^3} \exp(-C\rho)d\rho \tag{5.19}$$

Eq. (5.19) can be integrated numerically for the total flux of slow moving particles. Here, Simpson's rule was adopted in during the integrations of Eqs. (5.12) and (5.19).

The total depositing flux at the substrate is therefore the sum of the fast moving flux expressed in Eq. (5.12) and the slow moving ones expressed in Eq. (5.19).

$$\phi = \phi_f + \phi_s \tag{5.20}$$

5.1.3 Results and Discussions

The values of r_1 and r_2 as measured from the targets used were 0.9 and 3.25 cm respectively. This etch track would be herein referred to as "NT". For a magnetron power of 200 W and argon pressure of 15 mTorr, the calculated deposition rate of sputtered Al is shown in Fig. 5.4 (a). The figure shows that the profile of the deposition rate is highly dependent on the substrate position, which is a function of the radial distance R from the

Reproduced with permission of the copyright owner. Further reproduction prohibited without permission.

target central axis, and the height, z from the target plane. Along the central axis, the deposition rate increases greatly with z, up to a maximum and then decreases. However, above the etch tracks, the deposition rate decreases with z. Usually, when the target is used for a while, the width of the etch track (erosion ring) reduces. To test for the effect of the width of the etch track on the shape of the thickness profile, r_1 was increased to 1.4 cm, and r_2 decreased to 2.5 cm (small etch track, ST), the calculated result is shown in Fig. 5.4 (b) for the same process conditions. A higher deposition rate is obtained above the etch tracks than in the former case. This may be attributed to a higher current density (same total current) since the area of the etch track is less. However, as observed in that Fig. 5.5 (ST 15 mTorr), a lower deposition rate is obtained along the central axis of the target, compared to the first case (NT 15 mTorr). The effect of a wider etch track (larger target, LT), with r_1 and r_2 as 3.15 and 7.0 cm, respectively, on the deposition profile is also shown in Fig 5.4(c) (LT 15 mTorr). The magnetron power in this case is set at 775 W, to give the same power density as in the first scenario. A lower deposition rate is obtained along the central axis, at regions close to the target, probably due to a longer effective distance from the erosion track to the centre (larger deposition area). However, at larger distances from the target, the deposition rate is higher than in the former cases. It is observed from all three cases that the location of the peaks, along the central axis, with respect to z depends on the inner radii of the etch tracks.

Reproduced with permission of the copyright owner. Further reproduction prohibited without permission.

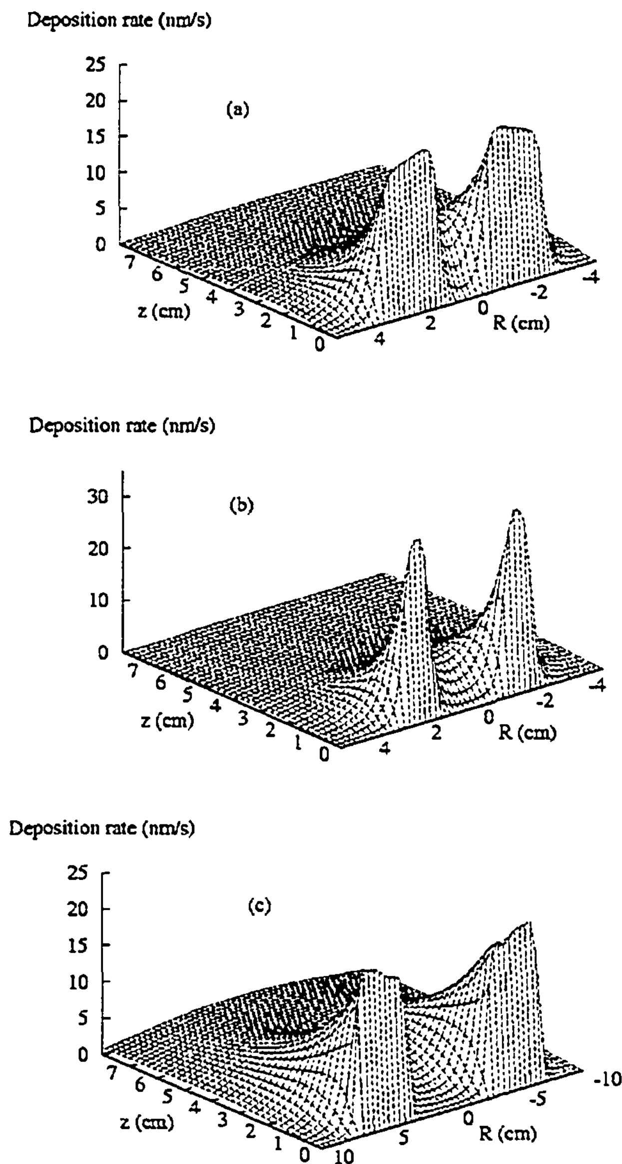

FIG. 5.4. Deposition profile of Al atoms at an argon pressure of 15 mTorr and power of 200 W. The inner and outer radii of the etch track are respectively (a) 0.9 and 3.25 cm, (b) 1.4 and 2.5 cm, and (c) 3.1 and 7 cm. (c) is at a power of 775 W.

Reproduced with permission of the copyright owner. Further reproduction prohibited without permission.

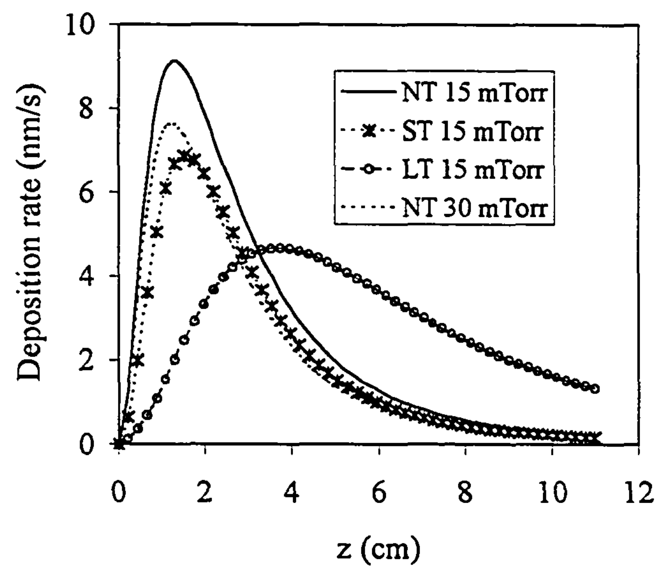

Fig. 5.5. The on axis deposition rate as a function of distance at a magnetron power density of 6.3 W/cm^2, argon pressure of 15 mTorr for etch track radii 0.9 and 3.25 cm (NT 15 mTorr), 1.4 and 2.5 cm (ST 15 mTorr) and 3.15 and 7.0 cm (LT 15 mTorr), and pressure of 30 mTorr and radii 0.9 and 3.25 cm (NT 30 mTorr) during the sputter deposition of Al.

Reproduced with permission of the copyright owner. Further reproduction prohibited without permission.

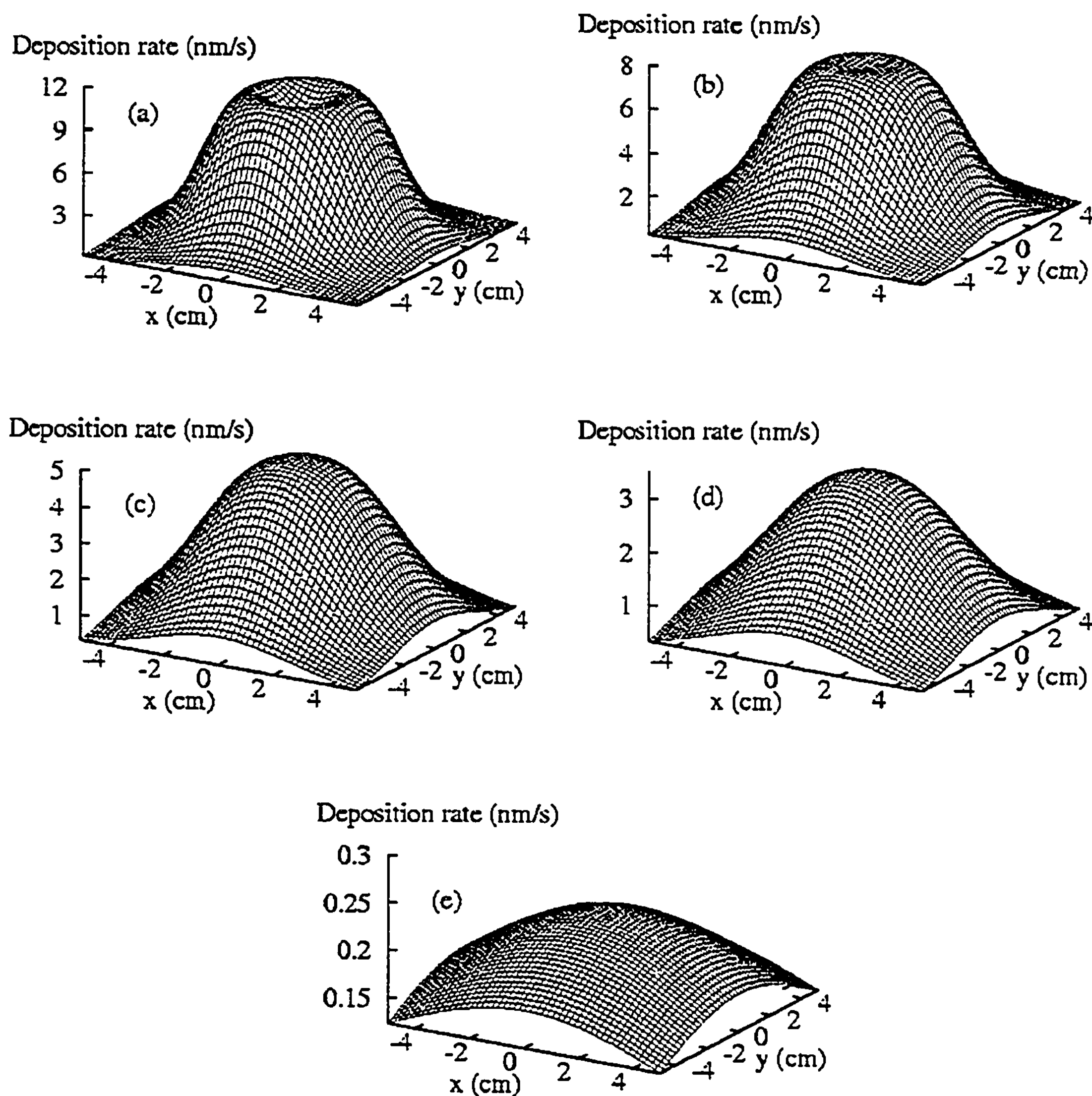

Fig. 5.6 Dependence of film uniformity on the etch track radii (0.9 and 3.25 cm respectively (NT)) for substrate located at (a) 1.1, (b) 2, (c) 3, (d) 4 and (e) 11 cm.

Reproduced with permission of the copyright owner. Further reproduction prohibited without permission.

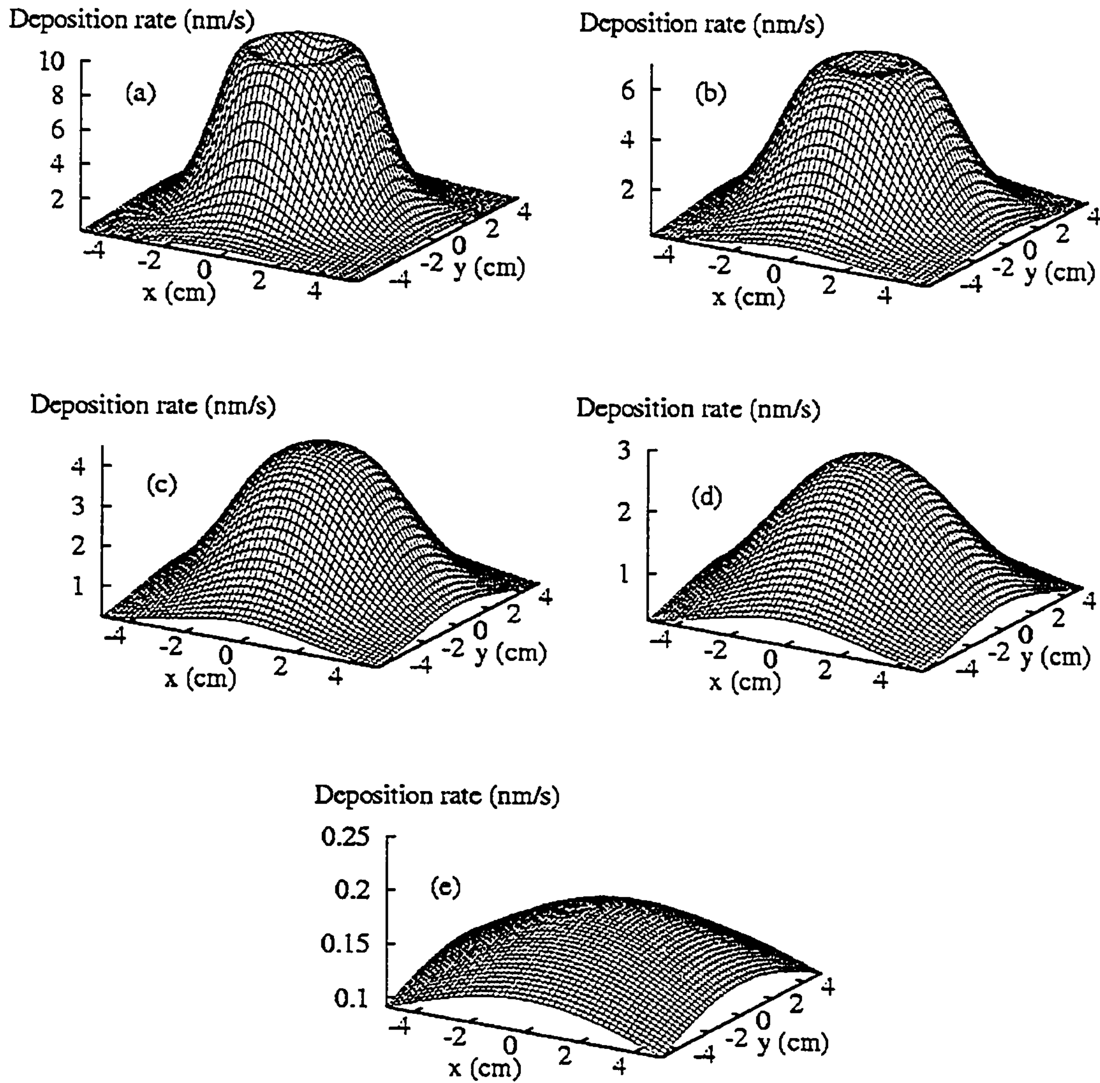

Fig. 5.7 Dependence of film uniformity on the etch track radii (1.4 and 2.5 cm respectively (ST)) for substrate located at (a) 1.1, (b) 2, (c) 3, (d) 4 and (e) 11 cm.

Reproduced with permission of the copyright owner. Further reproduction prohibited without permission.

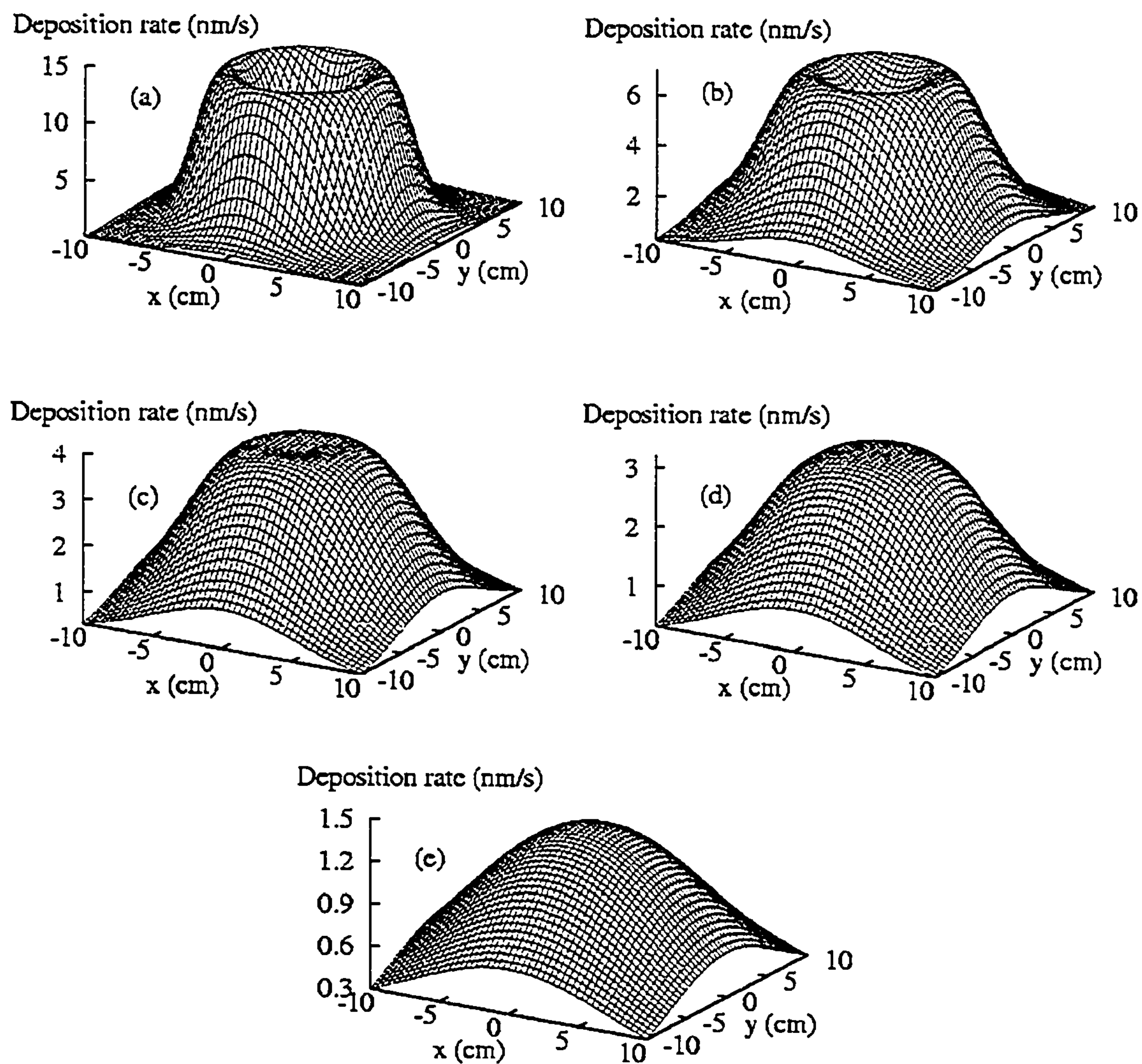

Fig. 5.8 Dependence of uniformity of thickness of film on the etch track radii (3.15 and 7 cm respectively (LT)) for substrate located at (a) 1.8, (b) 4, (c) 6, (d) 7 and (e) 11 cm.

Reproduced with permission of the copyright owner. Further reproduction prohibited without permission.

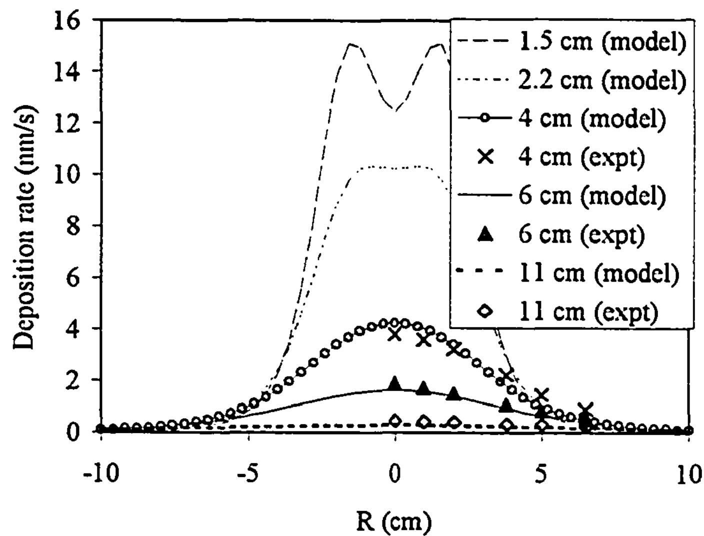

Fig. 5.9. Effect of substrate location on film uniformity, for a sputter deposition of Al at magnetron power of 200 W and gas pressure of 15 mTorr. Also shown are the experimental data for different radial distances.

Uniformity of film thickness depends on the size of the etch track as well as the location of the substrate above the target. Figs 5.6 (NT), 5.7 (ST) and 5.8 (LT) compare the uniformity of the film for the three sizes of the track at various locations above the target. From the results, it is noted that the uniformity is very poor for those locations very close to the target, $z < 2r_1$. The film is thickest at the circumference of a circle of radius of about $0.7r_2$. However, as the substrate distance is increased, a more uniform film is

Reproduced with permission of the copyright owner. Further reproduction prohibited without permission.

obtained. The effect of the inner radius (r_1), is observed in a shift of the location of the uniform film away from the target. For instance, a near uniform film is obtained at a distance of 2 cm for NT, whereas, a similar profile is obtained at about 3 cm for ST and at about 6 cm for LT. However, at about 4 cm, the shape profiles for NT and ST appear the same. Generally, it is noted that a more uniform film would be obtained at the substrate locations $z \geq 2r_1$. The spatial area of the "flat top" of the deposited film depends on the area of the etch track, and decreases with the substrate distance from the target, such that at long distances, a cone like shape is obtained. Fig. 5.9 compares the model results with the experimental values for z = 4.0, 6.0 and 11.0 cm along the substrate radial distances, as a test of the validity of the model. The results compare very well in both relative trends and absolute value.

As expected, an increase in pressure (with other process conditions maintained) results in a decrease in the deposition rate (see Fig. 5.5 NT 30 mTorr). The location of maximum deposition shifts slightly towards the target. Fig. 5.10 shows the calculated on-axis deposition rate alongside the experimental data for a magnetron power of 300 W at a distance of 10.8 cm for different argon gas pressures for the sputter deposition of (a) Al and (b) Cu (system 1). The theoretical data compare well with the experiment. The rapid decrease in deposition rate with pressure is obtained at low pressures where the

Reproduced with permission of the copyright owner. Further reproduction prohibited without permission.

depositing flux is dominated by the fast moving particles. At higher pressures, where the flux is dominated by the slow moving particles, the decrease becomes more gradual.

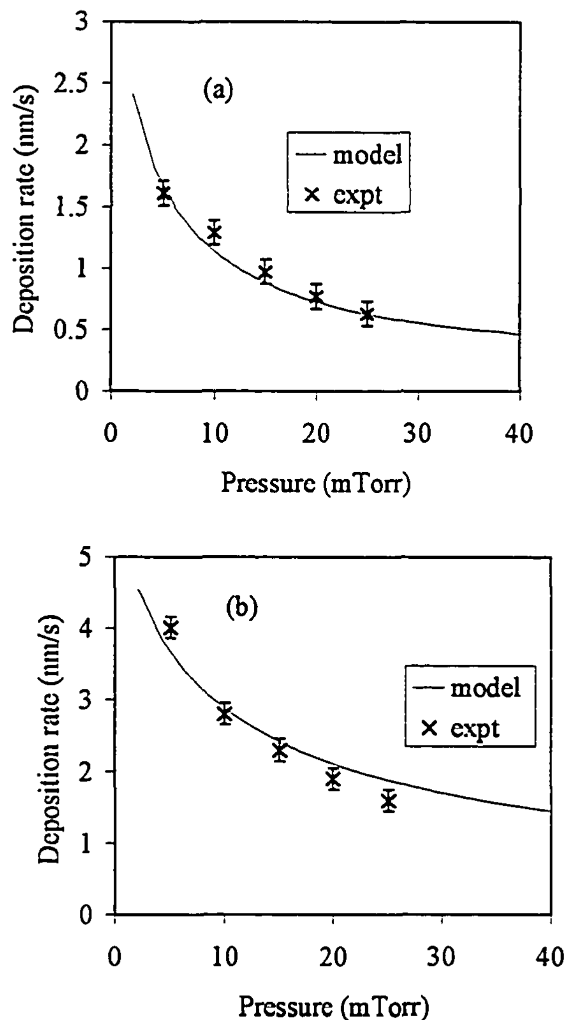

Fig. 5.10. On-axis deposition rate as a function of pressure at magnetron power of 300 W and target-substrate distance of 10.8 cm during the sputter deposition of (a) Al and (b) Cu.

Reproduced with permission of the copyright owner. Further reproduction prohibited without permission.

The effect of target material on the shape of the deposition profile is shown in Fig. 5.11 for sputtered Cu. The shape profile is similar to that of Al for a similar process conditions, though higher deposition rates (due to higher sputtering yield) are obtained especially for distances that are not too far from the target.

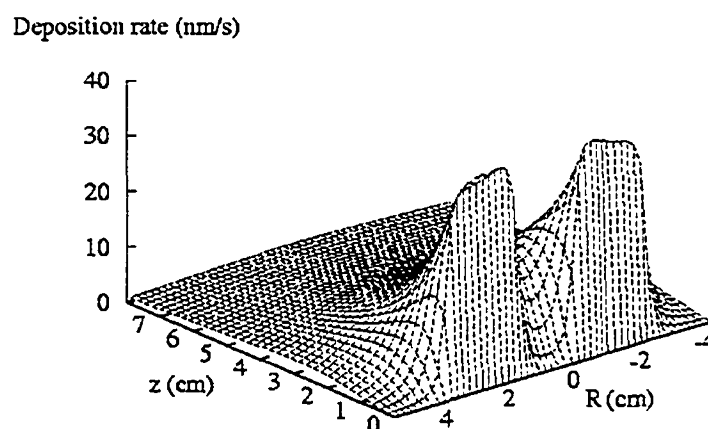

Fig. 5.11. Deposition profile sputtered Cu atoms at a magnetron power of 200 W, argon pressure of 15 mTorr. The inner and outer radii of the etch track are respectively 0.9 and 3.25 cm.

Reproduced with permission of the copyright owner. Further reproduction prohibited without permission.

Fig. 5.12 shows the effect of magnetron power on the deposition rate for the sputtering of aluminum and copper, respectively, at a pressure of 5 mTorr and a distance of 14 cm (system 2). Experimental data for Al at 5 and 10 mTorr, distance of (a) 10.8 and (b) 21 cm obtained using system 1 (Bob) alongside the model are presented in Fig. 5.13. Overall, the agreement between the model and experiment is good although the model may slightly underestimate the flux at low power. The deposition rate increases with power. The trend seems to suggest a non-linear dependence. This may be attributed to the reduction in the local density of the gas due to gas heating. The gas heating effect is much more significant at high powers than at low ones.

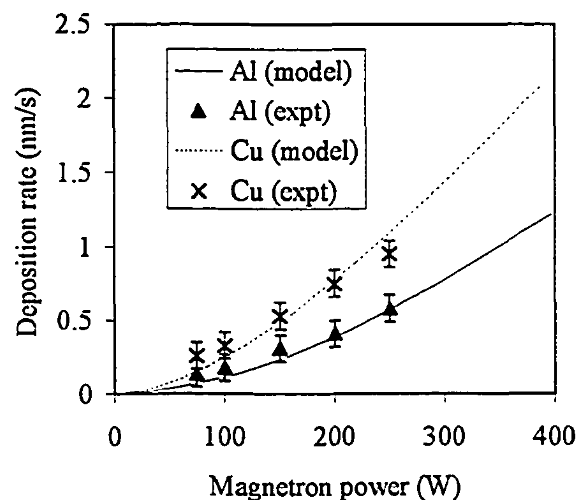

Fig. 5.12. On-axis deposition rate of Al and Cu as a function of magnetron power at a gas pressure of 5 mTorr and distance of 14 cm.

Reproduced with permission of the copyright owner. Further reproduction prohibited without permission.

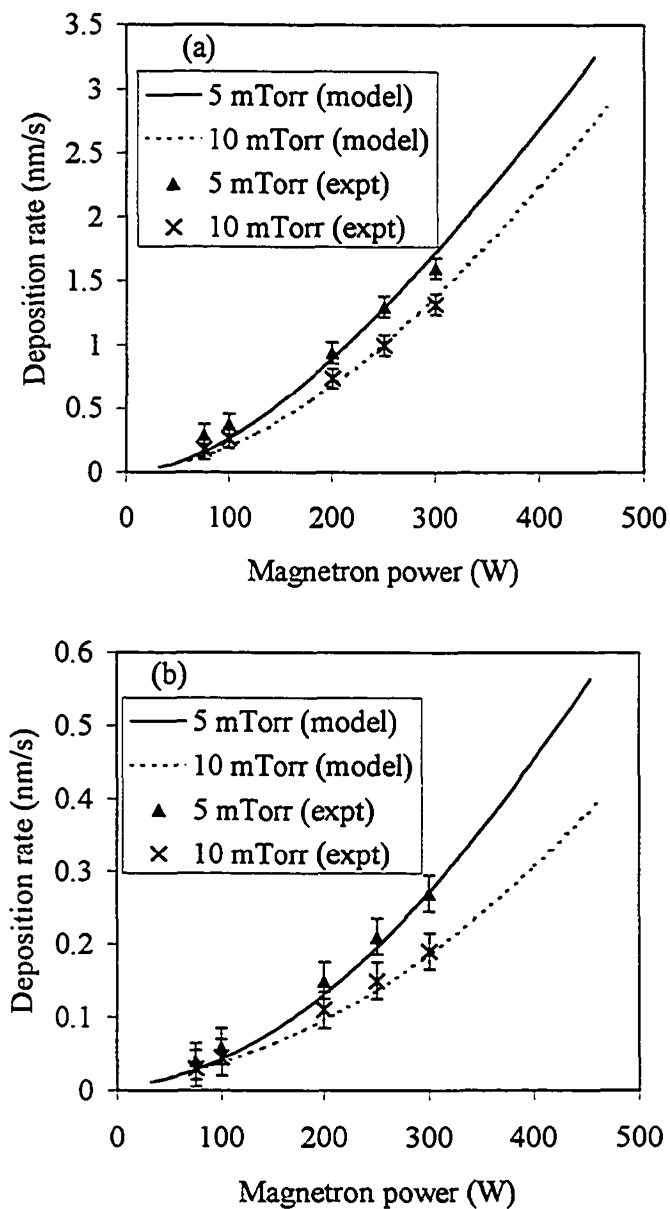

Fig. 5.13. On-axis deposition rate of Al as a function of magnetron power at a gas pressure of 5 and 10 mTorr, and distance of (a) 10.8 and (b) 21 cm.

Reproduced with permission of the copyright owner. Further reproduction prohibited without permission.

Fig. 5.14 shows the fraction of the diffused Al and Cu flux respectively, with respect to the total depositing flux as a function of the working gas (argon) pressure, for different powers at a distance of 10.8 cm. As expected, this fraction decreases with power, and depends on the pressure. This clearly shows the effect of the process parameters on the scattering effect of sputtered particles. At high pressure and low power, the depositing flux is dominated by the diffused flux, whereas, at low pressure and high power, it is dominated by the ballistic flux. The reduced effect observed with Cu in comparison with that of Al is attributed to the difference in the mass ratio between the sputtered particle and the gas. Al atoms in collision with Ar atom are scattered more than do Cu atoms. This results in a higher loss rate of the sputtered particles from the ballistic flux with increasing pressure. At high powers, the sputtered atoms are more energetic, and hence can persist in their original direction farther than they do at low powers.

Reproduced with permission of the copyright owner. Further reproduction prohibited without permission.

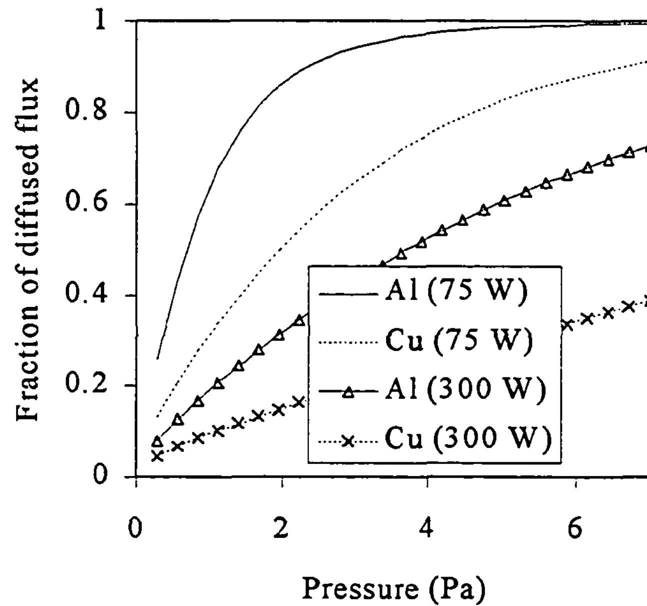

Fig. 5.14. Fraction of diffused flux of Al and Cu atoms at the substrate distance of 10.8 cm as a function of pressure and magnetron power.

5.2 Energy Model

The total energy per unit time, q_{tr}, transferred to the substrate is the product of the deposition flux and the total energy per deposited atom, which is obtained through a modified Thornton's model [127].

$$q_{tr} = \phi(U + E_k + E_r + E_p) + q_e + q_t \tag{5.21}$$

Reproduced with permission of the copyright owner. Further reproduction prohibited without permission.

Where U and E_k are the contributions of the heat of condensation and the average kinetic energy of the deposited atoms; E_r is the contribution of the reflected gas neutrals, which is dependent on the incident ion energy, E_0, and energy reflection coefficient, R_E; E_P is the contribution of the plasma radiation from the excitation and ionization events, and q_e and q_t are respectively the contributions of the electrons and the thermal radiation.

The contribution of the sputtered particles to the total deposited energy is mainly from its potential energy (condensation) and kinetic energy. The condensation energy, U per atom of aluminum and copper are respectively 3.33 and 3.5 eV [129]. The average kinetic energy of the ejected atoms was determined using Eq. (2.3), but with a correction factor as detailed in ref [88]. The modification is necessary as the high-energy tail observed with high ion energies is usually found to drop off sharply with the low ion energies associated with magnetron sputtering. The final expression for the energy distribution which combines the Thompson distribution of Eq. (2.3), modified anisotropy correction, and cut off factor (which sets the distribution to vanish at $E = E_{max}$ is as follows [88]:

$$f(E)dE \propto E(E+U)^{-3+2m} \exp\left[-A\left(\frac{M_g\left(E\cos^{q_1}\vartheta+U\right)}{M_t E_i}\right)^{q_2}\right]\left(1-\frac{E+U}{\gamma E_i}\right)dE \tag{5.22}$$

where ϑ is the emission angle, $A = 13$, $q_2 = 0.55$ and $q_1 \approx 2 - M_t/4M_g$. The maximum recoil energy γE_i is sometimes taken be equal to (E_{max} + U). The parameter m, which depends on the species, was found to be generally between 0.20 and 0.23 [88]. From the

Reproduced with permission of the copyright owner. Further reproduction prohibited without permission.

semi-empirical relation of Eq. (5.22), the obtained kinetic energies of sputtered Al and Cu atoms as a function of the ion energy are shown in Fig. 5.15. In transport towards the substrate, this energy is degraded due to collisions with the gas, as expressed in Eq. (2.9). For a given gas temperature, the mean free path scales inversely with pressure. Hence, Eq. (2.9) can be rewritten as:

$$E_{kf} = E_{ki} \exp\left(-\frac{\sigma P d}{kT}\right) \tag{5.23}$$

Where σ is the collision cross-section for exchange of momentum. As expressed in Eq. (2.22), σ/kT was estimated as 0.12, for which the gas temperature was assumed constant.

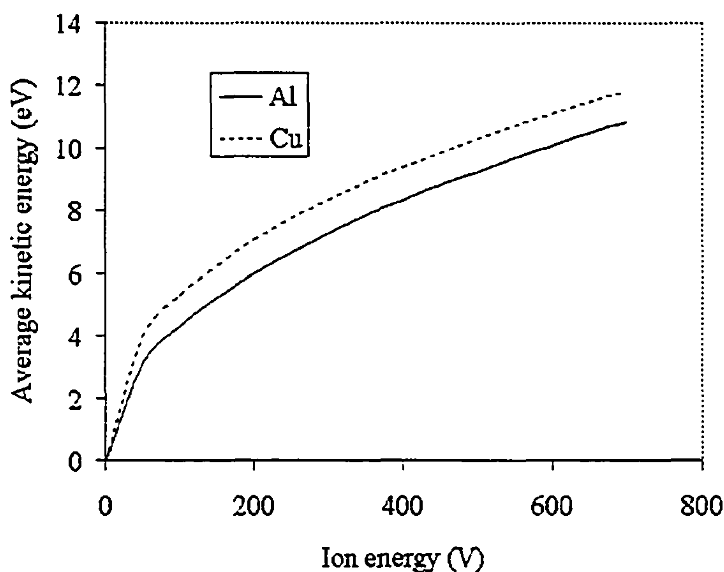

Fig. 5.15 Average energy of Al and Cu atoms sputtered normally to the surface as a function of the argon ion energy obtained from the semi-empirical model of Eq. (5.16) [88].

Reproduced with permission of the copyright owner. Further reproduction prohibited without permission.

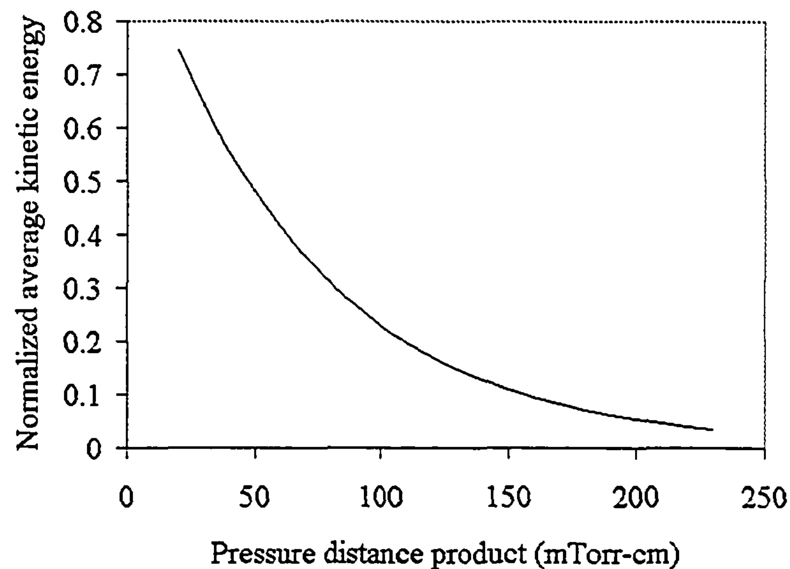

Fig. 5.16 Scaled dependence of the average kinetic energy of sputtered Al atoms as a function of pressure-distance product.

However, it is known that gas temperature does vary because of gas heating by the energetic sputtered particles and other processes. The extent of gas heating depends on the discharge current and, hence on magnetron power. Using the concept of gas heating, the dependence of the average kinetic energy on pressure distance product, *Pd*, is obtained by scaling the gas temperature, T, with the gas heating effect of discharge current, as expressed in Eq. (5.5). This is plotted as the solid line in Fig. 5.15.

Reproduced with permission of the copyright owner. Further reproduction prohibited without permission.

The contribution of the plasma radiation is due to the radiation emitted as a result of ionization and excitation events. This radiation is the difference between the average energy required by an electron to make an ion and the ionization energy of the gas atom. For an event involving an electron and argon atom, this energy is roughly estimated to be about 5.33 eV and can be emitted in either the forward or reverse direction [129]. In terms of the energy per sputtered atom, this energy is normalized to the sputtering yield as

$$E_{PS} = 5.33eV / Y_s \tag{5.24}$$

which assumes every ion is collected at the cathode. However, the interest is in terms of the energy per deposited atom; therefore, E_{PS} is further normalized to the deposition efficiency [127] as:

$$E_P = E_{PS} / \alpha_{de} \tag{5.25}$$

Where α_{de} is the deposition efficiency (the ratio of the deposited flux to the emitted flux at the target). It depends on scattering events, and is determined by pressure and the distance of the substrate from the target. The dependence of the deposition efficiency on pressure is given in Eq. (2.24) for a given substrate-target distance. However, it is usual to express this dependence in terms of the product of pressure and distance as:

$$\alpha_{de} = \alpha_{de0} \exp(-\gamma Pd) \tag{5.26}$$

Thus, E_P increases with pressure and distance. To clearly illustrate this dependence on pressure, SRIM-2000.39 [86] is used to obtain the sputtering yield at a discharge voltage

Reproduced with permission of the copyright owner. Further reproduction prohibited without permission.

of 415 V for an aluminum target as $Y_s = 0.58$ atoms/ion. Thus, for a gas pressure of 5 and 10 mTorr, and substrate-target distance of 10.8 cm, an estimated contribution of 13 and 18 eV respectively from plasma radiation is obtained per deposited atom.

The contribution of the energy of the reflected neutrals to the total deposited energy depends on the mass ratio of the target material to that of the incident ion. Both the energy and particle reflection coefficients have been shown to increase with the mass of the target material for a given gas. In ref. [176] it was reported that the reflection coefficients decrease monotonically with increase in the incident energy, since the probability for backscattering decreases with the penetration depth. However, above 400 eV, the differences in values for different energies are small, and the coefficients may be assumed constant with energy. The functional dependence of the energy reflection coefficient on the target voltage, V_T, within the range of study [176] is given by:

$$R_E = 1 - \left(\frac{V_T}{V_E}\right)^{\varepsilon} \tag{5.27}$$

where V_E is a fitting parameter, which was found to be around 20000 V for the heavy elements, but lower for the lighter ones. The power ε was found to be around 0.006 for germanium and to increase to about 0.037 for tungsten. The initial energy of the reflected neutral is equal to the product of the ion energy and the reflection coefficient. Because of

Reproduced with permission of the copyright owner. Further reproduction prohibited without permission.

collisions with the gas, the deposited energy of the reflected neutrals decays exponentially with pressure-distance product as:

$$E_r = \frac{R_E E_0}{Y_s}\exp(-\alpha_r Pd) = \frac{R_E E_0}{Y_s}\exp\left(-\frac{\sigma_r Pd}{kT}\right) \tag{5.28}$$

Since this energy contribution is scaled with the ejected atoms at the target, and the interest is in terms of the deposited atoms at the substrate, it would be necessary to factor Eq. (5.28) by the deposition efficiency of Eq. (5.26).

Substrate bias is a significant factor in determining the contribution of ions and electrons to the total energy deposited onto the growing film [214]. At a substrate bias potential equal to or greater than 0 V, ions contribute an insignificant energy to the growing film, whereas electrons contribute significantly to the total energy [127,130]. The energy contribution of electrons depends on the electron temperature, kT_e, and density, n_e as well as the substrate bias potential, V_{sub} relative to the plasma potential, V_P. For a Maxwellian energy distribution, the energy flux of electrons is given by [151,214]:

$$E_e = 2kT_e n_e\left(\frac{kT_e}{2\pi m_e}\right)^{0.5}\exp\left(-\frac{e(V_P - V_{sub})}{kT_e}\right); \qquad V_P > V_{sub} \tag{5.29}$$

The electron density in the substrate region is proportional to the discharge power [135], and for a given power depends on the pressure. The spatial distribution of electron density is highly influenced by the pattern of the magnetic field. This density is

Reproduced with permission of the copyright owner. Further reproduction prohibited without permission.

significantly higher above the target etch tracks than along the central axis at those regions close to the target [215]. However, at large distances the distribution tends to flatten out. Generally, the shape profile of the spatial distribution of electrons is similar to those of the deposition rate. Electron temperature depends on the gas-target combinations and discharge voltage. For a given experimental system, the dependence of electron temperature on the discharge voltage V_d is given by [152]:

$$kT_e = \upsilon V_d^2 \tag{5.30}$$

Where, υ is constant for a given gas-target combination, magnetic field and system geometry. At constant power operation, the discharge voltage decreases with gas pressure, hence the electron temperature would decrease with pressure. From Langmuir probe measurements, the electron temperature and density for Al at a gas pressure of 5 mTorr, substrate-target distance of 10.8 cm and magnetron power of 200 W were estimated to about 2.4 eV and 2.4 x 10^9 cm^{-3} respectively.

Measurement of the temperature of the shield around the target for the magnetron sputtering system used for this study shows that a weak thermal link exists between the shield and the water-cooling system. Thus the shield heats up, resulting in a significant heat transfer to the substrate by thermal radiation. The thermal radiant flux, q_t, from the shield toward the substrate region was determined using Eq. (2.19). Fig. 5.17 shows the variation in shield temperature with time for both the experimental measurement and the

Reproduced with permission of the copyright owner. Further reproduction prohibited without permission.

data from a thermal model of the chamber of radius 24 cm at a magnetron power of 200 W and gas pressure of 5 mTorr during the sputtering of Al. The shield temperature was modeled using Eqs. (2.19) and (3.2), by considering that almost all the incident energy is converted into heat and the main sources of heat lost from the shield are by thermal conduction through the gas as well as through the shield material to the cooling surface and radiation. The energy source to the shield is mainly from the system input power. Thus, the shield steady state temperature is expected to increase with magnetron power. The emissivity used was found to be different from the bulk emissivity for steel. A value of 0.79 was used, which is higher than the bulk value. This value is close to the value for oxidized steel [205]. There has been evidence that the surface emissivity of material does change with temperature and surface roughness [169,196,216,217]. For example, Love [216], cites an increase in emissivity for chromium steel from about 0.2 at 600 °C to over 0.7 at 900 °C. Simonsen [217] gave values for the emissivity of steel at 100 °C ranging from 0.066 to 0.97, depending on whether the surface is polished or rough. In the magnetron sputtering system, the ground shield around the target is always subjected to bombardment by energetic particles, and hence its surface is rough. At a magnetron power of 200 W, the contribution of thermal radiation to the deposited energy during the sputter deposition of Al was estimated to be about 11 % of the total energy [127] (shown in section 4.3.3).

Reproduced with permission of the copyright owner. Further reproduction prohibited without permission.

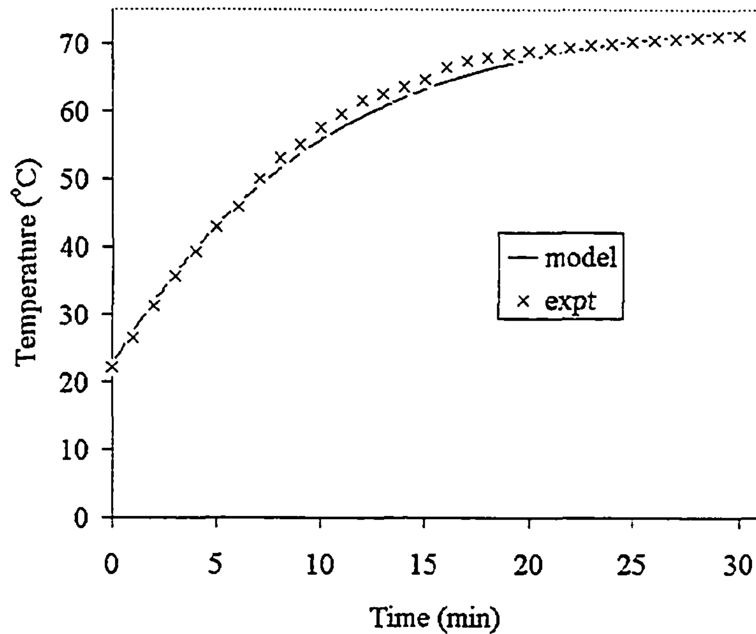

Fig. 5.17. Comparison of the model with the measured temperature of the shield around a 7.5 cm planar target located in the magnetron sputter chamber of radius 24 cm during the sputtering of Al at a magnetron power of 200 W and gas pressure of 5 mTorr.

An energy model is thus obtained by using the above details in Eq. (5.21). The next sections will discuss the results of the energy model obtained. As a test of the validity of the model, its results are compared to the experimental ones.

Reproduced with permission of the copyright owner. Further reproduction prohibited without permission.

5.2.1 Total Energy at the Substrate

The steady state total energy deposited as a function of the magnetron discharge powers for gas pressures of 5 and 10 mTorr at substrate-target distances of 10.8 cm and 21 cm are shown in Figs. 5.18 and 5.19 for Al and Cu respectively. The model results compare well with the experimental values, although there is limited data for copper. The deposited energy increases with power as expected, with a trend that seems to suggest a non-linear dependence. Any apparent deviation from linear dependence may be attributed to the gas heating effect. Gas heating which results in the reduction of the local density, causes increases in the free path of the sputtered atoms, reflected neutrals and electrons. This results in the deposition of greater energy at the substrate.

Reproduced with permission of the copyright owner. Further reproduction prohibited without permission.

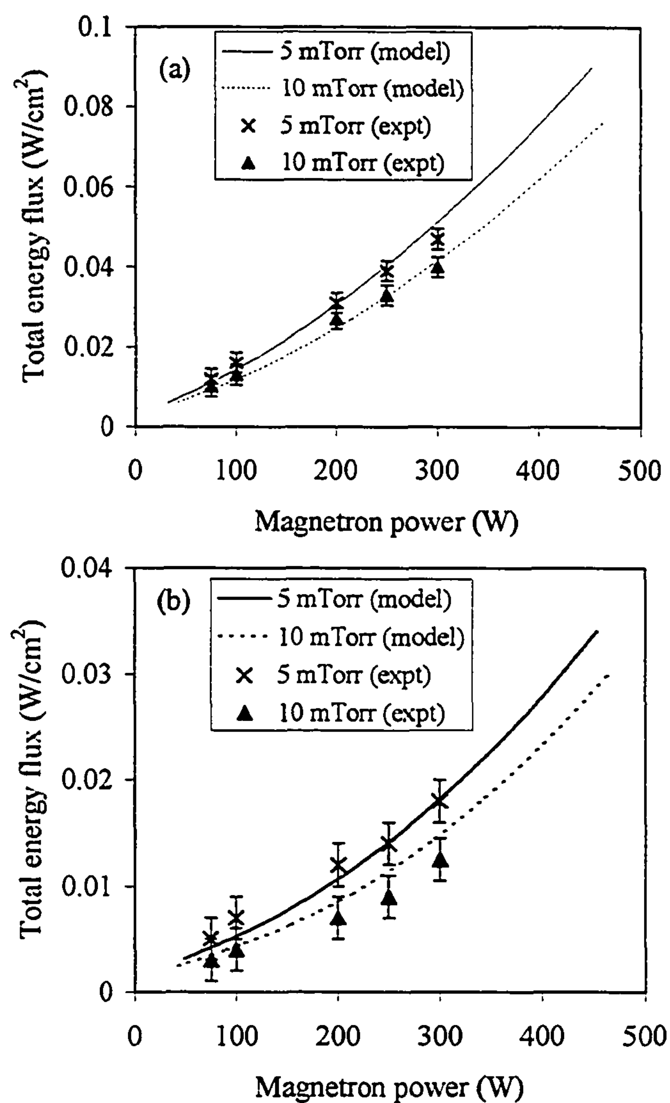

Fig. 5.18 Steady state energy as a function of magnetron power at substrate-target distances of (a) 10.8 and (b) 21 cm during the sputter deposition of Al at 5 and 10 mTorr.

Reproduced with permission of the copyright owner. Further reproduction prohibited without permission.

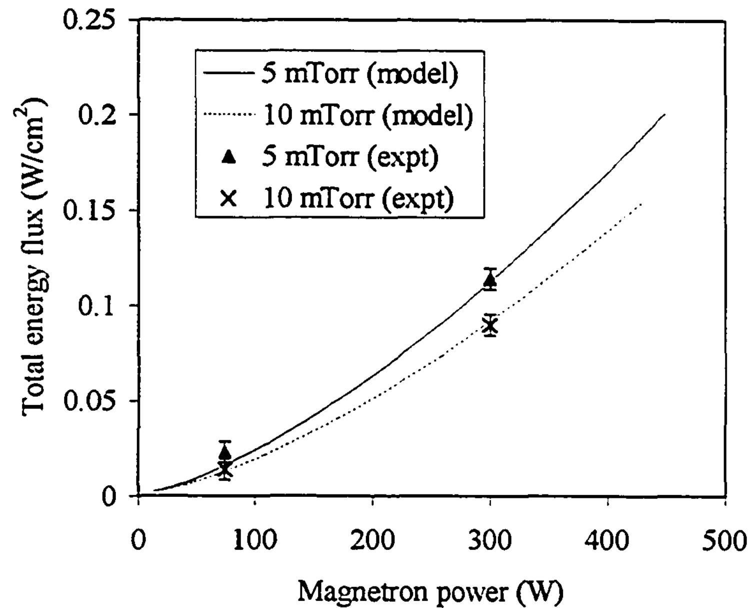

Fig. 5.19 Steady state energy as a function of magnetron power at substrate-target distances of 10.8 cm during the sputter deposition of Cu at 5 and 10 mTorr.

Fig. 5.20 shows the on-axis total energy plotted with distance for Al at 5 mTorr and for three different magnetron discharge powers. The deposited energy follows the pattern of particle deposition. As expected, the energy rises with distance to a maximum at some point close to the target, thereafter, it falls off. The trend of the fall is steep initially, then levelling off afterwards. This compares well with experimental results found elsewhere [151]. At long distances, most of the sputtered atoms are thermalized after involving in several collisions with the background gas. Thus the energy contribution of the sputtered atoms to the total deposited energy is greatly reduced to just about their condensation

Reproduced with permission of the copyright owner. Further reproduction prohibited without permission.

energy. In addition to the reduction in the energy of the sputtered atom, the flux of the sputtered atoms is also reduced due to scattering. The contribution of electrons is equally believed to fall at the substrate as a result of electron cooling and scattering due to the large *Pd* involved.

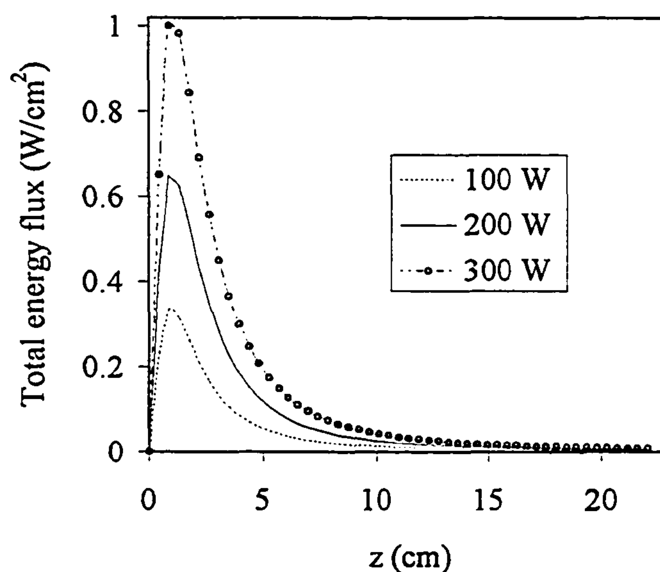

Fig. 5.20 Variation in the total energy flux at the substrate with substrate-target distance, *z* as a function of magnetron power at a gas pressure of 5 mTorr during the sputter deposition of Al.

Reproduced with permission of the copyright owner. Further reproduction prohibited without permission.

5.2.2 Total Energy per Deposited Atom

The total energy per deposited atom as a function of discharge power and pressure is shown in Fig. 5.21 (a) and (b) for Al and Cu respectively. Both the experimental values and the model show similar trends, although the model may overestimate the energies at very low powers by underestimating the deposition rate (especially for Al). In the low power regime, there is a rapid fall in the energy per deposited atom with powers. At high powers the energy per atom is essentially constant, and independent of both power and pressure. Fig. 5.22 (a) and (b) show the energy per deposited Al atom at various locations within the chamber at gas pressure of 5 mTorr and power density of 9.5 W/cm^2 for etch tracks of radii 0.9 and 3.25 cm, and 3.15 and 7.0 cm respectively. As noted in the figure, for those locations where uniform film over a large area is obtained, the energy per deposited atom is constant with substrate distance. This is the region where substrates would be located in most industrial applications where high deposition rate and film uniformity is highly desirable. Outside this region, the energy per deposited atom increases with distance. The effect of pressure, as seen in Fig. 5.21 is noticed mostly in the low power regime, where the energy per deposited atom is found to increase with pressure, probably due to reduced sputtered flux arriving at the substrate.

Reproduced with permission of the copyright owner. Further reproduction prohibited without permission.

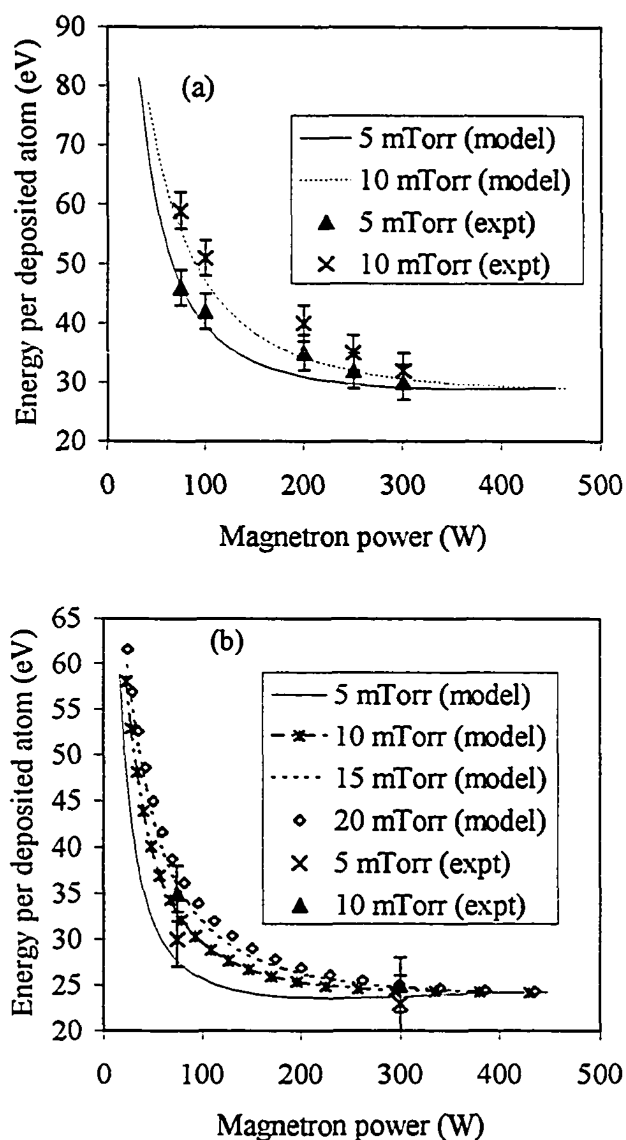

Fig. 5.21 Total energy per deposited (a) Al atom and (b) Cu atom as a function of power at distance of 10.8 cm for different pressures.

Reproduced with permission of the copyright owner. Further reproduction prohibited without permission.

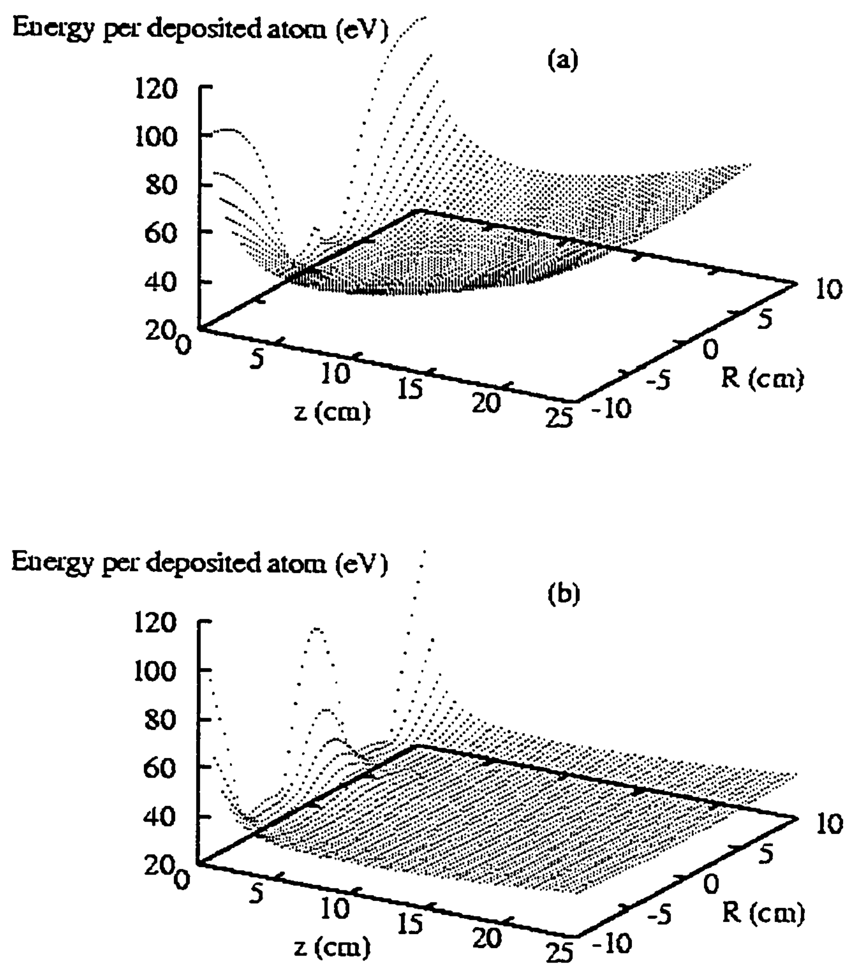

Fig. 5.22 The effect of the size of target and etch track on the energy per deposited atom (a) NT and (b) LT.

Reproduced with permission of the copyright owner. Further reproduction prohibited without permission.

The effect of target size and etch track size on the energy per deposited atom is shown in Fig. 5.22. Increase in the size of the inner radius of the etch track as well as the target size results in a shift in the regions of uniform film away from the target. As noticed in (b), this shift results in a lower energy per deposited atom compared with those of the smaller target (a) over the same area. However, the calculated energy per deposited atom at regions of uniform film is about the same for both cases under the same power density and other operating conditions. For Al and Cu, this energy is about 28 and 25 eV/atom respectively, given a d.c. planar magnetron considered in this study and limits of uncertainty.

Thornton [129] had proposed a pressure and power independent energy per atom. The results here tend to confirm that trend at high discharge powers, though the values of these energies per atom are higher than his values (13 and 17 eV for argon sputtering with cylindrical-post magnetrons). This is because of the modification to his model to include the contributions of electrons and thermal radiation as well as the computation of the plasma radiation per deposited atom instead of the atoms sputtered at the target. However, for a hollow cathode, Thornton [129] obtained about 40 eV/atom for both Cu and Al, and attributed the much higher value to plasma bombardment of the substrate. This is herein taken to imply the contributions of the charged particles (electrons and ions). For an unbiased substrate, ions have been shown to contribute an insignificant

Reproduced with permission of the copyright owner. Further reproduction prohibited without permission.

energy deposited onto the substrate [127,130], thus the extra energy he observed may be from electrons. At low powers, the trend of the results here is similar to those of Drusedau, *et al* [176], in which case, they obtained an increase in the energy per deposited atom with pressure, but a decrease with power.

The decrease in energy per atom with power may be attributed to the greater than linear increase in the deposition rate and gas heating effect. Both the energy flux and the deposition rate increase with power. However, not all the factors contributing to the total energy flux increase with power at the same rate as the flux of the depositing atoms. For instance, the plasma contribution increases with gas density. At high power, the rate of gas heating is high, and hence the density is reduced. Gas density reduction also causes an increase in deposition efficiency through reduced gas scattering. At low powers and high pressures, the probability of the sputtered atom depositing onto the substrate is greatly reduced, and the plasma radiation contribution is high since it increases with pressure.

To better understand the role of the individual contributions to the total energy per deposited atom, the effect of the process parameters on the individual contributions is shown in Figs. 5.23 and 5.24 for Al and Cu respectively. The trend of the results suggests that the plasma effects (electrons and plasma irradiation) are more important at lower

Reproduced with permission of the copyright owner. Further reproduction prohibited without permission.

power levels, especially for Al because of its low sputtering yield. The contribution of the sputtered atom increases with power but decreases with pressure as would be expected. In the low power regime, the contribution of electrons decreases rapidly with power, but at high powers, it is nearly constant with power. That of the plasma irradiation has a similar trend to that of the electron, though the initial decrease is not as rapid as that of the electron. Both contributions increase with pressure. At about 300 W and 5 mTorr, both electrons and plasma irradiation contribute about 30% each to the total energy per deposited Al atom. This percentage contribution changes with pressure and power. In obtaining the above, it was assumed that all incident energy at the substrate is absorbed. However, in practical context, some of the radiant energy, as already pointed out in section 4.3.3, may be reflected away from the surface, though some through multiple reflections may be deposited onto the substrate. This might limit the contribution of say the plasma radiation. The overall error is estimated to be in the order of 10%. Tables 5.1 and 5.2 show the percentage contributions at 100 and 300 W, 5 and 10 mTorr, and a substrate-target distance of 10.8 cm for Al and Cu respectively.

Reproduced with permission of the copyright owner. Further reproduction prohibited without permission.

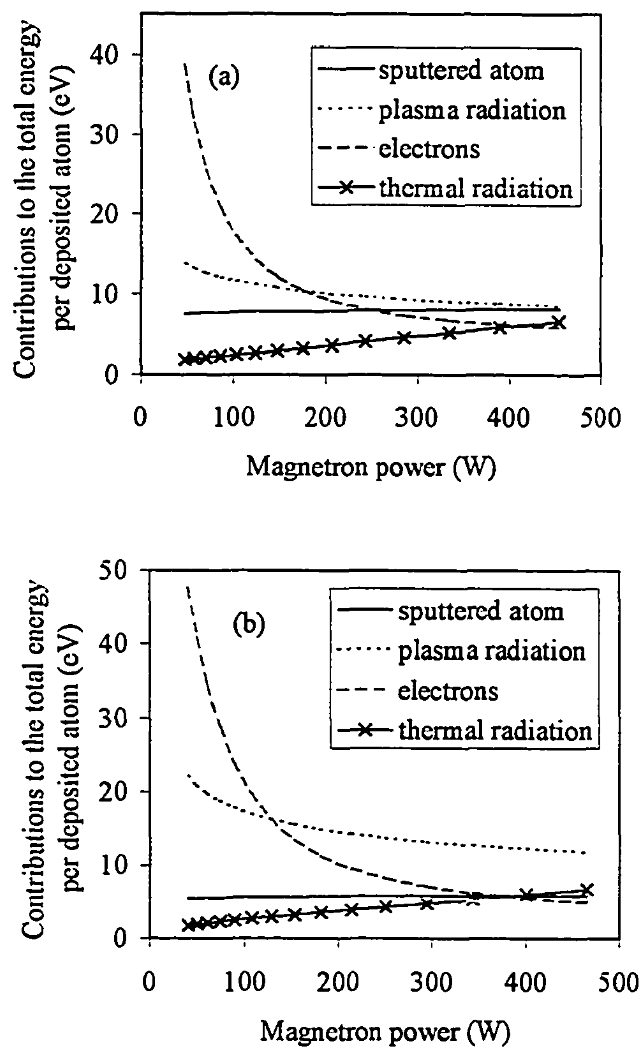

Fig. 5.23 Individual contributions to the total energy per deposited Al atom as a function of magnetron power at a substrate-target distance, z of 10.8 cm and gas pressure of (a) 5 and (b) 10 mTorr.

Reproduced with permission of the copyright owner. Further reproduction prohibited without permission.

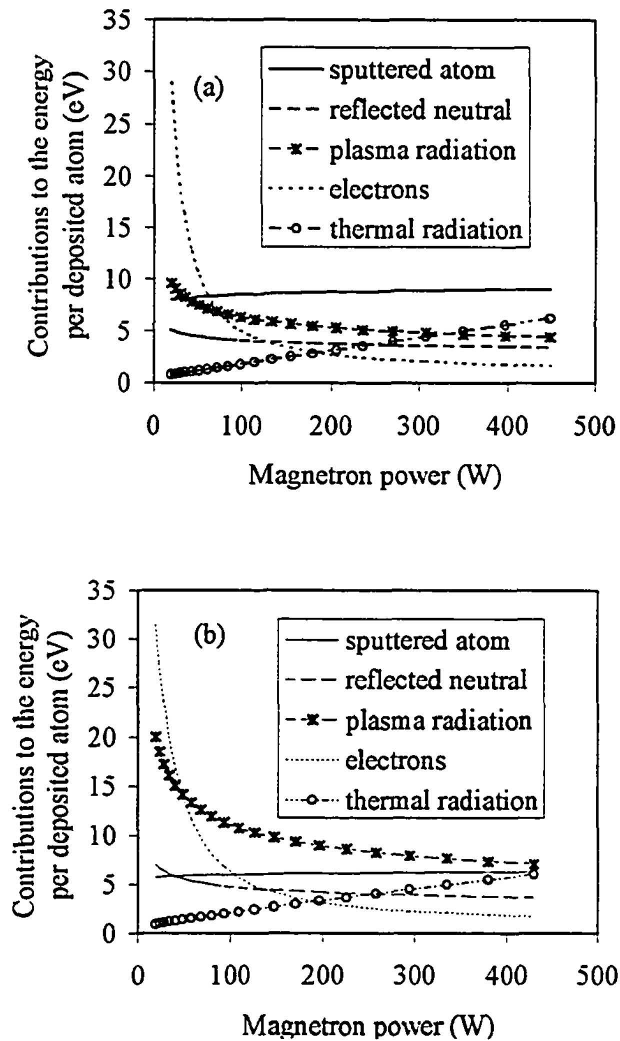

Fig. 5.24 Individual contributions to the total energy per deposited Cu atom as a function of magnetron power at a substrate-target distance of 10.8 cm and gas pressure of (a) 5 and (b) 10 mTorr.

Reproduced with permission of the copyright owner. Further reproduction prohibited without permission.

Table 5.1 Percentage contribution of the individual factors to the total energy per deposited aluminum atom at a substrate-target distance of 10.8 cm, magnetron power of 100 and 300 W, and gas pressure of 5 and 10 mTorr.

Factors	Percentage contribution 100 W		Percentage contribution 300 W	
	5 mTorr (%)	10 mTorr (%)	5 mTorr (%)	10 mTorr (%)
Sputtered atom	19.7	12.1	28.1	18.7
Plasma radiation	29.8	37.3	32.2	42.7
Electrons	44.1	45.0	22.4	22.9
Thermal radiation	6.4	5.6	17.3	15.7
Total	100	100	100	100

Reproduced with permission of the copyright owner. Further reproduction prohibited without permission.

Table 5.2 Percentage contribution of the individual factors to the total energy per deposited copper atom at a substrate-target distance of 10.8 cm, magnetron power of 100 and 300 W, and gas pressure of 5 and 10 mTorr.

Factors	Percentage contribution 100 W		Percentage contribution 300 W	
	5 mTorr (%)	10 mTorr (%)	5 mTorr (%)	10 mTorr (%)
Sputtered atom	33.2	20.0	37.4	24.9
Reflected neutrals	15.7	16.2	14.9	15.7
Plasma radiation	24.5	36.8	20.4	31.1
Electrons	19.6	20.0	8.8	10.0
Thermal radiation	7.0	7.0	18.5	18.3
Total	100	100	100	100

Reproduced with permission of the copyright owner. Further reproduction prohibited without permission.

Chapter 6

Numerical Simulation of Gas Heating

The volume in front of the target in a magnetron sputtering discharge is always in a state of bombardment by energetic particles. This mechanism may result in pressure differentials and/or gas heating [63,170]. Sputtered particles, as a result of their mean free paths compared to those of other energetic particles, have been thought to be the main source of the gas heating [63]. However, depending on pressure and other process conditions, reflected neutrals and charged particles may contribute significantly to the gas heating. Thus, the purpose of the numerical simulation of gas heating, in this context, is to obtain a temperature profile of gas temperature within the sputtering chamber for a magnetron sputtering system with argon as the background gas. Since the heating of the gas is mainly due to energy deposited into the gas from collision events, gas pressure would be assumed to have a considerable effect on the temperature profile.

Reproduced with permission of the copyright owner. Further reproduction prohibited without permission.

6.1 Numerical Model

The energy lost to the gas from the collision events is used in part to raise the temperature of the gas, which in turn is transferred from the gas to the ambient, through the chamber walls. In section 2.5, it was shown that the dominant mode of heat transfer, given the low gas pressure, is by conduction. Thus, the transient energy balance equation is:

$$q_{in} = C\frac{dT_b}{dt} - \frac{\kappa A(T_b - T_a)}{l_{ab}} \tag{6.1}$$

$$C = \rho c V \tag{6.2}$$

where C is the thermal capacity, V is the volume element b, c is the specific heat capacity, ρ is the density, T_b is the gas temperature, T_b-T_a is the difference in temperature between point a and b, l_{ab} is the separation of a and b, A is the contact area, q_{in} is the power input and κ is the thermal conductivity of gas.

In solving Eq. (6.1), the following assumptions are made:

(a) Since the power input q_{in} is from the collision events between the gas and energetic particles, it depends on the probability of collision.

Reproduced with permission of the copyright owner. Further reproduction prohibited without permission.

(b) The sources for the power input are from the collisions between gas and (a) sputtered particles, (b) reflected neutrals, (c) electrons and (d) ions. Here radiation is ignored due the low absorptivity of the gas.

(c) Within the walls of the chamber, $q_{in} = 0$.

(d) Outside the chamber, $dT = 0$, and $q_{in} = 0$.

(e) Heat transfer occurs at the boundary between the steel surface and the gas.

(f) The volume may be divided into "lumps" (cubes) centred on the nodal points. With this, the Finite Difference Method (FDM) [153,218,219] can be used in solving for the spatial temperature profile.

(g) The medium between two nodal points can be represented by an element of thermal resistance, ***r***. The heat storage capability of each node is represented by the thermal capacity, C of the cube connected between the node and the "ground" [153] (see Fig. 6.1). This forms an r-C network similar to the Transmission Line Matrix or Method (TLM) described elsewhere [220–226].

(h) The thermal resistance for heat transport by conduction, for instance, r_y between a and d is given by: $r_y = \frac{dy}{\kappa dx dz}$, where *dx*, *dy* and *dz* are the respective length of the "lump". The thermal resistance for heat

Reproduced with permission of the copyright owner. Further reproduction prohibited without permission.

transfer between the wall and the gas, $r_c = \frac{1}{hdxdy}$, h is the heat transfer coefficient between the steel surface and the gas.

(i) The thermal conductivity of the gas increases linearly with temperature.

(j) The average gas pressure within the chamber is constant.

(k) The thermal mass is directly related to the gas pressure but depends inversely on temperature.

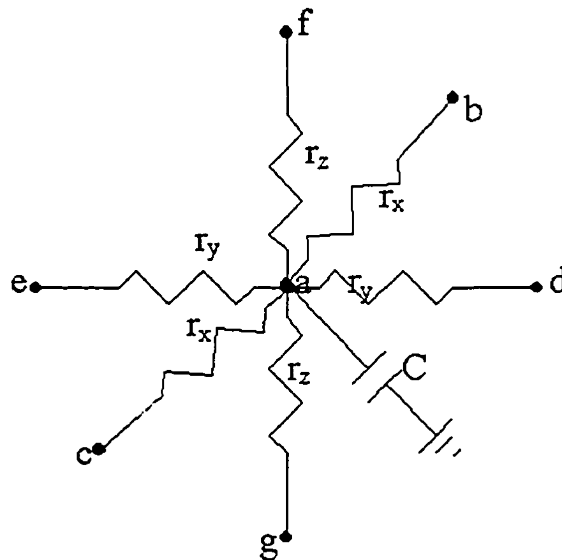

Fig. 6.1 Three-dimensional nodal r-C network constructed for a nodal centre a, of a cube with six neighbouring nodal centres (b-g). The thermal capacity of the cube is represented by C, which is connected to the ground.

Reproduced with permission of the copyright owner. Further reproduction prohibited without permission.

By applying the time-domain FDM, Eq. (6.1) may be re-written in 3D using the forward difference representation for each node as:

$$q_{in} = C\frac{dT}{dt} - \frac{\kappa dydz(T_a - T_b)}{dx} - \frac{\kappa dydz(T_a - T_c)}{dx} - \frac{\kappa dxdz(T_a - T_d)}{dy}$$
$$- \frac{\kappa dxdz(T_a - T_e)}{dy} - \frac{\kappa dxdy(T_a - T_f)}{dz} - \frac{\kappa dxdy(T_a - T_g)}{dz} \quad (6.3)$$

where $\frac{dT}{dt} = \frac{(T(a,t+dt) - T(a,t))}{dt}$, $C = \frac{cPMdxdydz}{kTN_A}$, M is the molecular mass of the material, k is the Boltzmann constant and N_A is the Avogadro constant.

If the energy transfer function for each energetic particle in collision with the gas is H, then energy lost to the gas is:

$$dE = -Hd\rho \quad (6.4)$$

where $d\rho = \frac{xdx + ydy + zdz}{\rho}$

The energy transfer function is obtained for each particle depending on its initial energy as outlined in section 5.2. The total energy lost to the gas at each node is computed by summing all the energy lost by each particle, which is given by:

$$q_{in} = q_{sp} + q_m + q_e + q_i \quad (6.5)$$

Reproduced with permission of the copyright owner. Further reproduction prohibited without permission.

$$q_{sp} = \phi E_{ki} \frac{\sigma P}{kT} \exp\left(-\frac{\sigma P \rho}{kT}\right) d\rho \tag{6.6}$$

$$q_m = E_0 j R_E R_N \frac{\sigma_r P}{kT} \exp\left(-\frac{\sigma_r P \rho}{kT}\right) d\rho \tag{6.7}$$

$$q_e = n_e 2kT_e \left(\frac{kT_e}{2\pi m_e}\right)^{1/2} \exp\left(-\frac{V_{bias}}{kT_e}\right) \frac{\sigma_e P}{kT} \exp\left(-\frac{\sigma_e P \rho}{kT}\right) d\rho \tag{6.8}$$

$$q_i = 0.61 n_e V_{bias} \left(\frac{kT_e}{m_i}\right) \frac{\sigma_i P}{kT} \exp\left(-\frac{\sigma_i P \rho}{kT}\right) d\rho \tag{6.9}$$

where ϕ is the sputtered particle flux of Eq. (5.20), kT_e is the electron temperature, V_{bias} is the difference in potential between the plasma potential and the floating potential, n_e is the electron density (non-maxwellian electrons are excluded due to their low densities), R_E and R_N are respectively the energy and particle reflection coefficients of the neutral gas particles and E_0 is the energy of the incident ion on the target. The dependence of these parameters on the process conditions has been already expressed in chapter 5.

The temperature of each node is initialized to the room temperature (300 K). In each cell, the flux of sputtered atoms and reflected neutrals, and electron density are calculated, in order to determine the input power density. The change in temperature of each node is then calculated for each time step and the nodal temperature updated until the steady state temperature is reached.

Reproduced with permission of the copyright owner. Further reproduction prohibited without permission.

In order to ensure stability, it is usual to choose the time step (3-D) such that [153]:

$$dt \le \left(\frac{1}{6}\right) rC \tag{6.10}$$

The rC time constant for the gas is by far smaller than that of the steel material (chamber walls), hence it determines the time step required for the simulation. However, at the surface of the walls, heat is also transported by convection (due to the temperature jump). Thus, the effective thermal resistance of the boundary cells (3-D) is [153]:

$$r_{eff} = \frac{3r_c r}{3r_c + r} = r\left(\frac{1}{1 + (1/3)(hdx/\kappa)}\right) \tag{6.11}$$

Since this is smaller than r, then the required time step for stability is thus:

$$dt \le \left(\frac{1}{6}\right)\frac{r_{eff}C}{n} \tag{6.12}$$

The constant, n is introduced as a scaling factor since some of the boundary cells may be smaller than the non-boundary cells. Here, from the size of the cell used, the value of n was generally found to be between 3 and 4.

6.2 Results and Discussions

It is expected that the maximum gas temperature would be dependent on the size of a cell (determined by the number of grids). The cylindrical chamber of external diameter of 49

Reproduced with permission of the copyright owner. Further reproduction prohibited without permission.

cm and of the same height is chosen for the simulation space. This may be divided into N^3 grids. Fig. 6.2 shows the effect of N on the maximum gas temperature for Cu sputtering at a gas pressure of 11.25 mTorr, with the substrate plane located at 5 cm above the target.

The temperature is observed to increase with the increase in N (decrease in *dx*). However, at N greater than 80, there was only a small change in temperature. Thus, the simulation space was divided into 100 x 100 x 100 grids.

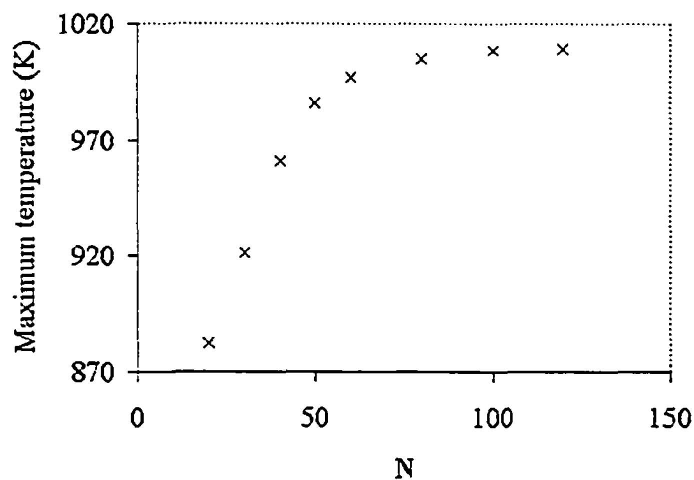

Fig. 6.2 Effect of grid size on the maximum gas temperature for the sputtering of Cu at 11.25 mTorr, magnetron power density of about 40 W/cm^2 and a substrate plane located at 5 cm above the target.

Reproduced with permission of the copyright owner. Further reproduction prohibited without permission.

The following treats the results in terms of the effect of the process conditions and materials on the spatial temperature profile.

6.2.1 Effect of Pressure

Figs. 6.3 and 6.4 show the simulation results of the longitudinal and transverse spatial gas temperature profiles respectively, for the dc magnetron sputtering of Al at argon gas pressure of (a) 7.5, (b) 11.25, (c) 20 and (d) 30 mTorr, with a magnetron power density of about 40 W/cm^2, with the substrate plane located at 15 cm above the target. Similar results for the sputtering of Cu are shown in Figs. 6.5 and 6.6 respectively. The results show that the maximum gas temperature is pressure dependent. Gas temperature increases with pressure. The higher the pressure, the more localized is the heating space in front of the target. This is as would be expected since the source of the input power is related to pressure through gas collisions. The mean free path (which determines the number of collisions within a given space) of the particles relates inversely with pressure.

At low pressures, the particles have long mean free path and can reach far into the chamber space with significant energy. As the pressure increases, they lose much of their energy to the gas until they become thermalized. It is evident that most of the particles are already thermalized after traversing a short distance in the case of the 30 mTorr of

Reproduced with permission of the copyright owner. Further reproduction prohibited without permission.

pressure in contrast with the case of 7.5 mTorr. The location of region of maximum temperature tends to shift with pressure towards the target.

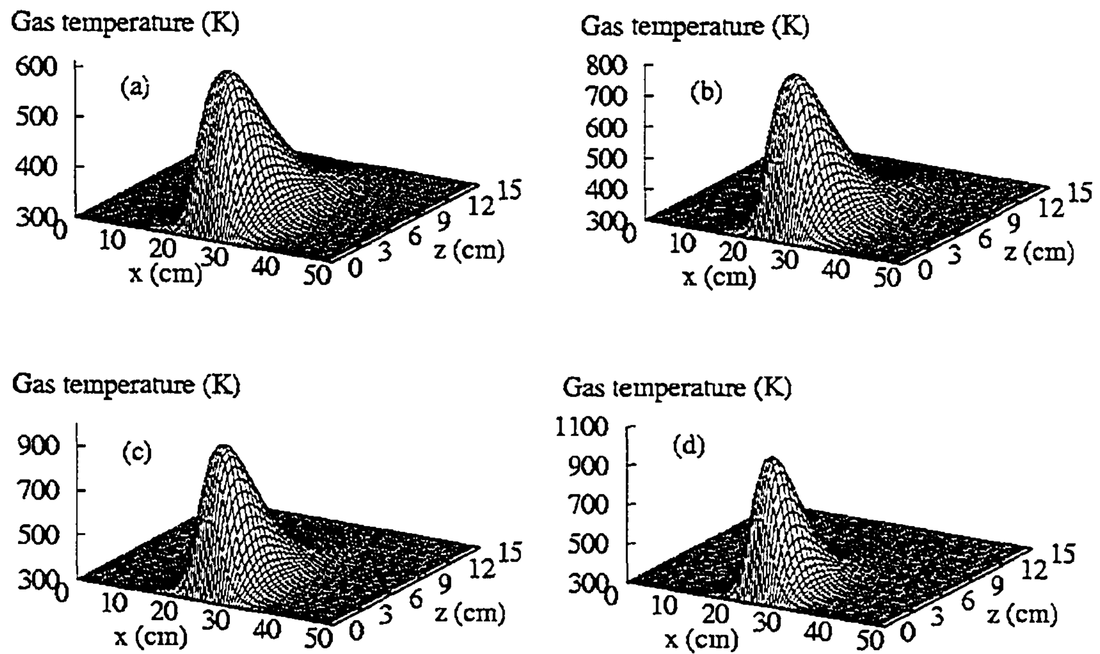

Fig. 6.3 Longitudinal gas temperature profile for the sputtering of Al at a magnetron power density of about 40 W/cm^2, pressure of (a) 7.5 (b) 11.25 (c) 20 and (d) 30 mTorr, with the substrate plane at 15 cm above the target.

Reproduced with permission of the copyright owner. Further reproduction prohibited without permission.

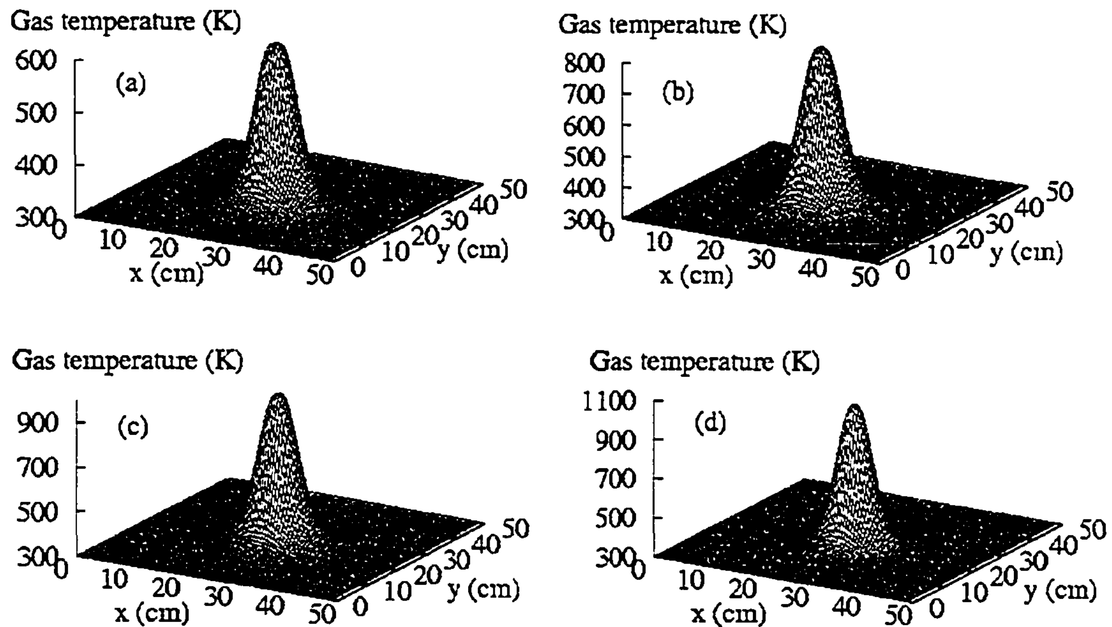

Fig. 6.4 Transverse gas temperature profile for the sputtering of Al at 1.96 cm above the target for a magnetron power density of about 40 W/cm^2, for pressures of (a) 7.5 (b) 11.25 (c) 20 and (d) 30 mTorr, with the substrate plane at 15 cm above the target.

The transverse profiles were taken at about 1.96 cm above the target. As observed in Figs. 6.4 and 6.6, details of the sputtered particles' deposition profile have some impact on the temperature profile close to the target. The extent of the effect from the target depends on the amount of scattering. For instance, for both Cu and Al, the spatial area of most heating (which of course depends on the size of target) reduces with pressure. Therefore, this might be attributed to the scattering effect of the sputtered particles. Thus,

Reproduced with permission of the copyright owner. Further reproduction prohibited without permission.

the higher the pressure, the more localized the heating space, and the more intense the heating. Of course the intensity of the heating depends also on the sputtering yield of the target material, as noticed in the case of Cu compared to that for Al.

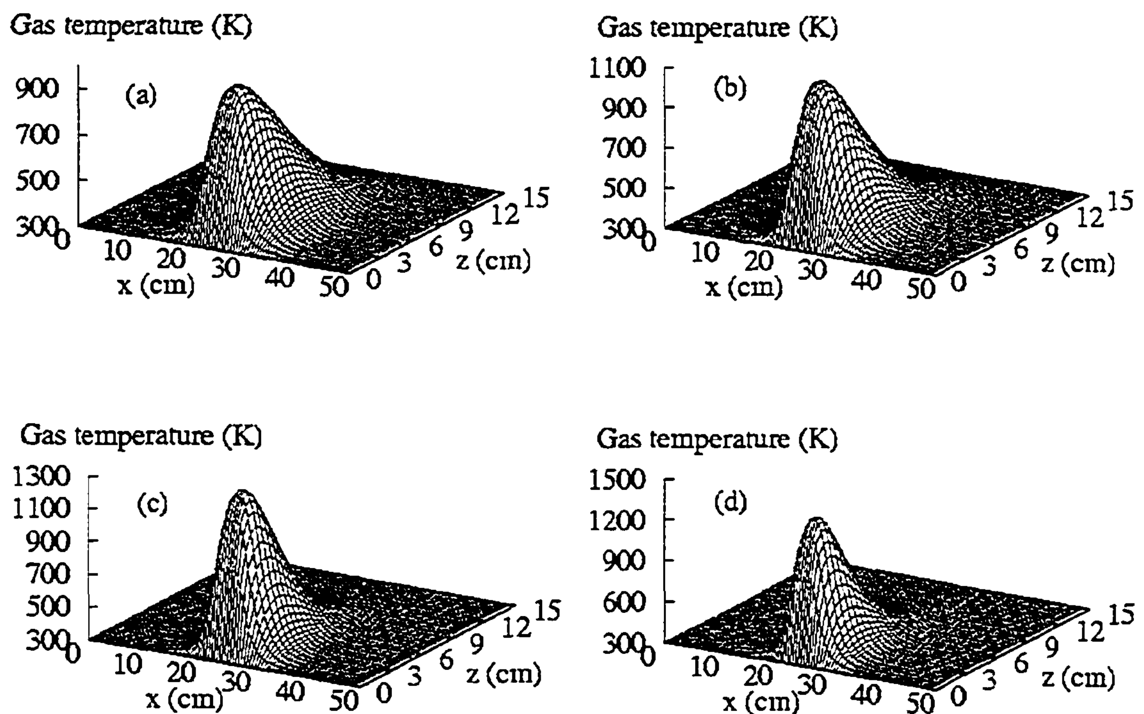

Fig. 6.5 Longitudinal gas temperature profile for the sputtering of Cu at a magnetron power density of about 40 W/cm^2, for pressures of (a) 7.5 (b) 11.25 (c) 20 and (d) 30 mTorr, with the substrate plane at 15 cm above the target.

Reproduced with permission of the copyright owner. Further reproduction prohibited without permission.

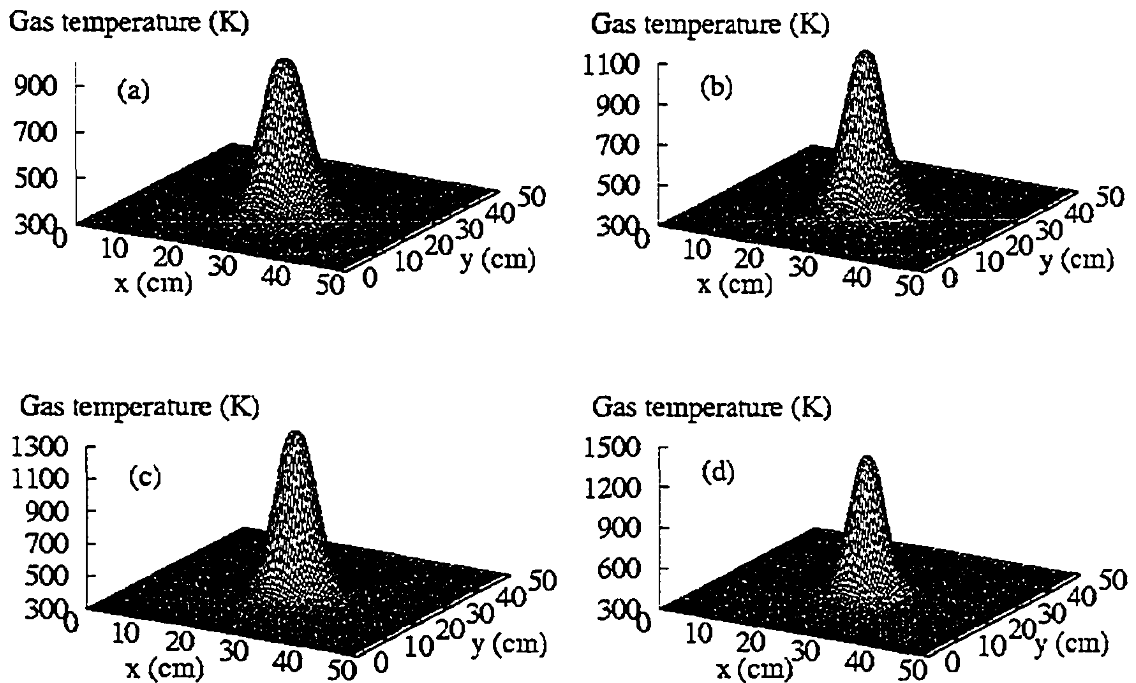

Fig. 6.6 Transverse gas temperature profile for the sputtering of Cu at 1.96 cm above the target for a magnetron power density of about 40 W/cm^2, for pressures of (a) 7.5 (b) 11.25 (c) 20 and (d) 30 mTorr, with the substrate plane at 15 cm above the target.

6.2.2 Effect of Target Material

There seems to be no significant difference in the relative shape of the temperature profile for Al and Cu. Though, as observed in the results for Al and Cu, for instance at 7.5 mTorr, Cu tends to show more of the thermalization effect than Al. However, Cu

Reproduced with permission of the copyright owner. Further reproduction prohibited without permission.

shows more of an absolute gas heating effect than Al, as the gas temperature in the case of Cu is consistently higher. These may be attributed to the fact that Cu has a higher energy transfer efficiency in collision with Ar than does Al. Also the sputtering yield of Cu is greater than that of Al, thus the flux of sputtered Cu would be higher than for Al under the same process conditions. Hence, the total energy transferred to the gas would be greater. Also, the mass ratio of Cu to argon is greater than that of Al to argon. Thus, it has a higher probability of energetic neutral gas reflection at the target than Al. These reflected neutrals in collision with the gas may also contribute some heating to the gas.

Since the effective gas pressure is assumed constant within the chamber, then the increase in gas temperature may be assumed to translate into gas density reduction (rarefaction). Thus, the relative gas density, *RD* may be obtained from the ratio of the room temperature to the temperature of the heated gas:

$$RD = \frac{300}{T(K)} \tag{6.13}$$

To attest to the validity of the results, the relative gas density is determined at the regions of maximum temperature and compared to the experimental results of ref [63], as shown in Table 6.1. The results compare favourably with the experiment results. Observed differences may be attributed to differences in terms of the system geometry for the two systems considered. It should be noted that the experimental data were obtained at a fixed distance of 5.32 cm from a 15 cm target, and might differ slightly from maximum values.

Reproduced with permission of the copyright owner. Further reproduction prohibited without permission.

Table 6.1 Comparison between simulated relative gas density and the experimental results of ref [63], for the sputtering of Al and Cu in argon gas at a magnetron power density of about 40 W/cm^2. The experimental data were obtained for a circular planar dc magnetron sputtering system, with a target diameter of 15 cm. The target voltages were typically between 300 and 700 V depending on the type of target material and gas used.

Pressure (mTorr)	Al		Cu	
	Simulation	Experiment	Simulation	Experiment
7.5	0.50	0.52	0.33	0.37
11.25	0.38	0.39	0.28	0.28
20	0.31	0.29	0.23	0.23
30	0.28	0.26	0.21	0.20

6.2.3 Effect of Substrate Plane Location

The location of the substrate plane above the target for a given pressure determines the ratio of the thermalized sputtered particles to the total sputtered particles that arrive at the substrate. The further away the substrate is from the target, the higher the ratio of thermalized particles. If the substrate plane were located very close to the target, then most of the particles would arrive at the substrate with their kinetic energies close to their ejected energies. The implication of this is that the particles would lose only a small

Reproduced with permission of the copyright owner. Further reproduction prohibited without permission.

amount of their energies to the background gas, and hence the gas temperature would not be very high. Therefore, it is expected that as the substrate plane is moved away from the target, more energy would be lost to the background gas. Thus, the gas temperature would increase with the distance of the substrate from the target. However, when most of the particles are thermalized, the maximum gas temperature would remain almost constant with the substrate-target distance, since no significant additional energy is added to the gas.

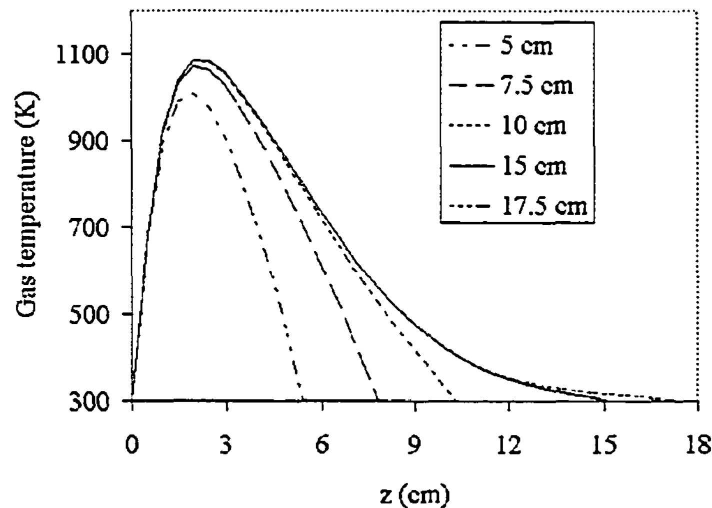

Fig. 6.7 Effect of the substrate plane location on the on axis gas temperature profile for the sputtering of Cu at magnetron power density of 40 W/cm^2 and pressure of 11.25 mTorr.

Reproduced with permission of the copyright owner. Further reproduction prohibited without permission.

Fig. 6.7 shows the on-axis temperature profile for the sputtering of Cu at a magnetron power density of 40 W/cm^2 and pressure of 11.25 mTorr for different distances of the substrate plane. The results show that maximum temperature increases with the distance of the substrate plane. Between the distance of 10 and 15 cm for this pressure, the difference in the gas temperature is very small. At distances 15 cm and above, the maximum temperature remains almost constant. Thus above 15 cm at a gas pressure of 11.25 mTorr, the kinetic energies of most of the depositing Cu atoms would be close to the thermal energies of the gas.

At short substrate plane distances from the target, the shape of the temperature profile is almost symmetrical between the target and the substrate plane. The symmetrical nature of the shape profile changes as the distance is increased, with the location of the peak temperature being closer to the target than the substrate plane. It is also observed that the peak location shifts slightly towards the substrate with increased in the distance of the substrate plane up to when most of the particles are thermalized.

Reproduced with permission of the copyright owner. Further reproduction prohibited without permission.

6.2.4 Effect of Gas type

The amount of heat transferred from the heated gas to the ambient depends on the thermal conductivity of the gas. Since different gases have different thermal conductivities, the higher the thermal conductivity of the gas, the greater the amount of heat that would be conducted away to the ambient, and hence the lower the maximum gas temperature. To observe the effect of the different gas on the gas heating, argon, neon and krypton were used respectively for the sputtering of Cu. The same process conditions were maintained in all cases. Fig. 6.8 shows the longitudinal temperature profile respectively for the sputtering of Cu at power density of 40 W/cm^2 with (a) argon, (b) neon and (c) krypton as the background gas. The substrate plane was located at 5 cm above the target.

The results clearly show the effect of thermal conductivity on the temperature distribution of the gas. Krypton with the least thermal conductivity shows the highest maximum gas temperature, while neon with the highest thermal conductivity shows the least maximum gas temperature. The results here are consistent with the experimental results of ref [63]. From the above results, it clear that the problem of gas heating is mainly that of heat conduction from the plasma region (local heat source) near the target through the gas to the chamber walls.

Reproduced with permission of the copyright owner. Further reproduction prohibited without permission.

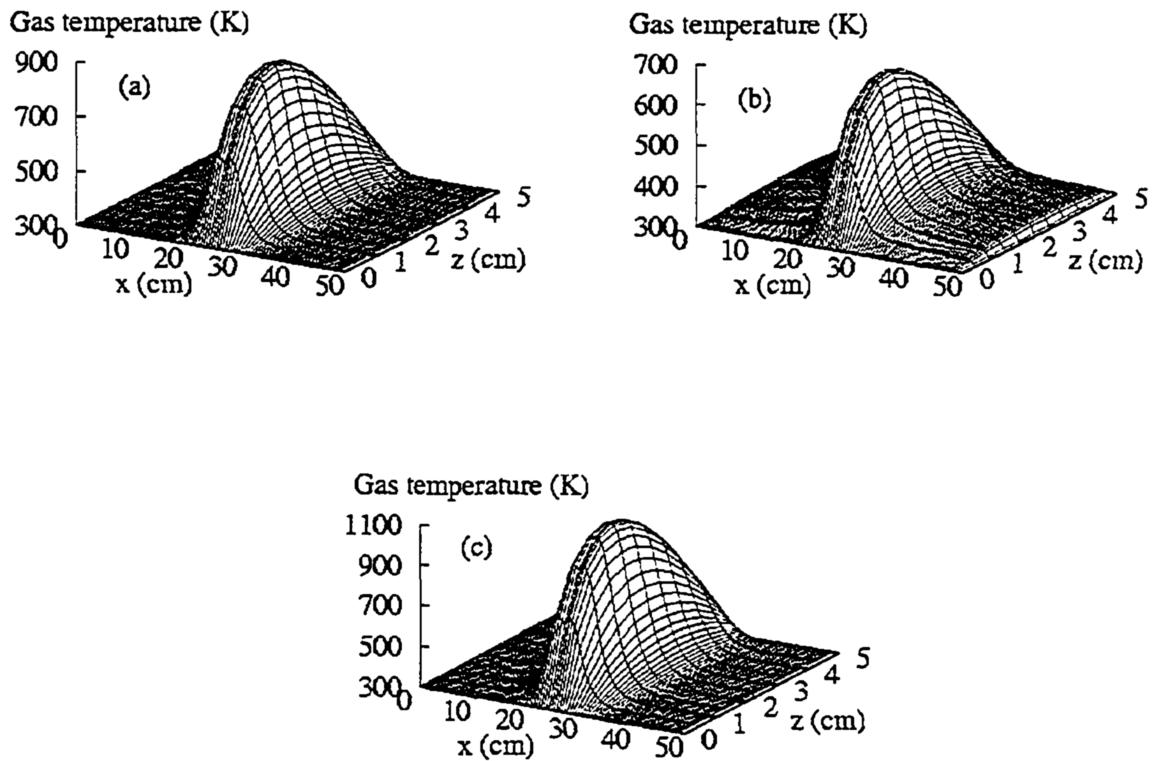

Fig. 6.8 Longitudinal gas temperature profile for the sputtering of Cu at a magnetron power density of about 40 W/cm^2 and pressure of 7.5 mTorr using (a) argon (b) neon and (c) krypton as the background gas, with the substrate plane at 5 cm above the target.

Reproduced with permission of the copyright owner. Further reproduction prohibited without permission.

6.2.5 Effect of Target Location

It is common to have the target of a sputtering system located along the central axis of the chamber, if it has only one sputter source. However, in systems with multiple sources, the target may be located at some distances off the central axis. For instance, the magnetron sputtering system referred to as "Bob" in the University of Alberta Nanofab Facility, has two sources located about 16 cm off the central axis of the 24 cm radius chamber. Since, heat conduction has been identified as the main problem of gas heating, it is expected that the location of the "local heat source" may have an effect on the maximum gas temperature. To study this effect, the target was modeled at about 16 cm from the central axis (similar to Bob). Fig. 6.9 shows (a) the longitudinal and (b) transverse temperature profiles for the sputtering of Cu at 7.5 mTorr and 40 W/cm^2, with the substrate plane located at 5 cm above the target. The results show that the maximum temperature increases slightly by about 10 K from the case when the target was located along the central axis. This minor change in the gas maximum temperature shows that the temperature does not change significantly, if the target location is changed under the same system geometry and process conditions. However, as would be expected, the temperature of the chamber wall close to the target is greater (about 50 K) than that for a corresponding location away from the heat source.

Reproduced with permission of the copyright owner. Further reproduction prohibited without permission.

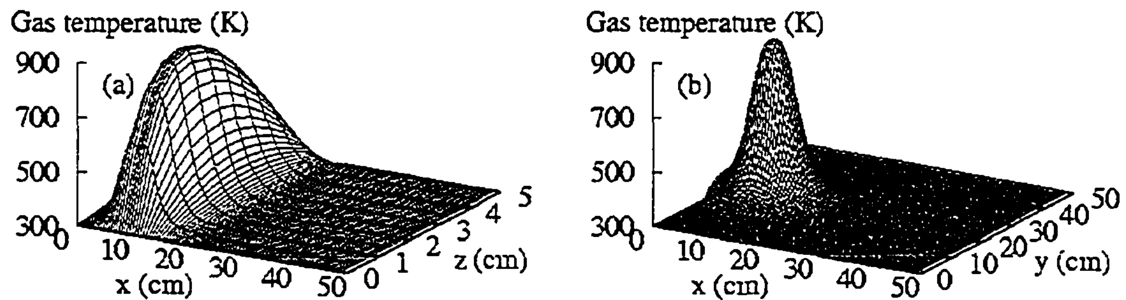

Fig. 6.9 (a) Longitudinal and (b) transverse temperature profile of an off-axis sputter source for the sputtering of Cu at 7.5 mTorr and magnetron power of 40 W/cm^2, with the substrate plane located at 5 cm above the sputter source.

6.2.6 Effect of Target Size / Width of Etch Track

In section 5.1.3, it was shown that the size of the target (width of the erosion track), and the radius of the inner etch track have great effect on the on-axis deposition rate of the sputter particles. It is thus expected that these might, as well, affect the gas temperature profile. To simulate this effect, the radii of the inner and outer etch track were respectively, increased to 2.9 and 5.7 cm (to give a larger etch track (LET)), with the target modeled at the centre of the chamber. Fig. 6.10 shows the simulated results for Al particles at an argon pressure of 7.5 mTorr. The power density was maintained at 40 W/cm^2, and the substrate location modeled at 15 cm from the target. Fig. 6.10 (a) shows

Reproduced with permission of the copyright owner. Further reproduction prohibited without permission.

the longitudinal temperature profile. In comparing this with Fig. 6.3 (a), it is evident that the gas heating space in this case (LET) is larger than in the case of the smaller etch track (SET). Since, the heating space extends further to toward the substrate, then it is expected that the energy flux towards the substrate would be higher than if a smaller target were used under the same process conditions. Fig. 6.10 (b) shows the transverse temperature profile at about 1.96 cm above the target. The profile indicates a lower on-axis temperature compared to the nearby off-axis values. This effect was not observed with the smaller target at this distance, though it is present at short distances from the target. This is due to the filling of the sputtered particles, as the inner radius is far away from the centre of the target. In Fig. 6.10 (c), the on-axis temperatures for both SET and LET are plotted. This figure shows that the location of the maximum temperature shifts away from the target with the inner radius of the etch track. The maximum temperature is slightly greater (by about 25 K) as more of the particles reach this location than in the case of the smaller track. The trend here correlates with that of the particle deposition profile. This suggests that sputtered particles may have the most effect on the gas heating.

Reproduced with permission of the copyright owner. Further reproduction prohibited without permission.

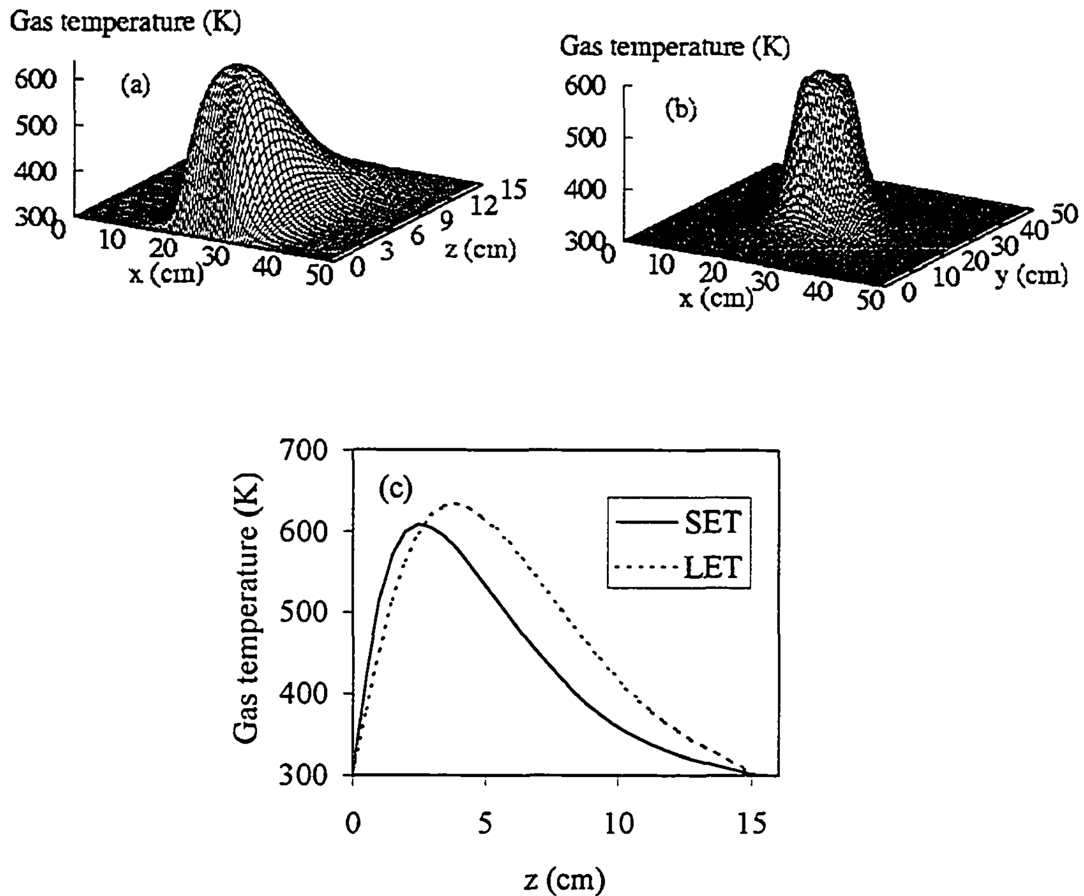

Fig. 6.10 (a) Longitudinal and (b) transverse temperature profile of an on-axis sputter source (with etch track radii of 2.9 and 5.7 cm - LET) for the sputtering of Al at 7.5 mTorr and magnetron power of 40 W/cm^2, with the substrate plane located at 15 cm above the sputter source. (c) compares the temperature profile along the central axis for both SET (etch radii of 0.9 and 3.25 – small etch track), and LET.

Reproduced with permission of the copyright owner. Further reproduction prohibited without permission.

6.2.7 Individual Contributions to the Gas Heating

In this study, sputtered particles, reflected neutrals, electrons and ions are considered as the sources of the power input to the gas. However, to clearly understand the importance of each as an energy source to the gas heating, the total input power was separated into individual sources and the gas temperatures calculated. The contribution of the reflected neutrals depends strongly on the ratio of the mass of the target to that of the gas. For cases where the ratio is less than 1, such as the cases for aluminum and argon, copper and krypton, etc, the particle reflection coefficient is negligibly small, and hence there is no contribution to the total input power. However, in cases where the mass ratio is more than 1 (copper and argon, copper and neon, etc), the reflected neutrals may contribute to the total input power. Thus, Cu is used here as a case study.

Table 6.2 shows the percentage contribution of sputtered Cu atoms, reflected neutrals, electrons and ions to the maximum gas temperature for the magnetron sputtering of Cu at argon gas pressures of 7.5 and 30 mTorr respectively. The magnetron power density is 40 W/cm^2 and the substrate plane is located at 5 cm above the target. The results show that at a low pressure of 7.5 mTorr, sputtered atoms contributed about 99.0%, reflected neutrals contributed only 0.9%, and electrons 0.1% to the maximum gas temperature. The

Reproduced with permission of the copyright owner. Further reproduction prohibited without permission.

contribution of the ions was almost 0%. This percentage contribution was found to change considerably with pressure. For instance, at 30 mTorr, the contribution from electrons was found to increase to about 12%, ions to 4% and that of the reflected neutrals increased slightly to 2%.

Since the reflected neutrals are the neutralized ions, which rebound from the target surface, they typically have energies of a few hundred eV. Because of this high energy, the cross section for momentum transfer of reflected neutrals can be an order of magnitude smaller than that of the sputtered atoms. This implies that reflected neutrals have long path lengths and can traverse the plasma without any significant collisions. At increased pressure, their path length reduces and they may under go some collisions, and transfer some of their energies to the background gas, as evident from the result at 30 mTorr.

The contributions of electrons and ions depend strongly on their densities, temperatures, as well as the "bias" potential (difference between the plasma and floating potentials). The results of Langmuir probe measurements of magnetron plasma [215,227,228], show that generally the electron density increases with pressure, while the electron temperature decreases slightly with pressure. The absolute value of the spatial floating potential also decreases with pressure. The increase in the electron density and the decrease in the

Reproduced with permission of the copyright owner. Further reproduction prohibited without permission.

absolute value of the floating potential with pressure imply that the flux of electrons away from the magnetic confinement increases with pressure. This is evident in the increased contribution of electrons at 30 mTorr. The ion temperatures are usually lower than the electron temperatures, thus, the contribution of the ions to the gas heating would be significantly smaller than that of the electrons, as observed in the result of the simulation.

Table 6.2 Percentage contribution of sputtered atoms, reflected neutrals, electrons and ions to the gas heating for the magnetron sputtering of Cu at magnetron power density of 40 W/cm^2 and argon gas pressures of 7.5 and 30 mTorr, with the substrate plane located at 5 cm above the target.

Factors	Percentage contribution at 7.5 mTorr (%)	Percentage contribution at 30 mTorr (%)
Sputtered atoms	99.0	82
Reflected neutrals	0.9	2
Electrons	0.1	12
Ions	0	4

Reproduced with permission of the copyright owner. Further reproduction prohibited without permission.

Chapter 7

Conclusions and Recommendations

7.1 Conclusions

In this thesis, the various energy sources to the substrate during a dc magnetron sputter deposition are explored. A novel experimental approach to measuring energy flux using a micro-machined temperature probe is demonstrated. A 3-D model is developed for the estimation of deposition rate and another model for the estimation of the individual contributions to the total deposited energy. The sum of these contributions is compared with the experimentally determined total energy flux. The models compare quite well with the experiment. The total energy per deposited atom is determined. The energy model can be easily modified for a biased substrate. Gas heating has been identified to have a significant effect on sputter deposition [63], thus a 3-D numerical simulation is carried out to properly understand the factors that contribute to the gas heating. It is expected that this thesis will provide useful tools for proper understanding, as well as make a significant contribution to the field of sputter deposition of materials.

Reproduced with permission of the copyright owner. Further reproduction prohibited without permission.

The following is a summary of the various issues addressed in the study:

7.1.1 Micromachined Temperature Probe

The temperature sensors were fabricated using a 1.5 μm CMOS process courtesy of the Canadian Microelectronics Corporation with some post-processing. The sensor's behaviour was approximated well by a first order temperature response. The relative change in the sensor resistance was found to depend linearly with power up to a certain power limit. For the sensor used, the change in temperature limit was found to be about 250 K. The thermal characteristics of the sensor were found to be affected by that of the package especially during the sputter deposition. Only a limited positive bias (< 10 V) could be applied before the sensor was damaged by electron bombardment. The sensitivity of the sensors was found to increase by etching the silicon underneath the polysilicon.

7.1.2 Deposition Rate

Two types of particle fluxes contribute to the total flux at the substrate. These are those with ballistic motion and those with diffusive behaviour. The diffusive ones have been thermalized as a result of loss of energy caused by collisions. In this work, in order to

Reproduced with permission of the copyright owner. Further reproduction prohibited without permission.

represent the broad pressure range that is used in magnetron sputter deposition, both types are considered. The gas heating effect is incorporated into the 3-D deposition model. The model compares well with experiments given the dc magnetron sputtering system used for the study. The dependence of deposition rate with magnetron power seems to be non-linear, and may be attributed to the gas rarefaction effect.

The deposition shape profile is greatly affected by the size of etch track on the target. Magnetron power, target material and pressure do not significantly affect the deposition rate profile. Uniform film over a large area (slightly less than the area of the target) can be coated faster by placing the substrate at a distance greater than 2 times the inner radius of the etch track, but not much greater than the outer radius, rather than place the substrate at very large distances where the deposition rate is very low.

Since the scattering process depends on the process parameters and the target material, it has been shown that for a given power, pressure and target-substrate distance, Al particles show more of this effect than do Cu particles. The model is equally useful in predicting the thermalization of sputtered particles in terms of the ratio of diffused particle flux to the total flux as a function of power and pressure-distance product.

Reproduced with permission of the copyright owner. Further reproduction prohibited without permission.

7.1.3 Total Energy Flux at the Substrate

The steady state energy flux at the substrate was measured to vary from 9.6 to 46 mW/cm^2 at a substrate-target distance of 10.8 cm during the deposition of Al, depending on the magnetron power (75 – 300 W) and gas pressure. The model predicts a non-linear dependence of the total energy flux on the magnetron power. The deviation from the linear dependence is as a result of the fact that not all factors contributing to the total energy vary linearly with the magnetron power. Plasma irradiation and electrons are shown to be the major sources of energy during the deposition of Al at a power of 200W [127]. Thermal radiation from the hot shield around the target is also shown to contribute to the total energy flux at the substrate.

The total energy deposited at the substrate during the deposition of Cu (25 to 114 mW/cm^2) was found to be greater than that for Al at the same magnetron power and pressure. This is as a result of the higher sputtering yield of Cu, and the contribution from the reflected gas neutrals at the target.

Reproduced with permission of the copyright owner. Further reproduction prohibited without permission.

7.1.4 Total Energy per Deposited Atom

The total energy per deposited atom was found to depend on the discharge power and pressure regimes (given the pressures under study). At low power regimes, it increases with pressure, but decreases with power. At high powers, it trends towards being constant and independent of both pressure and power. Values of about 28 and 25 eV were obtained for Al and Cu respectively at regions not too far from the target. Away from the target, they were found to increase with distance, this may be probably due to the scaling of the radiation inputs with the deposition efficiency.

These results resolve the earlier contradictions, in terms of power regimes, between Thornton [129] who observed a pressure and power independent energy per atom, and Drusedau, *et al* [176] who observed an increase in the energy per atom with pressure, but a decrease with power. The seemingly large values of the energy per atom observed at low powers and large pressure-distance products are attributed to the differences in the dependence of all the factors on the process parameters.

Reproduced with permission of the copyright owner. Further reproduction prohibited without permission.

7.1.5 Simulation of Gas Heating

The problem of gas heating is mainly that of heat conduction from the plasma region (local heat source) near the target through the gas to the chamber walls. Since different gases have different thermal conductivities, the type of sputtering gas used determines the maximum temperature of the gas. For a given power density, the maximum gas temperature increases with pressure (in the range of pressures studied).

Sputtered particles are shown to be the greatest contributing factor to the gas heating, especially at low pressures. Moving the substrate plane farther away from the target plane causes an increase in the maximum gas temperature up to when most of the sputtered particles are thermalized. The contributions of electrons, ions and reflected neutrals depend very strongly on pressure. At low pressures, their contributions are very small. The location of the sputter source relative to the chamber walls affects the maximum gas temperature slightly. Target materials with high sputtering rate show more of the gas heating than those with low sputtering rate. The location of the maximum gas temperature depends strongly on the size of the target and to a less extent on gas pressure.

Reproduced with permission of the copyright owner. Further reproduction prohibited without permission.

7.2 Recommendations for Further Work

The general areas for further work so as to enhance the general applicability of the model include the following. First, more experimental measurements could be carried out with materials having high masses, such as tungsten, and under a wide range of pressures, and the results compared with the model. Secondly, the energy model could be refined to include variations of magnetron sputtering such as radio frequency (rf) and ionized physical vapour deposition (IPVD). As well, improved models of the target shield, substrate heating and reflectivity of the substrate surface could be developed to capture more of the system behaviour and dynamics.

Reproduced with permission of the copyright owner. Further reproduction prohibited without permission.

Bibliography

[1] K.J Klabunde, "Introduction to Free Atoms and Particles" in *Thin Films from Free Atoms*, (edited by K.J. Klabunde), Academic Press, Orlando, p. 1 (1985).

[2] R.F. Bunshah, "Deposition Technologies: An Overview" in *Deposition Technologies for Films and Coatings*, edited by R.F. Bunshah, Noyes Publication, Park Ridge, p.1 (1982).

[3] W.R. Runyan and K.E. Bean, *Semiconductor Integrated Circuit Processing Technology*, Addison-Wesley, Reading (1990).

[4] D.K Ferry, L.A. Akers, and E.W. Greeneich, *Ultra Large Scale Integrated Microelectronics*, Prentice Hall, New Jersey (1988).

[5] H.R. Huff, "From the Lab to the Fab: Transistors to Integrated Circuits", AIP Conference Proceedings, Vol. 683, No. 1, p.3 (2003).

[6] A.-L. Barabasi and H.E. Stanley, *Fractal Concepts in Surface Growth*, Cambridge University Press, Cambridge, (1995).

[7] M. Bohr, "Intel's 65 nm Logic Technology Demonstrated on 0.57 μm^2 SRAM Cells", www.intel.com/research/silicon/mircon.htm, November 24, 2003.

[8] "Accelerating the Convergence of Computing and Communications", Intel Developer Update Magazine, April 2003.

[9] L. Eckertova, *Physics of Thin Films*, Plenum Press, New York, (1986).

[10] H.F. Winters and E. Kay, "Gas Incorporation into Sputtered Films", Journal Applied Physics, Vol. 38, No. 10, p. 3928 (1967).

[11] W.E. Hardy and D. Mills, "Effects of Deposition Temperature on Ta Thin Film Resistors Reactively Sputtered in Oxygen", Journal of Vacuum Science Technology, Vol. 10, No. 1, p. 303 (1973).

Reproduced with permission of the copyright owner. Further reproduction prohibited without permission.

[12] J.A. Thornton, "Influence of Apparatus Geometry and Deposition Conditions on the Structure and Topography of Thick Sputtered Coatings", Journal of Vacuum Science and Technology, Vol. 11, No. 4, p.666 (1974).

[13] J.A. Thornton, J. Tabock and W. Hoffman, "Internal Stresses in Metallic Films Deposited by Cylindrical Magnetron Sputtering", Thin Solid Films, Vol. 64, p.111 (1979).

[14] D.W. Hoffman and J.A. Thornton, "Internal Stresses in Cr, Mo, Ta, and Pt Films Deposited by Sputtering from a Planar Magnetron Source", Journal of Vacuum Science and Technology, Vol. 20, No. 3, p.355 (1982).

[15] J.A. Thornton and D.W. Hoffman, "The Influence of Discharge Current on the Intrinsic Stress in Mo Films Deposited Using Cylindrical and Planar Magnetron Sputtering Sources", Journal of Vacuum Science and Technology, A Vol. 3, No. 3, p.576 (1985).

[16] S.M. Rossnagel, M.A. Russak, and J.J. Cuomo, "Pressure and Plasma Effects on the Properties of Magnetron Sputtered Carbon Films", Journal of Vacuum Science and Technology, A, Vol. 5, No. 4, p. 2150 (1987).

[17] K.-H. Muller, "Stress and Microstructure of Sputter Deposited Thin Films: Molecular Dynamics Investigations", Journal of Applied Physics, Vol. 62, No. 5, p. 1796 (1987).

[18] M. Georgson, A. Roos and C.-G. Ribbing, "The Influence of Preparation Conditions on the Optical Properties of Titanium Nitride Based Solar Control Films", Journal of Vacuum Science and Technology, A, Vol. 9, No. 4, p. 2191 (1991).

[19] H. Windischmann, "Intrinsic Stress in Sputtered Thin Films", Journal of Vacuum Science and Technology, A Vol. 9, No. 4, p.2431 (1991).

Reproduced with permission of the copyright owner. Further reproduction prohibited without permission.

[20] R.N. Tait, S.K. Dew, T. Smy and M.J. Brett, "Density Variation of Tungsten Films Sputtered Over Topography", Journal of Applied Physics, Vol. 70, No. 8, p.4295 (1991).

[21] N. Motegi, Y. Kashimoto, K. Nagatani, S. Takahashi, T. Kondo, Y. Mizusawa and I. Nakayama, "Long-throw Low-pressure Sputtering Technology for Very Large-scale Integrated Devices", Journal of Vacuum Science Technology, B, Vol. 13, No. 4, p.1906 (1995).

[22] F. Klabunde, M. Lohmann, J, Blasing and T. Drusedau, "The Influence of Argon Pressure on the Structure of Sputtered Molybdenum: From Porous Amorphous to a New Type of Highly Textured Film", Journal of Applied Physics, Vol. 80, No. 11, p.6268 (1996).

[23] M. Kalff, M. Breeman, M. Morgenstern, T. Michely and G. Comsa, "Effect of energetic particles on island formation in sputter deposition of Pt on Pt(111)". Applied Physics Letters, Vol. 70, No. 2, p.182 (1997).

[24] T.P. Drusedau, F. Klabunde, P. Veit and TH. Hempel, "Investigation on Microstructure, Surface Topography, and Growth Process of Sputtered Molybdenum Showing Texture Turnover", Phys. Stat. Sol. A, Vol.161, p.167 (1997).

[25] J. Musil and J. Vlcek, "Magnetron Sputtering of Films with Controlled texture and Grain Size", Material Chemistry and Physics, Vol. 54, p.116 (1998).

[26] L.-J. Meng and M.P. dos Santos, "Influence of the Target-substrate Distance on the Properties of Indium Tin Oxide Films Prepared by Radio Frequency Reactive Magnetron Sputtering", Journal of Vacuum Science and Technology, A, Vol. 18, No. 4, p.1668 (2000).

[27] Q. Li, Y.-H. Yu. C.Singh Bhatia, L.D. Marks, S.C. Lee and Y.W. Chung, "Low-temperature Magnetron Sputter-deposition, Hardness, and Electrical Resistivity

Reproduced with permission of the copyright owner. Further reproduction prohibited without permission.

of Amorphous and Crystalline Alumina Thin Films", Journal of Vacuum Science and Technology, A, Vol. 18, No. 5, p.2333 (2000).

[28] F,-J, Haug, Zs. Geller, H. Zogg, A.N. Tiwari and C. Vignali, "Influence of Deposition Conditions on Thermal Stability of ZnO:Al Films Grown by RF Magnetron Sputtering", Journal of Vacuum Science and Technology, A, Vol. 19, No. 1, p.171 (2001).

[29] S. Venkataraj, J. Geurts, H. Weis, O. Kappertz, W.K. Njoroge, R. Jayavel and M. Wuttig, "Structural and Optical Properties of Thin Lead Oxide Films Produced by Reactive Direct Current Magnetron Sputtering", Journal of Vacuum Science and Technology, A, Vol. 19, No. 6, p.2870 (2001).

[30] Y. Senzaki, "Chemical Vapour Deposition of Copper Using a New Liquid Precursor with Improved Thermal Stability", Advanced Metallization and Interconnect Systems for ULSI Applications in1997: Conference Proceedings ULSI XIII, Materials Research Society, p. 451 (1998).

[31] P. Doppelt, T.-Y. Chen, O. Fischer, and M. Stelzle, "Single-Step Selective Metallization of Different Patterned Activated Surfaces by Copper CVD", Advanced Metallization and Interconnect Systems for ULSI Applications in 1997: Conference Proceedings ULSI XIII, Materials Research Society, p.463 (1998).

[32] G. Bai, C. Chiang, J.N. Cox, S. Fang, D.S. Gardner, A. Mack, T. Marieb, X-C. Mu, V. Ochoa, R. Villasol, and J. Yu, "Copper Interconnection Deposition Techniques and Integration", Symposium on VLSI Technology: Proceedings, Honolulu, p. 48 (1996).

[33] T. Andryushchenko, W. Holtkamp, W.C. Ko, F. Lin, D. Papapanayiotou, B. Stickney and C.H. Ting, "Copper Electroplating Process in Single Wafer Processing Chamber with in-situ Spin Rinse-dry", Proceedings of the 15th

Reproduced with permission of the copyright owner. Further reproduction prohibited without permission.

International VLSI Multilevel Interconnection Conference, Santa Clara, p.55 (1998).

[34] M. Paunovic, P.J. Bailey, R.G. Schad, D.A. Smith, "Electrochemically Deposited Diffusion Barriers", Journal of Electrochemical Society, Vol. 141, No 7, p.1843 (1994).

[35] V.M. Dubin, C.H. Ting, R. Cheung, R. Lee and S. Chen, "Copper Plating Techniques for ULSI Metallization", Advanced Metallization and Interconnect Systems for ULSI Applications in 1997: Conference Proceedings ULSI XIII, Materials Research Society, p.405 (1998).

[36] S. Lopatin, Y. Shacham-Diamand, V. Dubin, P.K. Vasudev, Y. Kim, and T. Smy, "Characterization of Electroless Cu, Co, Ni and Their Alloys for ULSI Metallization", Advanced Metallization and Interconnect Systems for ULSI Applications in1997: Conference Proceedings ULSI XIII, Materials Research Society, p.437 (1998).

[37] T. Smy, S. Lopatin, Y. Shacham-Diamand, S.K. Dew, and M.J. Brett, "Simulation of the Microstructure and Profile Evolution of Cu Films Deposited over ULSI Topography by Electroless Deposition", Advanced Metallization and Interconnect Systems for ULSI Applications in 1997: Conference Proceedings ULSI XIII, Materials Research Society, p.457 (1998).

[38] R.F. Bunshah, "High Rate Physical Vapour Deposition Processes", in Materials Coatings Techniques, (edited by R.F. Bunshah), Agard Lecture Series, NATO, No. 106, p.2-1 (1980).

[39] L.L. Mercado, C. Goldberg, S-H. Kuo, T-Y. Lee, and S.K. Pozder, "Analysis of Flip-Chip Packaging Challenges on Copper / Low-*k* Interconnects", IEEE Transactions on Device and Materials Reliability, Vol. 3, No. 4, p. 111 (2003).

[40] Peter Singer, "Copper Goes Mainstream: Low k to Follow", Semiconductor International, Vol. 20, No. 13, p. 67 (1997).

Reproduced with permission of the copyright owner. Further reproduction prohibited without permission.

[41] Z. Liu, T. Omstead, and J. Bottin, "MOCVD Cu Process for Seed Layer and Fill Applications", Advanced Metallization Conference in 1998: Conference Proceedings ULSI XIV, Materials Research Society, p.141 (1999).

[42] A. Jain, C. Simpson, T. Saaranen, R. Venkatraman, M. Herrick, M. Angyal, R. Bajaj, C. Dang, S. Das, D. Denning, J. Farkas, D. Watts, C. Capasso, J. Gelatos, R. Islam, B. Smith, T. Sparks, P. Crabtree, S. Filipiak, C. King, B. Fiordalice, H. Kawasaki, J. Klien, S. Venkatesan and E. Weitzman, "CVD TiN and Hybrid Barriers for Back-end Copper Interconnect Technology", Advanced Metallization and Interconnect Systems for ULSI Applications in 1997: Conference Proceedings ULSI XIII, Materials Research Society, p. 41 (1998).

[43] C. Ting, V. Dubin, and T. Nogami, "Recent Advances in Cu Metallization", Proceedings of the 13th VLSI Multilevel Interconnection Conference, Santa Clara, p. 481 (1996).

[44] S. Sharan and G.S. Sandhu, "Contact Metallization for High Aspect Ratio Contacts", Advanced Metallization and Interconnect Systems for ULSI Applications in 1997: Conference Proceedings ULSI XIII, Materials Research Society, p.23 (1998).

[45] T. Suzuki, A. Tsukune, O. Tsuboi, M. Yamada, C. Galewski and C.A. Sans, "Comparison of CVD TiN, PECVD WN_x, and CVD W-Si-N as Upper Electrode Materials for Ta_2O_5 DRAM Capacitors", Advanced Metallization and Interconnect Systems for ULSI Applications in 1997: Conference Proceedings ULSI XIII, Materials Research Society, p. 49 (1998).

[46] Y.-P. Chen, G. Dixit, J.-P. Lu, J. Luttmer, and R. Havemann, "$TiCl_4$ and TiI_4 Based Inorganic CVD Ti/TiN Films for Gigabit DRAM Contact Metallization", Advanced Metallization and Interconnect Systems for ULSI Applications in 1997: Conference Proceedings ULSI XIII, Materials Research Society, p.57 (1998).

Reproduced with permission of the copyright owner. Further reproduction prohibited without permission.

[47] A. Telikepalli, "Virtex-II Pro FPGAs: The Platform for Programmable Systems Has Arrived" Xcell Journal, Issue 42, p. 10 (2002).

[48] Alexander Braun, "Aluminum Persists as Copper Age Dawns", Semiconductor International, Vol. 22, No.9, p.58 (1999).

[49] G.N. Jackson, "RF Sputtering", Thin Solid Films, Vol. 5, p.209 (1970).

[50] R. Glang, "Vacuum Evaporation", in *Handbook of Thin Film Technology*, (edited by L.I. Maissel and R. Glang), McGraw Hill, New York, p.1-3 (1970).

[51] L. Holland, *Vacuum Deposition of Thin Films*, Wiley, New York, (1956)

[52] L.R. Shaginyan, M, Misina, S. Kadlec, L. Jastrabik, A. Mackova and V. Perina, "Mechanism of the Film Composition Formation during Magnetron Sputtering of WTi", Journal of Vacuum Science and Technology, A, Vol. 19, No. 5, p. 2254 (2001).

[53] L.T. Ball, I.S. Falconer, D.R. Mckenzie, and J.M. Smelt, "An Interferometeric Investigation of the Thermalization of Copper Atoms in a Magnetron Sputtering Discharge", Journal of Applied Physics, Vol. 59, No. 3, p. 720 (1986).

[54] A. Gratis-Marti and J. Valles-Abarca, "Slowing Down and Thermalization of Sputtered Particle Fluxes: Energy Distributions", Journal of Applied Physics, Vol. 54, No. 2, p. 1071 (1983).

[55] G.M. Turner, I.S. Falconer, B.W. James, and D.R. Mckenzie, "Monte Carlo Calculation of the Thermalization of Atoms Sputtered from the Cathode of a Sputtering Discharge", Journal of Applied Physics, Vol. 65, No. 9, p. 3671 (1989).

[56] J. Valles-Abarca, and A. Gratis-Marti, "Evolution Towards Thermalization, and Diffusion of Sputtered Fluxes: Spatial Profiles", Journal of Applied Physics, Vol. 55, No. 5, p. 1370 (1984).

[57] R.V. Stuart, *Vacuum Technology, Thin Films, and Sputtering: An Introduction*, Academy Press, New York, p. 91 (1983).

Reproduced with permission of the copyright owner. Further reproduction prohibited without permission.

[58] J.B. Webb, "Formation of Thin Semiconducting Films by Magnetron Sputtering", in *Thin Films from Free Atoms and Particles*, (edited by K.J. Klabunde), Academic Press, Orlando, p. 257 (1985).

[59] H. Urbassek and D. Sibold, "Sputtered Atom Transport in High-current Gas Discharges: A Self-consistent Computer Simulation Study", Journal of Vacuum Science and Technology, A Vol. 11, No. 13, p.676 (1993).

[60] J.A. Thornton, "Coating Deposition by Sputtering" in *Deposition Technologies for Films and Coatings*, R.F. Bunshah, ed., Noyes Publication, Park Ridge, p.170 (1982).

[61] Y. Yamamura and M. Ishida, "Monte Carlo Simulation of the Thermalization of Sputtered Atoms and Reflected Atoms in the Magnetron Sputtering Discharge", Journal of Vacuum Science and Technology, A Vol. 13, No. 1, p.101 (1995).

[62] A. Bogaerts, M. Straaten, and R. Gijbels, "Description of the Thermalization Process of the Sputtered Atoms in a Glow Discharge Using a Three-Dimensional Monte Carlo Method", Journal of Applied Physics, Vol. 77, No. 5, p.1868 (1995).

[63] S.M. Rossnagel, "Gas Density Reduction Effects in Magnetrons", Journal of Vacuum Science and Technology, A, Vol. 6, No. 1, p.19 (1988).

[64] T. Motohiro, "Applications of Monte Carlo Simulation in the Analysis of a Sputter-Deposition Process", Journal of Vacuum Science and Technology, A, Vol. 4, No. 2, p.189 (1986).

[65] T. Motohiro and Y. Taga, "Monte Carlo Simulation of the Particle Transport Process in Sputter Deposition", Thin Solid Films, Vol. 112, p.161 (1984).

[66] A. Kersch, W. Morokoff, and C. Werner, "Self-consistent simulation of sputter deposition with the Monte Carlo method", Journal of Applied Physics, Vol. 75, No. 4, p.2278 (1994).

Reproduced with permission of the copyright owner. Further reproduction prohibited without permission.

[67] V.V. Serikov and K. Nanbu, "The Analysis of background gas heating in direct current sputtering discharge via particle simulation", Journal of Applied Physics, Vol. 82, No. 12, p.5948 (1997).

[68] J.E. Foster, A.E. Wendt, W.W. Wang, and J.H. Booske, "Determination of Metal Vapour Ion Concentration in an Argon/Copper Plasma for Ionized Physical Vapour Deposition", Journal of Vacuum Science and Technology, A Vol. 16, No. 4, p.2198 (1998).

[69] S.M. Rossnagel, "Interaction Between Gas Rarefaction and Metal Ionization in Ionized Physical Vapour Deposition", Journal of Vacuum Science and Technology, B Vol. 16, No. 6, p.3008 (1998).

[70] S.M. Rossnagel, "Directional and Preferential Sputtering-based Physical Vapour Deposition", Thin Solid Films, Vol. 263, p.1 (1995).

[71] M. Dickson, F. Qian, and J. Hopwood, "Quenching of Electron Temperature and Electron Density in Ionized Physical Vapour Deposition", Journal of Vacuum Science and Technology, A Vol. 15, No. 2, p.304 (1997).

[72] M. Dickson and J. Hopwood, "Axially-Resolved Study of Highly Ionized Physical Vapour Deposition", Journal of Vacuum Science and Technology, A Vol. 15, No. 4, p.2307 (1997).

[73] S. Hamaguchi and S.M. Rossnagel, "Liner Conformality in Ionized Magnetron Sputter Metal Deposition Processes", Journal of Vacuum Science and Technology, B Vol. 14, No. 4, p.2603 (1996).

[74] S.M. Rossnagel, "Filling Dual Damascene Interconnect Structures with AlCu and Cu using Ionized Magnetron Deposition", Journal of Vacuum Science and Technology, B Vol. 13, No. 1, p.125 (1995).

[75] W.M. Holber, "Electron cyclotron Resonance (ECR) Ion sources", in *Handbook of Ion Beam Processing Technology,* (edited by J. Cuomo, S. Rossnagel, and H. Kaufman), Park Ridge, New Jersey, Noyes, p. 21 (1989).

Reproduced with permission of the copyright owner. Further reproduction prohibited without permission.

[76] J. Asmussen, "Electron cyclotron resonance microwave discharge for ectching and thin film deposition," in *Handbook of Plasma Processing Technology*, (edited by S. Rossnagel, J. Cuomo, and W. Westwood), Park Ridge, New Jersey, Noyes, p.285 (1990).

[77] J.J. Cuomo and S.M. Rossnagel, "Hollow Cathode-enhanced Magnetron Sputtering", Journal of Vacuum Science and Technology, A Vol. 4, p.393 (1986).

[78] S.M. Rossnagel, "Sputtered Atom Transport Processes", IEEE Transactions on Plasma Science, Vol. 18, No. 6, p.878 (1990).

[79] M. Venugopalan and R Avni, "Analysis of Glow Discharges for the Understanding the Process of Film Formation", in *Thin Films from free Atoms and Particles*, (edited by K.J. Klabunde), Academy Press, Orlando, p.49 (1985).

[80] P. Sigmund, "Sputtering by Ion Bombardment: Theoretical Concepts", in *Sputtering by Particle Bombardment*, (edited by R. Behrisch), Springer, Berlin, Vol. I p.9 (1981).

[81] M.W, Sckerl, P. Sigmund and M. Vicanek, "Particle Fluxes in Atomic Collision Cascades", Matematisk-fysiske Meddelelser, The Royal Danish Academy of Sciences and Letters, Vol. 44, No. 3, p.5 (1996).

[82] J.M. Bordes, Ch. Bordes, E, Ehret, R. Gschwind, and Ph. Bauer, "Theoretical Sputtering Yields of Al and Mg Targets in PVD Processes", Journal of Vacuum Science and Technology, A Vol. 19, No. 3, p.805 (2001).

[83] J.A. Thornton and J.E. Greene, "Sputter Deposition Process", in *Handbook of Deposition Technologies for Films and Coatings*, (edited by R.F. Bunshah), Noyes Publications, Park Ridge, p 249, (1994).

[84] W.D. Westwood, "Glow Discharge Sputtering", Progress in Surface Science, Vol. 7, p. 71 (1977).

Reproduced with permission of the copyright owner. Further reproduction prohibited without permission.

[85] L.C. Feldman and J.W. Mayer, *Fundamentals of Surface and Thin Film Analysis,* North Holland, (1992).

[86] J.F. Ziegler and J.P. Biersack, *TRIM.SP Program*, SRIM-2000.39 (1999).

[87] J.M. Bordes and Ph. Bauer, "Depth of Origin", Journal of Vacuum Science and Technology, A Vol. 19, No. 3, p.812 (2001).

[88] M. Stepanova and S.K. Dew, "Estimates of Differential Sputtering Yields for Deposition Applications", Journal of Vacuum Science and Technology, A Vol. 19, No. 6, p.2805 (2001).

[89] C.H. Becker and K.T. Gillen, "Nonresonant Multiphoton Ionization as a Sensitive Detector of Surface Concentrations and Evaporation Rates", Applied Physics Letters, Vol. 45, No. 10, p.1063 (1984).

[90] G. Brauer, D. Hassalkamp, W. Kruger, and A. Scharmann, "The Angular Distributions of Particles Sputtered from Cu, Zr and Au Surfaces by Ion Bombardment at Grazing Incidence", Nuclear Instruments and Methods, B, Vol. 12, p.458 (1985).

[91] C. Eisenmenger-Sittner, A. Bergauer, H. Bangert, and W. Bauer, "Measurement of the Angular Distribution of Sputtered Neutrals in a Planar Magnetron Geometry", Journal of Vacuum Science and Technology, A Vol. 12, No. 2, p.536 (1994).

[92] C. Eisenmenger-Sittner, R. Beyerknecht, A. Bergauer, W. Bauer, and G. Betz, "Angular Distribution of Sputtered Neutrals in a Post Magnetron geometry: Measurement and Monte Carlo Simulation", Journal of Vacuum Science and Technology, A Vol. 13, No. 5, p.2435 (1995).

[93] W.D. Westwood, "Calculation of Deposition Rates in Diode Sputtering Systems", Journal of Vacuum Science and Technology, Vol. 15, p.1 (1978).

[94] R.S. Robinson, "Energetic Binary Collisions in Rare Gas Plasmas", Journal of Vacuum Science and Technology, Vol. 16, No. 2, p.185 (1979).

Reproduced with permission of the copyright owner. Further reproduction prohibited without permission.

[95] R.E Somekh, "Calculations of Thermalization During the Sputter Deposition Process", Vacuum, Vol. 34, No. 9, p.987 (1984).

[96] K. Meyer, I.K. Schuller, and C.M. Falco, "Thermalization of Sputtered Atoms", Journal of Applied Physics, Vol. 52, No.9, p.5803 (1981).

[97] S.S. Nathan, G.M. Rao, and S. Mohan, "Transport of Sputtered Atoms in Facing Targets Sputtering Geometry: A Numerical Simulation Study", Journal of Applied Physics, Vol. 84, No. 1, p.564 (1998).

[98] M.W. Thompson, Philosophical Magazine, Vol. 18, p.377 (1968).

[99] J.B. Hasted, *Physics of Atomic Collisions*, Butterworhts, London, (1972).

[100] I.M. Torrens, *Interatomic Potentials*, Academic Press, New York, (1972).

[101] G.A. Bird, *Molecular Gas Dynamics*, Oxford University Press, London, (1976).

[102] S. Chapman and T.G. Cowling, *The Mathematical Theory of Non-uniform Gases*, 2nd ed., Cambridge University Press, London, (1952).

[103] B. Sturtevant and E.A. Steinhalper, "Intermolecular Potentials from Shock Structure Experiments", in *Rarefied gas Dynamics*, (edited by Sam Fisher), Academic Press, New York, p.159 (1974).

[104] G.A. Bird, "Monte Carlo Simulation in an Engineering Context", Rarefied Gas Dynamics, Vol. 74, Part 1, p.239 (1980).

[105] J.F. Ziegler, J.P. Biersack, and U. Littmark, *Stopping and Ranges of Ions in Matter*, Vol. 1. Pergamon Press, New York, (1985).

[106] T.E. Itina, A.A. Katassonov, W. Marine and M. Autric, "Numerical Study of the Role of Background Gas and System Geometry in Pulsed Laser Deposition", Journal of Applied Physics, Vol. 83, No. 11, p. 6050 (1997).

[107] R.E. Somekh, "The Thermalization of Energetic Atoms During the Sputtering Process", Journal of Vacuum Science and Technology, A Vol. 2, No. 3, p.1285 (1984).

Reproduced with permission of the copyright owner. Further reproduction prohibited without permission.

[108] J.E. Greene, "Nucleation, Film Growth, and Microstructural Evolution", in *Handbook of Deposition Technologies for Films and Coatings: Science and Technology, Applications*, 2nd edition,(edited by R.F. Bunshah), Noyes Publications, Park Ridge, p. 681 (1994).

[109] G.C. Nieman and K.J. Klabunde, "Clustering of Free Atoms and Particles: Polymerization and The Beginning of Film growth", in *Thin Films from Free Atoms*, (edited by K.J. Klabunde), Academic Press, Orlando, P.23, (1985).

[110] J.E. Greene, Proc. NATO Advanced Studies Institute on Plasma – Surface Interactions and Processing of Materials, Alicante, Spain. NATO ASI Series, (Sept 4-16, 1988).

[111] D.M. Mattox, "Non-Elemental Characterization of Films and Coatings" in *Handbook of Deposition Technologies for Films and Coatings: Science and Technology, Applications*, 2nd edition, (edited by R.F. Bunshah), Noyes Publications, Park Ridge, p.643 (1994).

[112] B. Lewis and J.C. Anderson, *Nucleation and Growth of Thin Films*, Academic Press, New York, (1978).

[113] D.W. Hoffman, "Stress and Property Control in Sputtered Metal Films without Substrate Bias", Thin Solid Films, Vol. 107, p.353 (1983).

[114] S. Hosokawa, A. Konishi, K. Hiratsuka, and K. Annoh, "Preparation and Properties of Carbon Films with Magnetron Sputtering", Thin Solid Films, Vol. 73, p.115 (1980).

[115] C. Wyon, R. Gillet, and L. Lombard, "Properties of Amorphous Carbon Films Produced by Magnetron Sputtering", Thin Solid Films, Vol. 122, p.203 (1984).

[116] J. Jacobsen, B.H. Cooper, and J.P. Sethna, "Simulations of energetic beam deposition: From picoseconds to seconds", Physical Review, B, Vol. 58, No. 23, p.15847 (1998).

Reproduced with permission of the copyright owner. Further reproduction prohibited without permission.

[117] T. Michely and C. Teichert, "Adatom Yields, Sputtering Yields, and Damage Patterns of Single-ion Impacts on Pt(111)", Physical Review, B Vol. 50, p.11156 (1994).

[118] B.A. Movchan and A.V. Demshishin, "Study of the Structure and Properties of Thick Vacuum Condensates of Nickel, Titanium, Tungsten, Aluminum Oxide, and Zirconium Dioxide", Fiz. Metal. Metalloved., Vol. 28, No. 4, p.653 (1969).

[119] B.E. Jacobson, "Microstructures of PVD Deposited Characterized by Transmission Electron Microscopy", in *Deposition Technologies for Films and Coatings*, (edited by R.F. Bunshah), Noyes Publications, Park Ridge, p.288 (1982).

[120] J.A. Thornton, "High Rate Thick Film Growth", Annual Review of Material Science, Vol. 7, p.239 (1977).

[121] A.C. Raghuram and R.F. Bunshah, "Effect of Substrate Temperature on the Structure of Titanium Carbide Deposited by Activated Reactive Evaporation", Journal of Vacuum Science and Technology, Vol. 9, p.1389 (1972).

[122] R.F. Bunshah, "Structure/Property Relationships in Evaporated Thick Films and Bulk Coatings", Journal of Vacuum Science and Technology, Vol. 11, No.4, p.633 (1974).

[123] K-H. Muller, "Dependence of Thin Film Microstructure on Deposition Rate by Means of a Computer Simulation", Journal of Applied Physics, Vol. 58, No. 7, p. 2573 (1985).

[124] M.J. Brett, "Structural Transitions in Ballistic Aggregation Simulation of Thin Film Growth", Journal of Vacuum Science and Technology, A Vol. 6, No. 3, p.1749 (1988).

[125] R.N. Tait, *Thin Film Microstructure Effects in VLSI Metallization*, Ph.D. thesis, Department of Electrical Engineering, University of Alberta, Edmonton, (1992).

Reproduced with permission of the copyright owner. Further reproduction prohibited without permission.

[126] D.K. Doughty, E.A. Den Hartog, and J.E. Lawler, "Optogalvanic Measurements of Gas Temperature in the Cathode Fall", Applied Physics Letters, Vol. 46, p.352 (1985).

[127] S.D. Ekpe and S.K. Dew, "Investigation of Thermal Energy Flux at the Substrate during the Sputter Deposition of Aluminum", Journal of Vacuum Science and Technology, A, Vol. 20, No. 6, p. 1877 (2002).

[128] D.J. Ball, "Plasma Diagnostics and Energy Transport of a dc Discharge Used for Sputtering", Journal of Applied Physics, Vol. 43, No. 7, p.3047 (1972).

[129] J.A. Thornton, "Substrate Heating in Cylindrical Magnetron Sputtering Sources", Thin Solid Films. Vol. 54, p.23 (1978).

[130] R. Wendt, K. Ellmer, and K. Wiesemann, "Thermal Power at a Substrate During ZnO:Al Thin Film Deposition in a Planar Magnetron Sputtering System", Journal of Applied Physics, Vol. 82. No. 5, p.2115, (1997).

[131] M. Andritschky, F. Guimaraes, and V. Teixeira, "Energy Deposition and Substrate Heating during Magnetron Sputtering", Vacuum, Vol. 44, No. 8, p.809 (1993).

[132] L.G. Christophorou, *Atomic and Molecular Radiation Physics,* Wiley – Interscience, p. 35, (1997).

[133] D.A. Benoy, J.A.M. van der Mullen, and D.C. Schram, "Radiative Energy Loss in a Non-Equilibrium Argon Plasma", Journal of Physics D: Applied Physics, Vol. 26, p. 1408 (1993).

[134] H. Steffen, H. Kersten, and H. Wulff, "Investigation of the Energy Transfer to the Substrate during the Titanium Deposition in a Hollow Cathode Arc", Journal of Vacuum Science and Technology, A, Vol. 12, No. 5, p.2781 (1994).

[135] H. Kersten, H. Steffen, D. Vender, and H.E. Wagner, "On the Ion Energy Transfer to the Substrate during Titanium Deposition in a Hollow Cathode Arc Discharge", Vacuum, Vol. 46, No. 3, p.305 (1995).

Reproduced with permission of the copyright owner. Further reproduction prohibited without permission.

[136] J.E. Mahan and A. Vantomme, "A Simplified Collisional Model of Sputtering in the Linear Cascade Regime", Journal of Vacuum Science and Technology, A, Vol. 15, No. 4, p.1976 (1997).

[137] M.A. Vidal and R. Asomoza, "Monte Carlo Simulation of the Transport Process in the Growth of a-Si:H Prepared by Cathodic Reactive Sputtering", Journal of Applied Physics, Vol. 67, No. 1, p.477 (1990).

[138] M.J. Goeckner, J.A. Goree, and T.E. Sheridan, Jr., "Monte Carlo Simulation of Ions in a Magnetron Plasma", IEEE Transactions on Plasma Science, Vol. 19, No. 2, p.301 (1991).

[139] W.O. Hofer, "Angular, Energy, and Mass Distribution of Sputtered Particles", in *Sputtering by Particle Bombardment III*, (Edited by R. Behrisch and K. Wittmaack), Topics in Applied Physics, Springer, Berlin, Vol. 64, p.15 (1991).

[140] H.H. Andersen, B. Stenum, T. Sorensen and H.J. Whitlow, "Angular Distribution of Particles Sputtered from Cu, Pt and Ge Targets by KeV Ar^+ Ion Bombardment", Nuclear Instrument and Methods in Physics Research, B6, p. 459 (1985).

[141] S. Kundu, D. Ghose, D. Basu and S.B. Karmohapatro, "The Angular Distribution of Sputtered Silver Atoms", Nuclear Instrument and Methods in Physics Research, B12, p. 352 (1985).

[142] J.M. Jeans, *The Dynamical Theory of Gases*, Dover, New York (1954).

[143] A. Gras-Marti, J.A. Valles-Abarca and A. Bensaoula, "Energy and Momentum Transport by Sputtered and Reflected Streams in a Glow Discharge", Journal of Vacuum Science and Technology, A, Vol. 5, No. 4, p.2217 (1987).

[144] I. Abril, A. Gras-Marti, and J.A. Valles-Abarca, "Energy Transfer Processes in Glow Discharge", Journal of Vacuum Science and Technology, A, Vol. 4, No. 3, p.1773 (1986).

Reproduced with permission of the copyright owner. Further reproduction prohibited without permission.

[145] B. Window and K.-H. Muller, "Strain Ion Bombardment and Energetic Neutrals in Magnetron Sputtering", Thin Solid Films, Vol. 171, p. 183, (1989).

[146] G.M. Turner, "Monte Carlo Calculations of Gas Rarefaction in a Magnetron Sputtering Discharge", Journal of Vacuum Science and Technology, A Vol. 13, No. 4, p.2161 (1995).

[147] L.D. Landau and E.M. Lifshitz, *Mechanics*, 3rd edition, Pergamon Press, London, (1960).

[148] B. Chapman, *Glow Discharge Processes: Sputtering and Plasma Etching*, John Wiley & Sons, New York, (1980).

[149] F. Guimaraes, J. Almeida, and J. Bretagne, "Modeling of the Energy Deposition Mechanisms in an Argon Magnetron Planar Discharge", Journal of Vacuum Science Technology, A, Vol. 9, No. 1, p.133 (1991).

[150] F. Llewellyn-Jones, *The Glow Discharge and an Introduction to Plasma Physics*, Spottiswoode, Ballantyne & Co Ltd, London (1966).

[151] H. Kersten, G.M.W. Kroesen and H. Hippler, "On the Energy Influx to the Substrate during Sputter Deposition of Thin Aluminum Films", Thin Solid Films Vol. 332, p.282 (1998).

[152] S.M. Rossnagel and H.R. Kaufman, "Current-voltage Relations in Magnetrons", Journal of Vacuum Science and Technology, A, Vol. 6, No. 2, p.223 (1988).

[153] A.J. Chapman, *Heat Transfer*, 2nd edition, Macmillan Company, New York (1967).

[154] F.J. Bayley, J.M. Owen, and A.B. Turner, *Heat Transfer*, Nelson, Great Britain (1972).

[155] M.A. Mikheyev, *Fundamentals of Heat Transfer*, Gosenergoizdat (1956).

[156] E.R.G. Eckert, *Introduction to Heat and Mass Transfer*, Translated by J.F. Gross, McGraw-Hill, New York, (1963).

Reproduced with permission of the copyright owner. Further reproduction prohibited without permission.

[157] P.G. Klemens, "Theory of Thermal Conductivity of Solids", in *Thermal Conductivity*, (edited by R.P. Tye), Vol. 1, Academic Press, London, p.2 (1969).

[158] N.V. Tsederberg, *Thermal Conductivity of Gases and Liquids*, MIT Press, Cambridge (1965).

[159] M. Nickolay, L. Fischer, and H. Martin, "Shape Factors for Conductive Heat Flow in Circular and quadratic Cross-sections", International Journal of Heat and Mass Transfer, Vol. 41, No. 11, p.1437 (1998).

[160] O. Leroy, J. Perrin, J. Jolly, M. Pealat, and M. Lefebvre, "Thermal Accommodation of a Gas on a Surface and Heat Transfer in CVD and PECVD Experiments", Journal of Physics D: Applied Physics, Vol. 30, p.499 (1997).

[161] T.M. Berlicki, "Heat Dissipation in Thin – Film Vacuum Sensor", Journal of Vacuum Science and Technology A, Vol. 19, No. 1, p.325 (2001).

[162] J.A. Bowman and D.T. Schwartz, "High Peclet Number Mass Transfer in the Acoustic Streaming Flow Between two Concentric Cylinders", International Journal of Heat and Mass Transfer, Vol. 41, Nos. 8/9, p.1065 (1998).

[163] Z. Guo and N.K. Anand, "An Analytical Model to Predict Condensation of R-410A in a Horizontal Rectangular Channel", Journal of Heat Transfer, Vol. 122, p.613 (2000).

[164] J.F. Horton and J.E. Peterson, "Rayleigh Light Scattering Measurements of Transient Gas Temperature in a Rapid Chemical Vapour Deposition Reactor". Journal of Heat Transfer, Vol. 122, p.165 (2000).

[165] Q.-S. Chen, H. Zhang, V. Prasad, C.M. Balkas, and N.K. Yushin, "Modeling of Heat Transfer and Kinetics of Physical Vapour Transport Growth of Silicon Carbide Crystals", Journal of Heat Transfer, Vol. 123, p.1098 (2001).

[166] G.K. White, "Measurement of Solid Conductors at Low Temperatures", in *Thermal Conductivity*, (edited by R.P. Tye), Vol. 1, Academic Press, London, p. 69 (1969).

Reproduced with permission of the copyright owner. Further reproduction prohibited without permission.

[167] B. Lawton and G. Klingenberg, *Transient Temperature in Engineering and Science*, Oxford Science Publications, Oxford, (1996).

[168] L. Stasiek and M.W. Collins, "Radiant and Convective Heat Transfer for Flow of a Radiation Gas in a Heated/Cooled Tube with a Grey Wall", International Journal of Heat and Mass Transfer, Vol. 36, No. 14, p.3633 (1993).

[169] A. Matthews, "A Predictive Model for Specimen Heating during Ion Plating", Vacuum, Vol. 32, No. 6, p. 311 (1982).

[170] D.W. Hoffman, "A Sputtering Wind", Journal of Vacuum Science and Technology, A, Vol. 3, No. 3, p.561 (1985).

[171] Q. Wei, J. Sankar, A.K. Sharma, Y. Yamagata and J. Narayan, "Effect of Chamber Pressure and Atmosphere on the Microstructure and nanomechanical Properties of Amorphous Carbon Films Prepared by Pulsed Laser Deposition", Journal of Vacuum Science and Technology, A, Vol. 19, No. 1, p. 311 (2001).

[172] G.M. Turner, I.S. Falconer, B.W. James, and D.R. Mckenzie, "Monte Carlo Calculations of the Properties of Sputtered Atoms at a Substrate in a Magnetron Discharge", Journal of Vacuum Science and Technology, A, Vol. 10, No. 3, p. 455 (1992).

[173] S.K. Dew, T. Smy, and M. Brett, "Step Coverage and Compositional Studies Using Integrated Vapour – Transport and Film Deposition Models", Japanese Journal of Applied Physics, Vol. 33, Part 1, p.1140 (1994).

[174] S.K. Dew, *Processes and Simulation for Advanced Integrated Circuit Metallization*, Ph.D. thesis, Department of Electrical Engineering, University of Alberta, Edmonton (1992).

[175] S.D. Ekpe and S.K. Dew, "Theoretical and Experimental Determination of the Energy Flux during Sputter Deposition onto an Unbiased Substrate", Journal of Vacuum Science and Technology, A, Vol. 21, No. 2, p. 476 (2003).

Reproduced with permission of the copyright owner. Further reproduction prohibited without permission.

[176] T.P. Drusedau, T. Brock, T.-M. John, and F. Klabunde, "Energy Transfer into Growing Film during Sputter Deposition: an Investigation by Calorimetric Measurement and Monte Carlo Simulations", Journal of Vacuum Science and Technology, A, Vol. 17, No. 5, p.2896 (1999).

[177] T.P. Drusedau, M. Lohmann, and B. Garke, "Decay Length of Pressure Dependent Deposition Rate for Magnetron Sputtering", Journal of Vacuum Science and Technology, A, Vol. 16, No. 4, p.2728 (1998).

[178] M.L. Escrivao, A.M. Moutinho, and M.J. Maneira, "Planar Magnetron Glow Discharge on Copper: Empirical and Semiempirical Relations", Journal of Vacuum Science and Technology, A, Vol. 12, No. 3, p.723 (1994).

[179] I.K. Moon, D.H. Jung, K.-B. Lee, and Y.H. Jeong, "Peltier Microcalorimeter", Applied Physics Letters, Vol. 76, No. 17, p.2451 (2000).

[180] N. Abedinov, P. Grabiec, T. Gotszaik, Tz. Ivanov, J. Voigt, and I.W. Rangelow, "Micromachined Piezoresistive Cantilever Array with Integrated Resistive Microheater for calorimetry and Mass Detection", Journal of Vacuum Science and Technology, A, Vol. 19, No. 6, p.2884 (2001).

[181] G. Cocorullo, F.G. Della Corte and I. Rendina, "Temperature Dependence of the Thermo-optic Coefficient in Crystalline Silicon between Room Temperature and 550 K at the Wavelength of 1523 nm", Applied Physics Letters, Vol. 74, No. 22, p. 3338 (1999).

[182] V. Lysenko, S. Perichon, B. Remaki, D. Barbier and B. Champagnon, "Thermal Conductivity of Thick Meso-porus Silicon Layers by Micro-Raman Scattering", Journal of Applied Physics, Vol. 86, No. 12, p. 6841 (1999).

[183] D. McCammon, R. Almy, E. Apodaca, S. Deoker, M. Galeazzi, S.-I. Han, A. Lesser, W. Sanders, R.L. Kelley, S.H. Moseley, F.S. Porter, C.K. Stahle and A.E. Szymkowiak, "High-resolution Calorimetry: Limitations of Doped

Reproduced with permission of the copyright owner. Further reproduction prohibited without permission.

Semiconductor Thermometers", Nuclear Instruments and Methods in Physics Research A, Vol. 436, p.205 (1999).

[184] A. Grenville, R. Uttaro, J.H.C. Sedlacek, M. Rothschild and D. Corliss, "Calorimetric Measurements of Optical Materials for 193 nm Lithography", Journal of Vacuum Science and Technology B, Vol. 14, No. 6, p. 4184 (1996).

[185] D. Kazantsev, G. Guttroff, M. Bayer and A. Forchel, "Sample Temperature Measurement in a Scanning Near-field Optical Microscope", Applied Physics Letters, Vol. 72, No. 6, p. 689 (1998).

[186] Z. Dohnalek, S. Mezhenny, I. Lyubinetsky, W.J. Choyke, and J.T. Yates, Jr., "Control of Silicon Crystal Temperature by Measurement of Resistivity", Journal of Vacuum Science and Technology A, Vol. 15, No. 5, p.2766 (1997).

[187] N.K. Zayer, P.J. Henderson, A.J.C. Grellier and C.N. Pannell, "In Situ Substrate Temperature Measurements during Radio Frequency Sputtering of ZnO thin film Using Fiber Bragg Grating", Journal of Vacuum Science and Technology A, Vol. 17, No. 3, p.871 (1999).

[188] B. Ullrich, H. Ezumi, S. Keitoku and T. Kobayashi, "Temperature Dependence of Reflectance and Transmittance at 514.5 nm of CdS Film formed by Laser Ablation", Applied Physics Letters, Vol. 68, No. 21, p. 2985 (1996).

[189] W. Ryba-Romanowski, S. Golab, W.A. Pisarski, G. Dominiak-Dzik, M.N. Palatnikov, N.V. Sidorov and V.T. Kalinnikov, "Influence of Temperature on the Optical Properties of $LiTaO_3$:Cr", Applied Physics Letters, Vol. 70, No. 19, p. 2505 (1997).

[190] J. Kikuchi, S. Fujimura, R. Kurosaki and H. Yano, "Pulse-modulated Infrared-laser Interferometric Thermometry for Non-contact Silicon Substrate Temperature Measurement", Journal Vacuum Science Technology A, Vol. 15, No. 4, p. 2035 (1997).

Reproduced with permission of the copyright owner. Further reproduction prohibited without permission.

[191] D.H. Zhang and D.E. Drodie, "Crystallite Orientation and the Related Photoresponse of Hexagonal ZnO Films Deposited by RF Sputtering", Thin Solid Films, **251**, 151 (1994).

[192] R.R. Chromik W.K. Neils, and E.J. Cotts, "Thermodynamic and Kinetic Study of Solid State Reactions in the Cu-Si System", Journal of Applied Physics, Vol. 86, No. 8, p. 4273 (1999).

[193] T.T. Lay, Y. Yoshitake and B. Mebarki, "Temperature Effect on Growth of well-ordered Thin Al_2O_3 Film on NiAl(110)", Journal of Vacuum Science and Technology, A, Vol. 20, No. 6, p. 2027 (2002).

[194] H. Nishino, W, Yang, Z. Dohnalek, V.A. Ukraintsev, W.J. Choyke and J.T. Yates, Jr., "Silicon Crystal Heating and Thermocouple Mounting Designs", Journal of Vacuum Science and Technology A, Vol. 15, No. 1, p.182 (1997).

[195] O. Eyal, V. Scharf, and A. Katzir, "Temperature Measurement Using Pulsed Photothermal Radiometry and Silver Hallide Infrared Optical Fibres", Applied Physics Letters, Vol. 70, No. 12, p.1509 (1997).

[196] A. Matthews and D.T. Gethin, "Heating Effects in Ionization-assisted Processes", Thin Solid Films, Vol. 117, p. 261 (1984).

[197] K.D. Irwin, G.C. Hilton, D.A. Wollman, and J.M. Martinis, "Thermal – Response Time of Superconducting Transition – Edge Microcalorimeters", Journal of Applied Physics, Vol. 83, No. 8, p.3978 (1998).

[198] A.N. Pargellis, "Evaporating and Sputtering: Substrate Heating Dependence on Deposition Rate", Journal Vacuum Science and Technology A, Vol. 7, No. 1, p.27 (1989).

[199] R.P. Howson, H. A. J'afer and A. G. Spencer, "Substrate Effects from an Unbalanced Magnetron", Thin Solid Films, Vol. 193/194, p.127 (1990).

Reproduced with permission of the copyright owner. Further reproduction prohibited without permission.

[200] S.S. Lau, R.H. Mills and D.G.Muth, "Temperature Rise during Film Deposition by RF and DC Sputtering", Journal of Vacuum Science and Technology, Vol. 9, No. 4, p. 1196 (1972).

[201] A. Hammiche, L. Bozec, M. Conroy, H.M. Pollock, G. Mills. J.M.R. Weaver, D.M. Price, M. Reading, D. J. Hourston and M. Song, "Highly localized thermal Mechanical, and Spectroscopic Characterization of Polymers Using Miniaturized Thermal probes" Journal of Vacuum Science and Technology, B Vol. 18, No. 3, p. 1322 (2000).

[202] Thomas D. McGee, *Principles and Methods of Temperature Measurements*, John Wiley, New York (1988).

[203] B. Window and N, Savvides, "Unbalanced dc Magnetrons as Sources of High Ion Fluxes", Journal of Vacuum Science and Technology, A, Vol. 4, No. 3, p. 453 (1986)

[204] S.A. Nikitov, Y.V. Gulyaev and A.D. Boardman, "Reflection and Scattering of Spin Waves by Surface Roughness of a Ferromagnet", Waves in Random Media, Vol. 6, p. 61 (1996).

[205] D. R. Lide (Editor-in-Chief), *Handbook of Chemistry and Physics*, CRC Press, Boca Raton (1991).

[206] J. H. Keller and R. G. Simmons, "Sputtering Process Model of Deposition Rate", IBM Journal of Research and Development, Vol. 23, p. 24 (1979).

[207] Y. Yamamura, "Contribution of Anisotropic Velocity Distribution of Recoil Atoms to Sputtering Yields and Angular Distributions of Sputtered Atoms", Radiation Effects, Vol. 55, No. 9, p. 49 (1981).

[208] H.H. Andersen, B. Stenum, T. Sorensen, and H.J. Whitlow, "Angular Distribution of Particles Sputtered from Cu, Pt and Ge Targets by KeV Ar^{+} Ion Bombardment", Nuclear Instruments and Methods, Vol. B6, p.459 (1985).

Reproduced with permission of the copyright owner. Further reproduction prohibited without permission.

[209] Y. Yamamura, T. Takiguchi and M. Ishida, "Energy and Angular Distributions of Sputtered Atoms at Normal Incidence", Radiation Effects and Defects in Solids, Vol. 118, p. 237 (1991).

[210] G. Ecker and K.G. Emeleus, "Cathode Sputtering in Glow Discharges", Proceedings of Physical Society, B. 67, p. 546 (1954).

[211] K.-B. Persson, "Inertia-Controlled Ambipolar Diffusion", Physics of Fluids, Vol. 5, p. 1625 (1962).

[212] I. Petrov, I. Ivanor, V. Orlinov and J.-E. Sundgren, "Comparison of Magnetron Sputter Deposition Conditions in Neon, Argon, Krypton and Xenon Discharges" Journal of Vacuum Science and Technology, A, Vol. 11, No. 5, p. 2733 (1993).

[213] S.D. Ekpe, L.W. Bezuidenhout, S.K. Dew, "Deposition Rate Model of Magnetron Sputtered Particles", Thin Solids Films (Accepted for publication), (2004).

[214] H. Kersten, H. Deutsch, H. Steffen, G.M.W. Kroesen and R. Hippler, "The Energy Balance at Substrate Surfaces During Plasma Processing", Vacuum, Vol. 63, p. 385 (2001).

[215] D.J. Field, S.K. Dew and R.E. Burrell, "Spatial Survey of a Magnetron Plasma Sputtering System using a Langmuir Probe", Journal of Vacuum Science and Technology, A, Vol. 20, No. 6, p. 2032 (2002).

[216] T.J. Love, *Radiative Heat Transfer*, Merrill, New York (1968).

[217] J.R. Simonsen, *An Introduction to Engineering Heat Transfer*, McGraw-Hill, New York (1967).

[218] S. Patankar, *Numerical Heat Transfer and Fluid Flow*, Taylor and Francis, London (1980).

[219] Y. Kim, J. Bae, H. Kim and S. Kang, "Modelling of Passive Heating for Replication of Sub-micron Patterns in Optical Disk Substrates", Journal of Physics D: Applied Physics, Vol. 37, p. 1319 (2004).

Reproduced with permission of the copyright owner. Further reproduction prohibited without permission.

[220] P.B. Johns and R.L. Beurle, "Numerical solution of Two-Dimensional Scattering Problems Using a Transmission-Line Matrix ", *Proceedings of IEEE*, Vol. 118, No. 8, p. 1203 (1971).

[221] P.B. Johns, "Application of the Transmission-line Matrix Method to Homogenous Waveguides of Arbitrary Cross-section", *Proceedings of IEEE*, Vol. 119, No. 8, p. 1086 (1972).

[222] P.B. Johns, "New Symmetrical Condensed Node for Three-dimensional solution of Electromagnetic Wave Problems by TLM", Electronics Letters, Vol. 22, p. 162 (1986).

[223] D.H. Choi and W.J.R. Hoefer, "The Simulation of Three Dimensional Wave Propagation by Scalar TLM Model", in *IEEE-MIT International Microwave Symposium*, San Francisco, CA, p 70, (1984).

[224] A.H.M. Saleh and P. Blanchfield, "Analysis of Acoustic Radiation Patterns of Array Transducers using the TLM Method", International Journal of Numerical Modeling, Vol. 3, p.39 (1990).

[225] C. Christopoulos, *The Transmission-Line Modeling Method*, IEEE Press, 1995.

[226] E. Martensson and U. Gafvert, "A Three-dimensional Network Model Describing a Non-linear Composite Material", Journal of Physics D: Applied Physics, Vol. 37, p.112 (2004).

[227] S.M. Rossnagel and H.R. Kaufman, "Langmuir Probe Characterization of Magnetron Operation", Journal of Vacuum Science and Technology, A, Vol. 4, No. 3, p. 1822 (1986).

[228] P. Spatenka, J. Vlcek and J. Blazek, "Langmuir Probe Measurements of Plasma Parameters in a Planar Magnetron with Additional Plasma Confinement", Vacuum, Vol. 55, p. 165 (1999).

Reproduced with permission of the copyright owner. Further reproduction prohibited without permission.